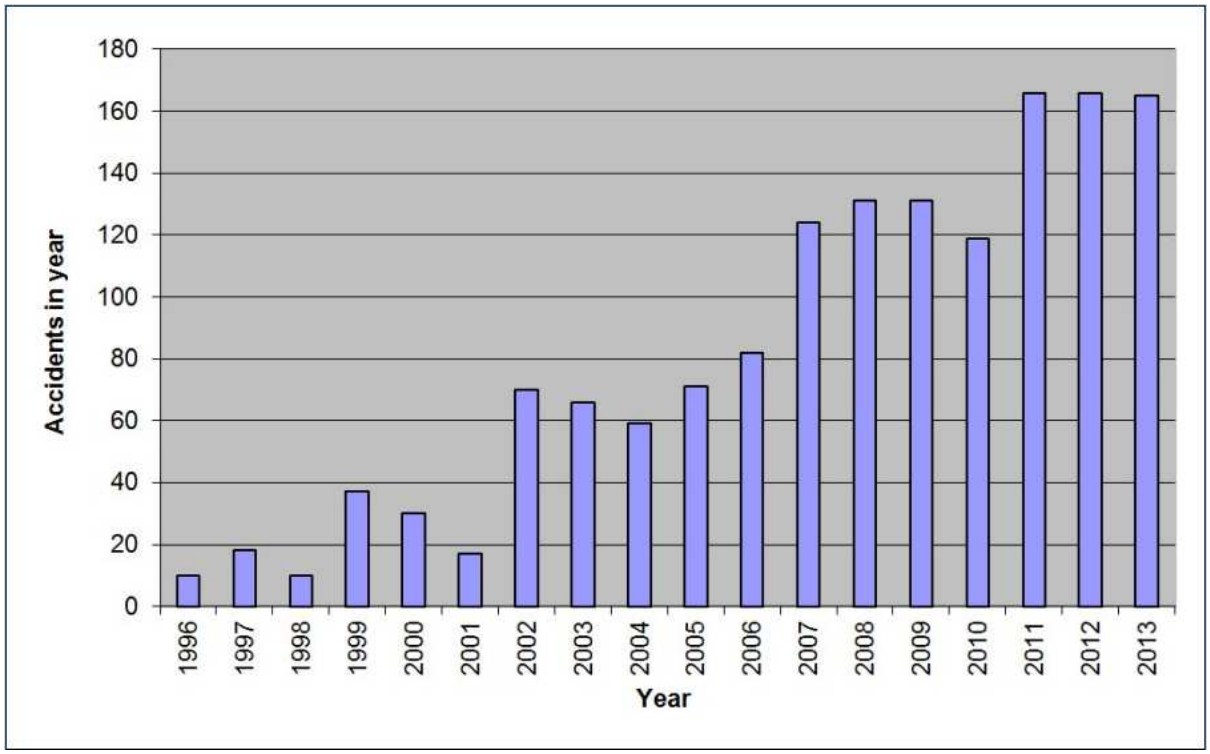

Figure 1 Statistics of wind turbine accidents reported by the end of2013 which shows an overall increasing trend.

Copyright © DashWin Consortium 2012

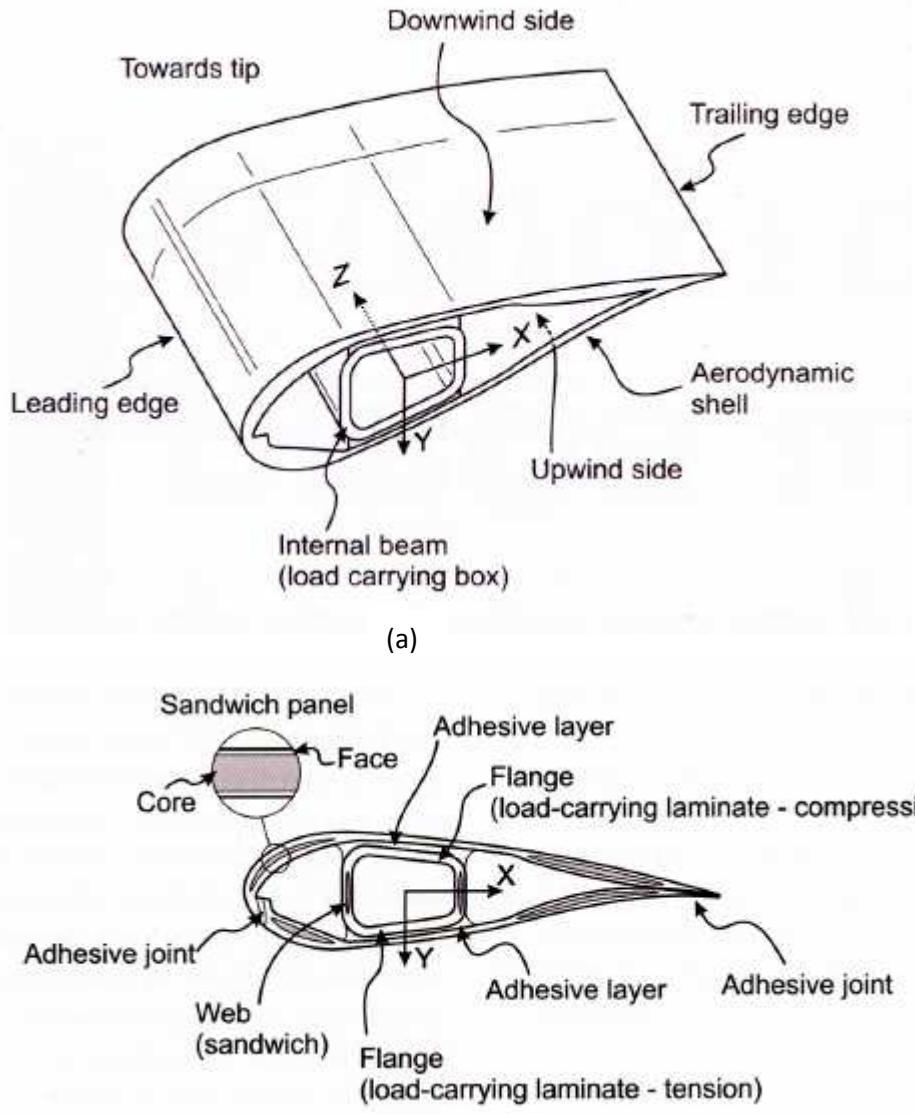

Figure 2 Configuration of wind turbine blade. (a) Cross-sections through a composite wind turbine blade that incorporates a box-shaped beam spar. (b) The aerodynamic shell is usually constructed of polymeric composites and is reinforced against buckling by using sandwich structures with balsa or PVC foam cores. The spar is manufactured using a glass or carbon polymeric composite and may contain regions with sandwich structures (PVC or balsa). Also shown are locations for adhesive joints which are utilised in the majority of large wind turbine blades. From Sorensen et al [1].

[1] Sørensen, B. F., Jørgensen, E., Debel, C. P., Jensen, F. M., Jensen, H. M., Jacobsen, T.K., and Halling, K. "Improved design of large wind turbine blade of fibre composites based on studies of scale effects (Phase 1). Summary report". Riso-R-1390(EN), Risø National Laboratory, Denmark. 2004

Copyright © DashWin Consortium 2012

Figure 3 A magnetic climbing robot platform (Courtesy of BSR)

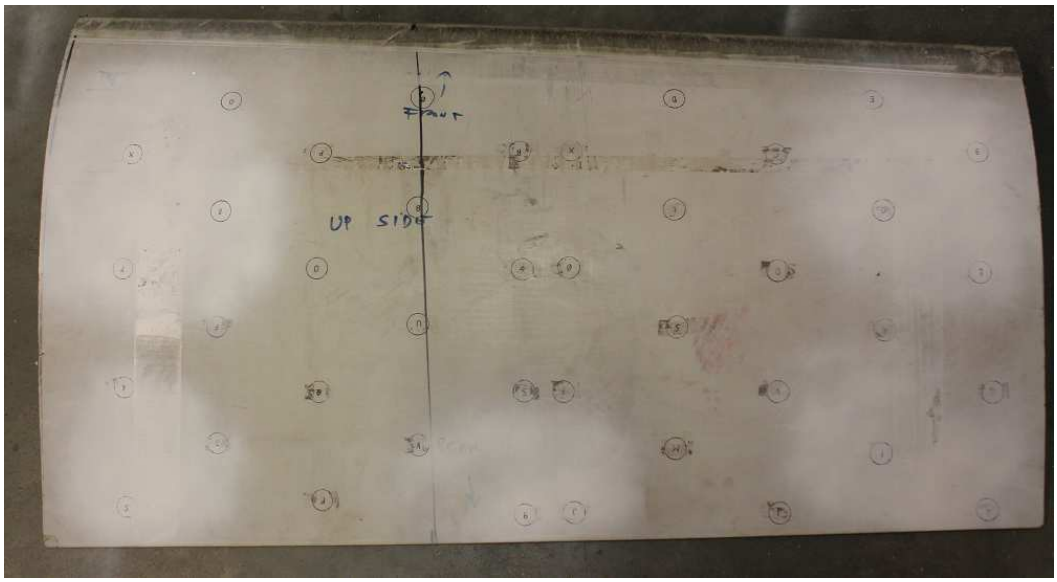

(a)

Copyright © DashWin Consortium 2012

(b)

Figure 4 Wind turbine blade (WTB) test sample-1. (a) Front view. Dimension: 1m x 0.5m. (b) Back surface where various artificial subsurface defects were fabricated for testing.

(a)

Copyright © DashWin Consortium 2012

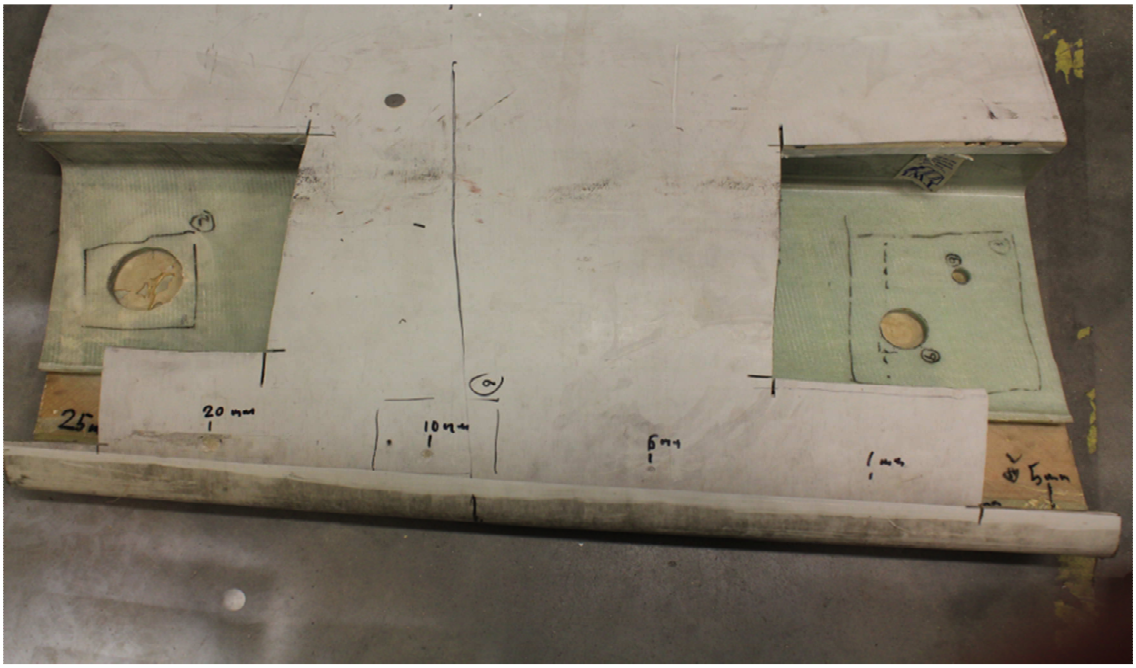

(b)

Figure 5 Wind turbine blade (WTB) test sample-2. (a) Front view. Dimension: 1m x0. 87m. (b) Back surface where various artificial subsurface defects were fabricated for testing.

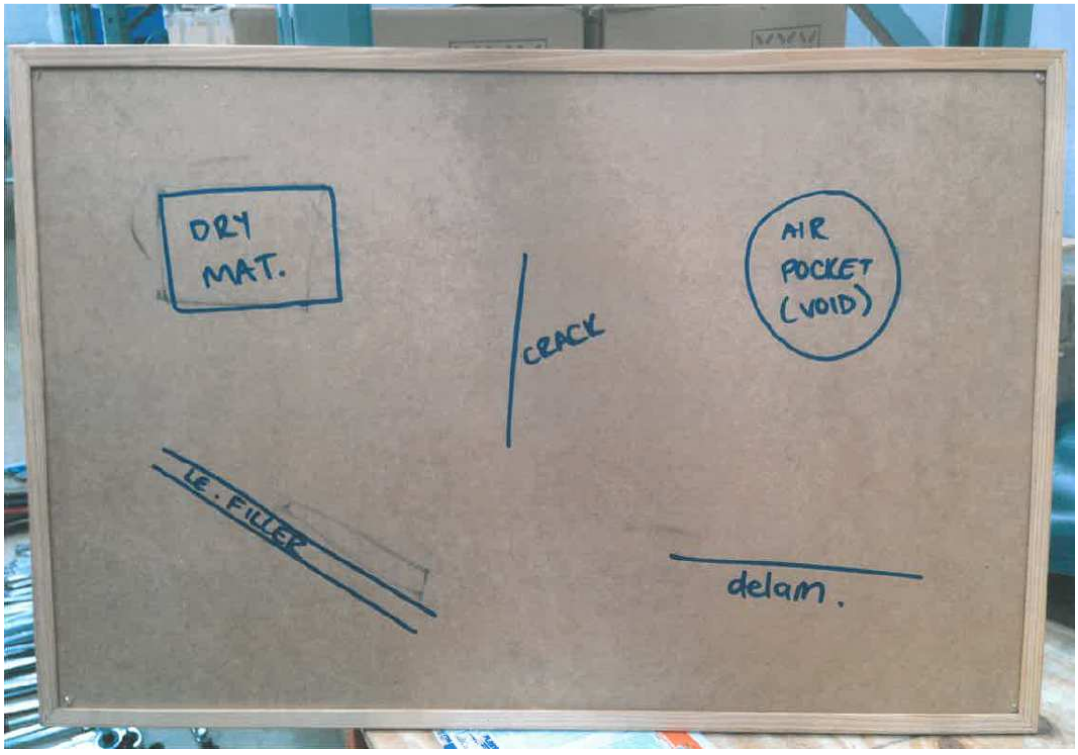

(a)

Copyright © DashWin Consortium 2012

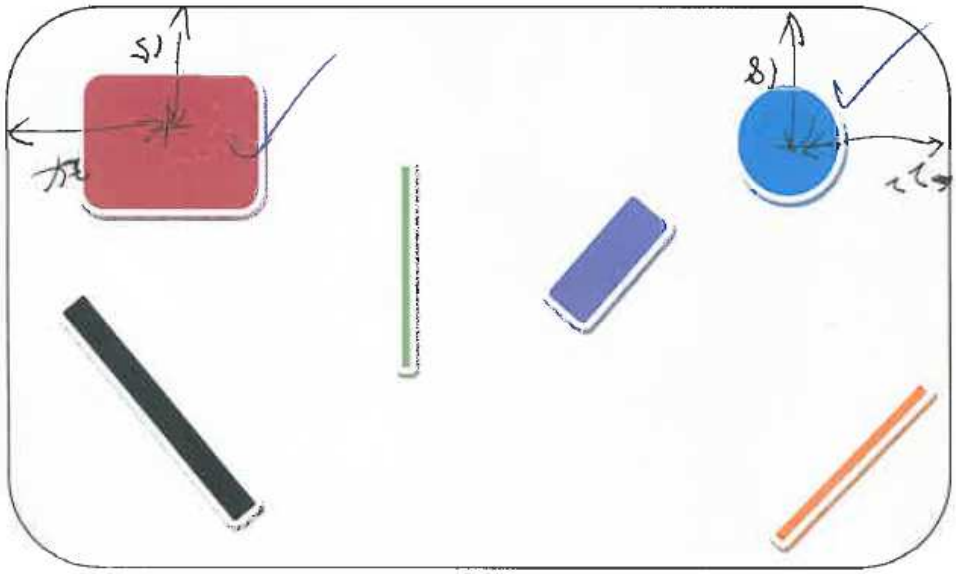

1. Dry laminate.
2. Epoxy Filler in Laminates.
3. Crack in Core Material.
4. Foreign Object in Laminates (Masking Tape)
5. Foreign Object Causing Laminate Void. (Wood Splinter)
6. De-lamination.

(b)

(c)

Figure 6 A test board. (a) Locations of the defects to be embedded. (b) Details of the defects. (c) One surface of the test board after the defects were embedded.

Copyright © DashWin Consortium 2012

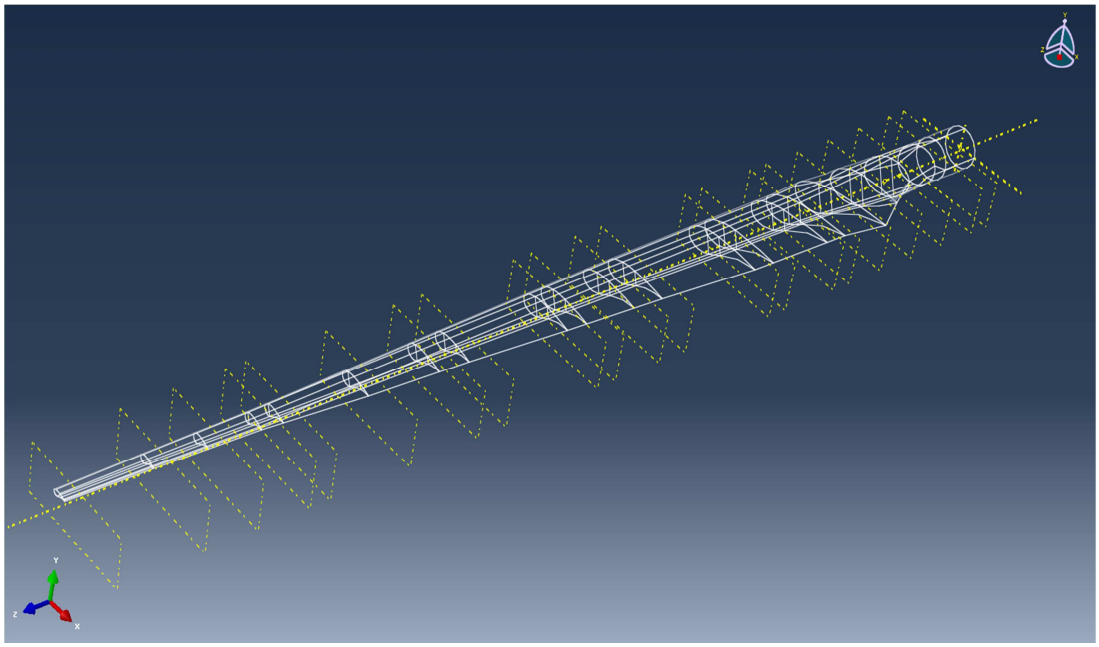

Figure 7 A 10m WTB illustrating sketches, datum planes and axes.

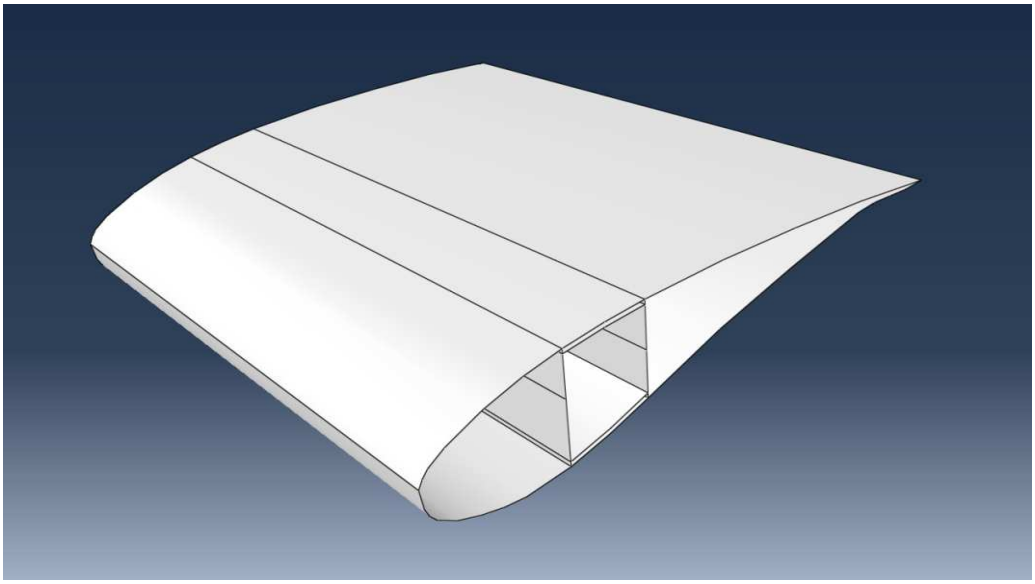

Figure 8 A 1m WTB section showing a lofted wire frame.

Copyright © DashWin Consortium 2012

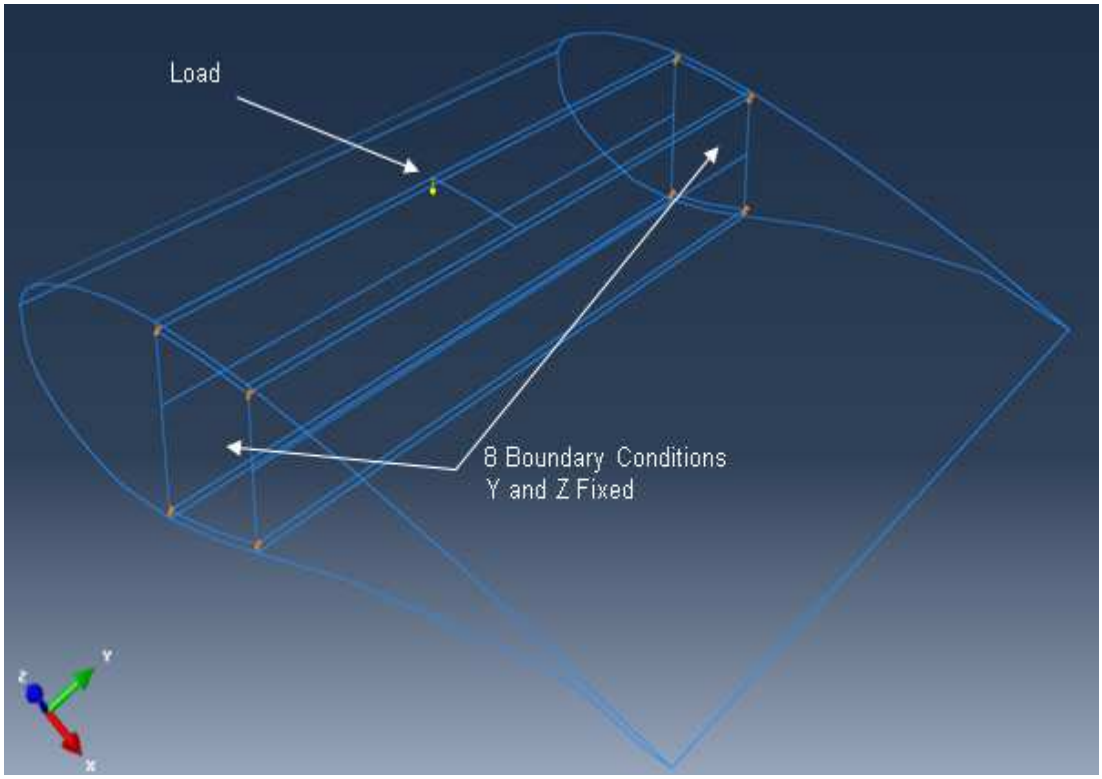

Figure 9 A 1m WTB section with loading and boundary conditions.

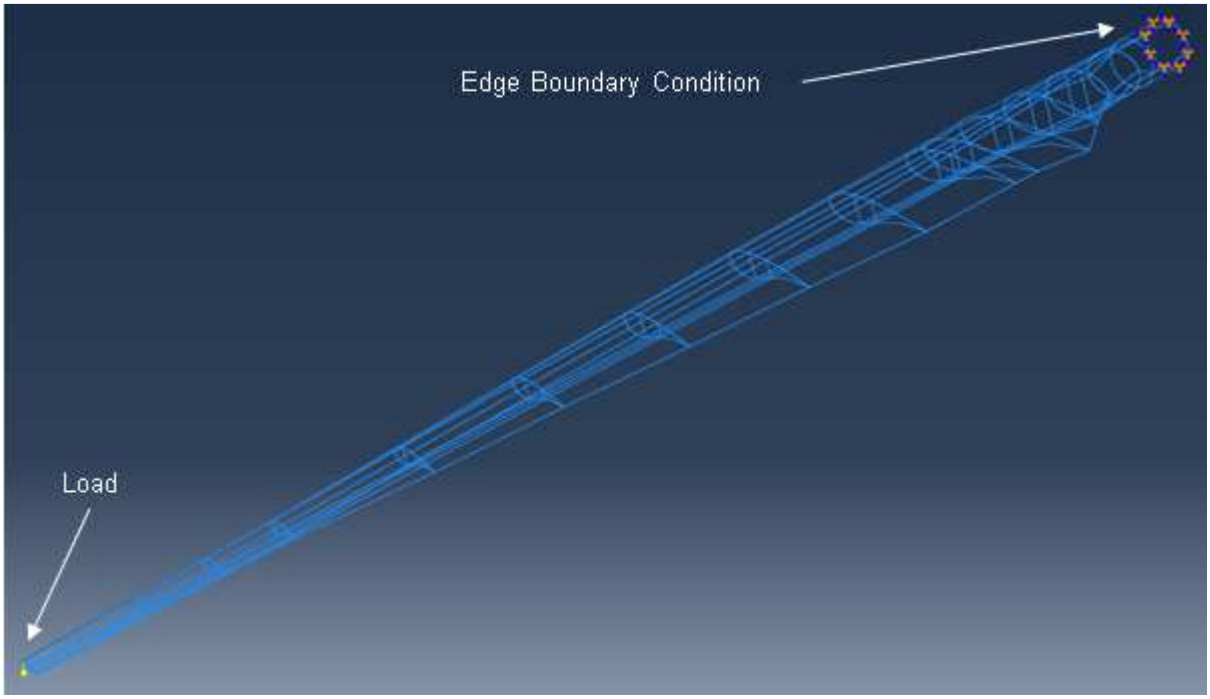

Figure 10 A 10m WTB verification model with loading and boundary conditions.

Copyright © DashWin Consortium 2012

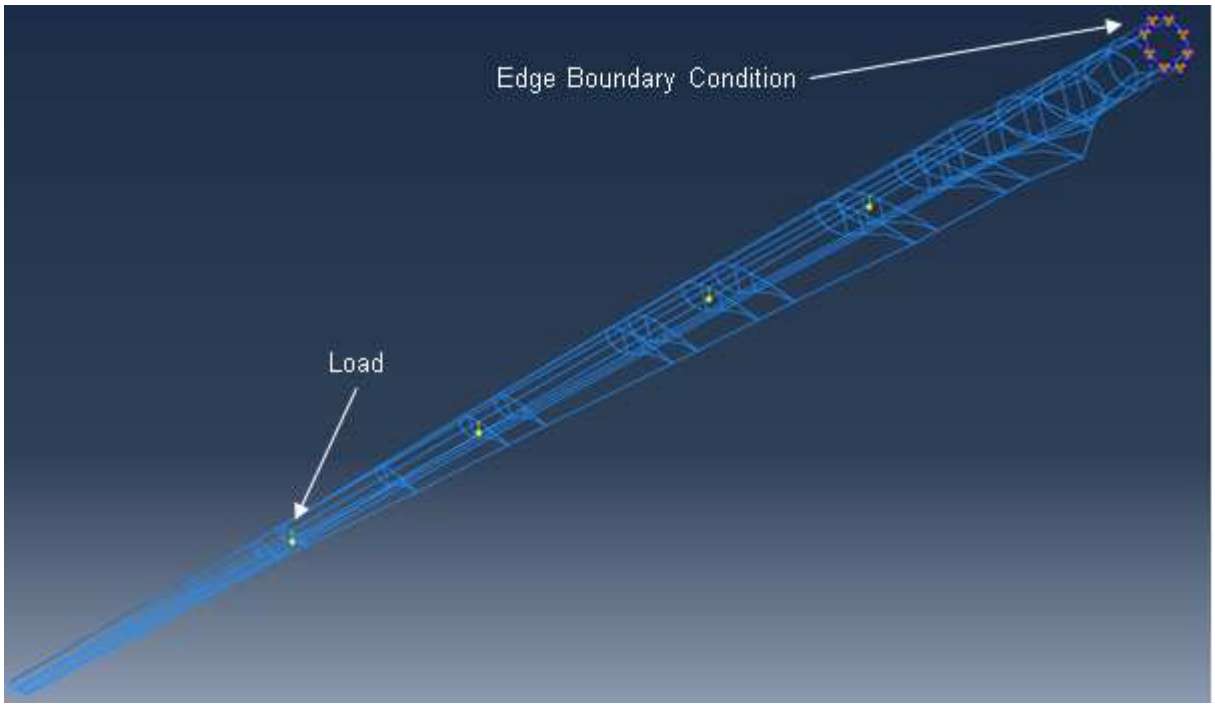

Figure 11 A 10m WTB with a quarter kip loading and boundary conditions.

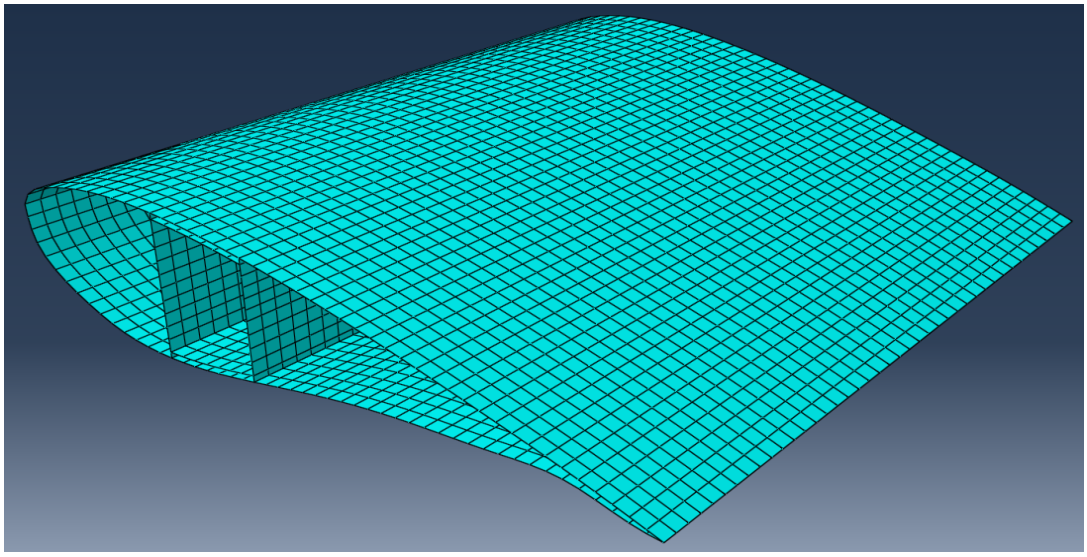

Figure 12 Mesh of a 1m section.

Copyright © DashWin Consortium 2012

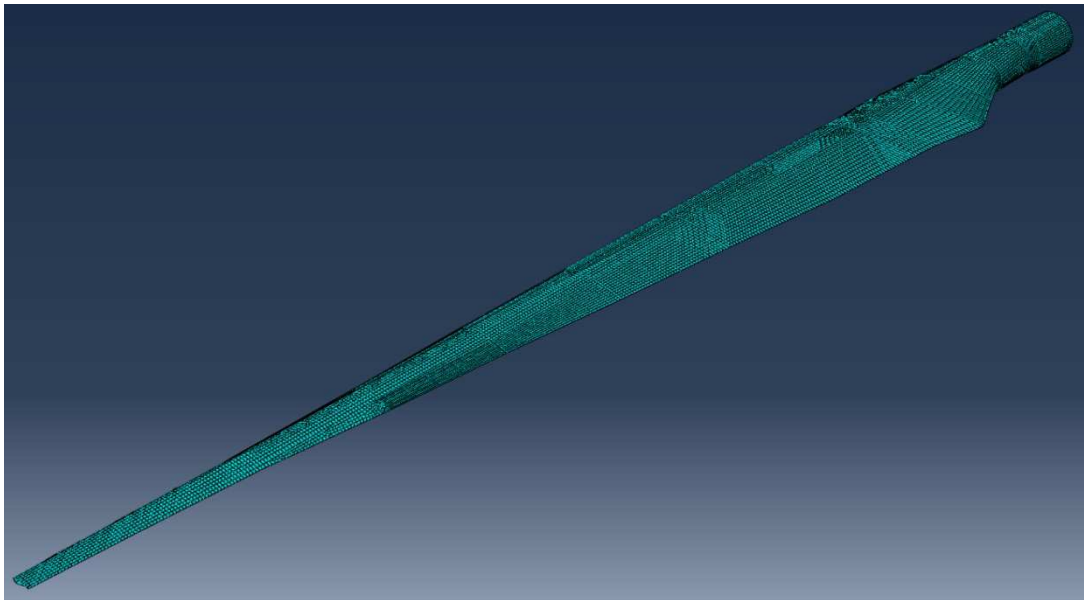

Figure 13 A 10m WTB verification model with low detail mesh.

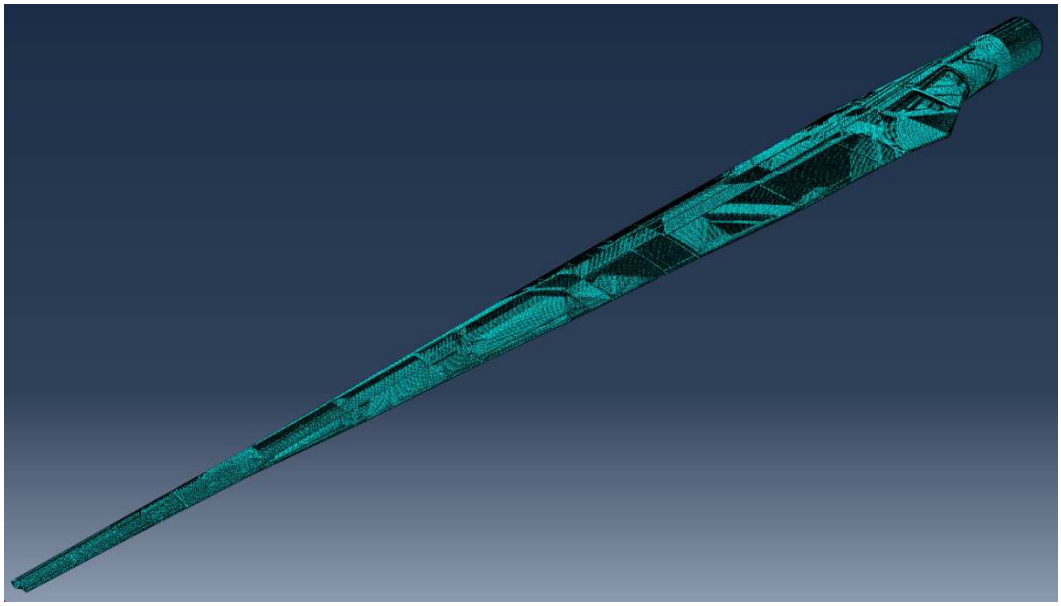

Figure 14 A 10m WTB with a high detail mesh.

Copyright © DashWin Consortium 2012

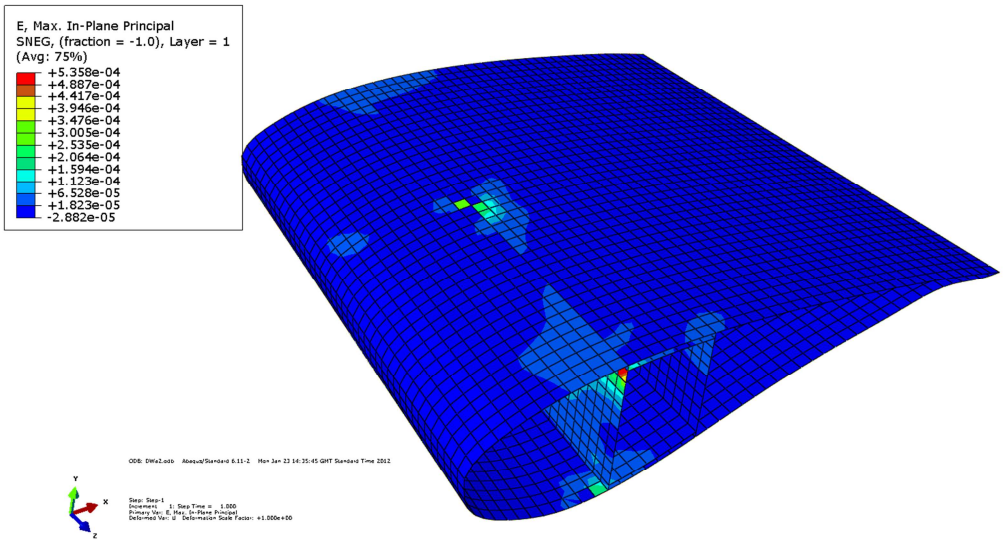

Figure 15 1m WTB section, top, max principal strain.

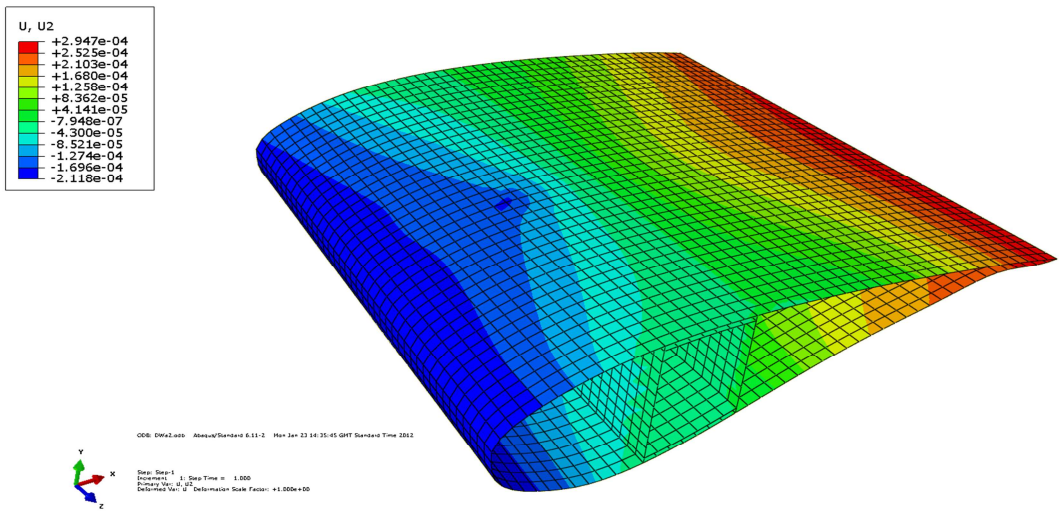

Figure 16 1m WTB section, top, U2 (transverse) displacement (Unit: m).

Copyright © DashWin Consortium 2012

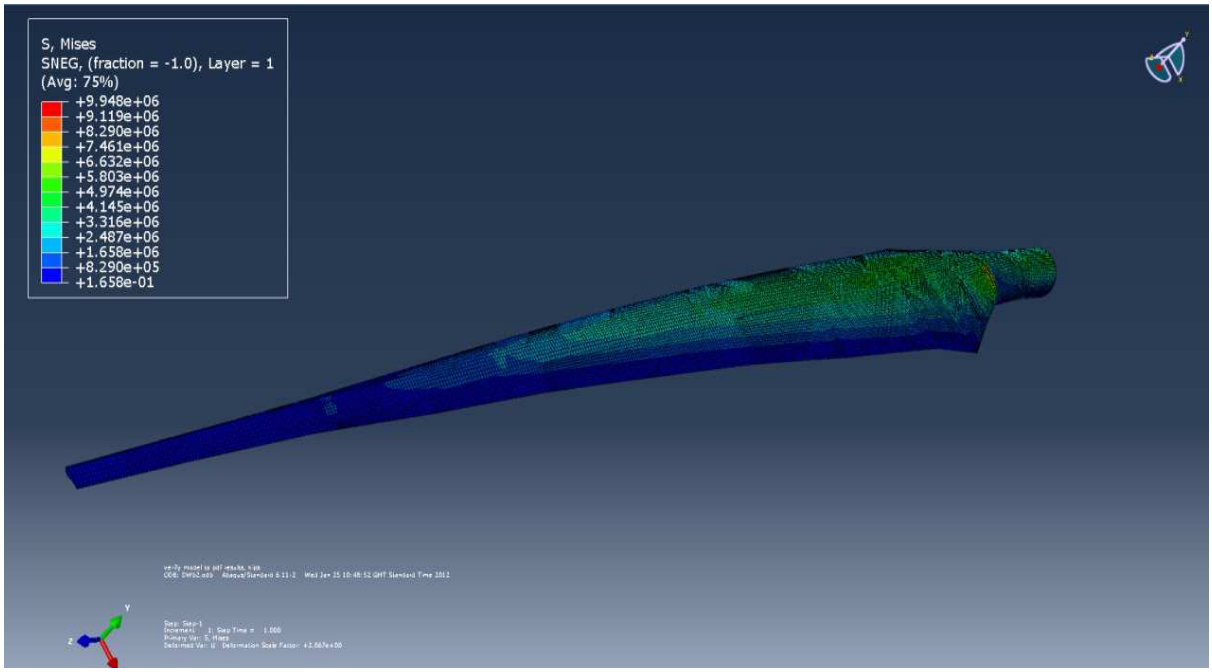

Figure 17 Stress distribution over the 10m WTB (Unit: Pa).

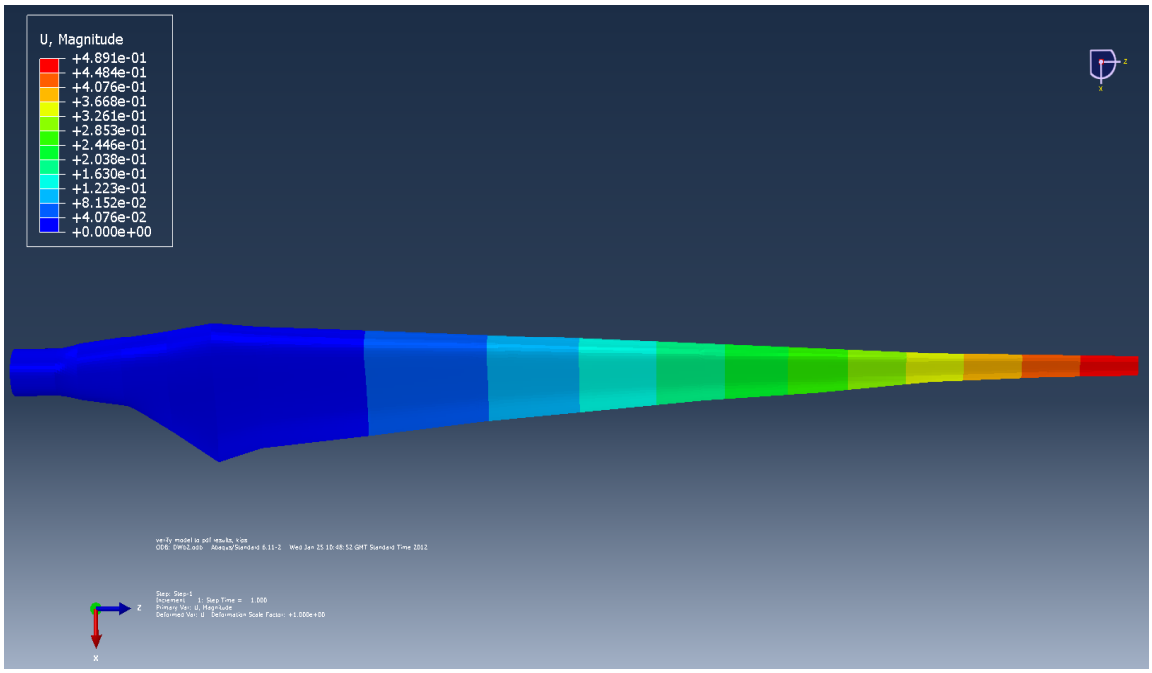

Figure 18 Displacement distribution of 10m WTB (Unit: m).

Copyright © DashWin Consortium 2012

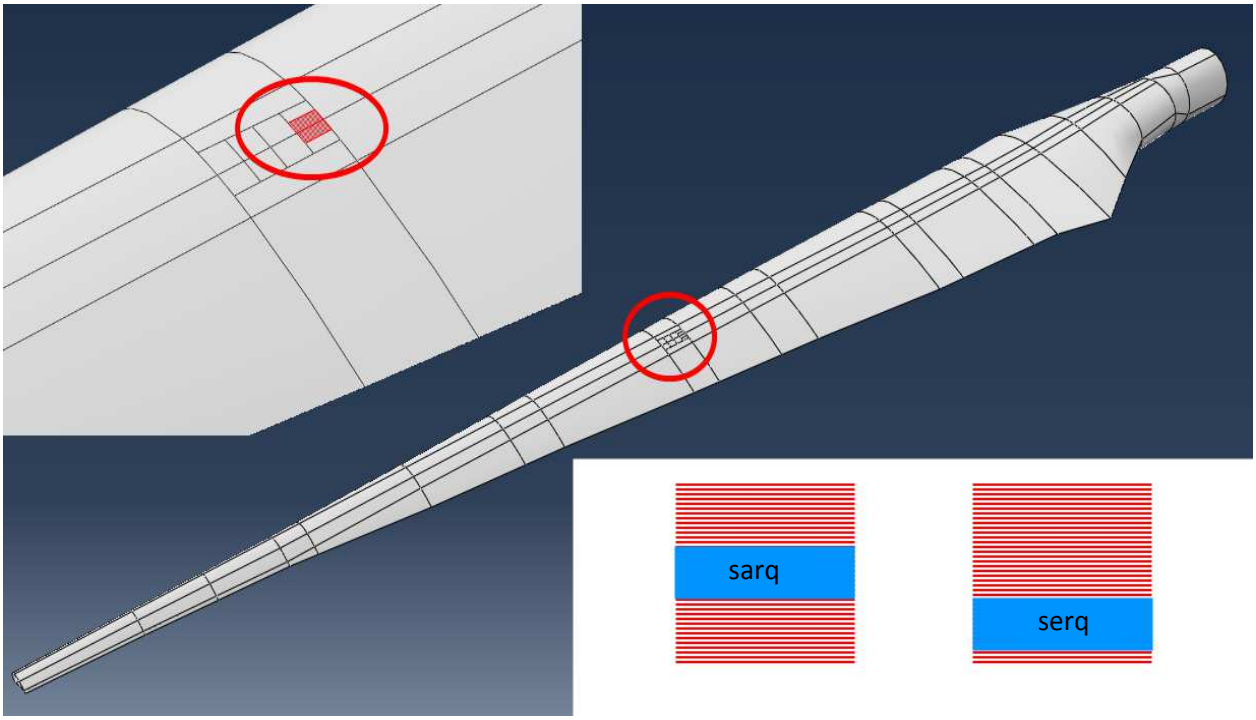

Figure 19 Defect location highlighted (centre), defect size highlighted (top left), and defect position in composite lay-up on the top half of WTB (bottom right).

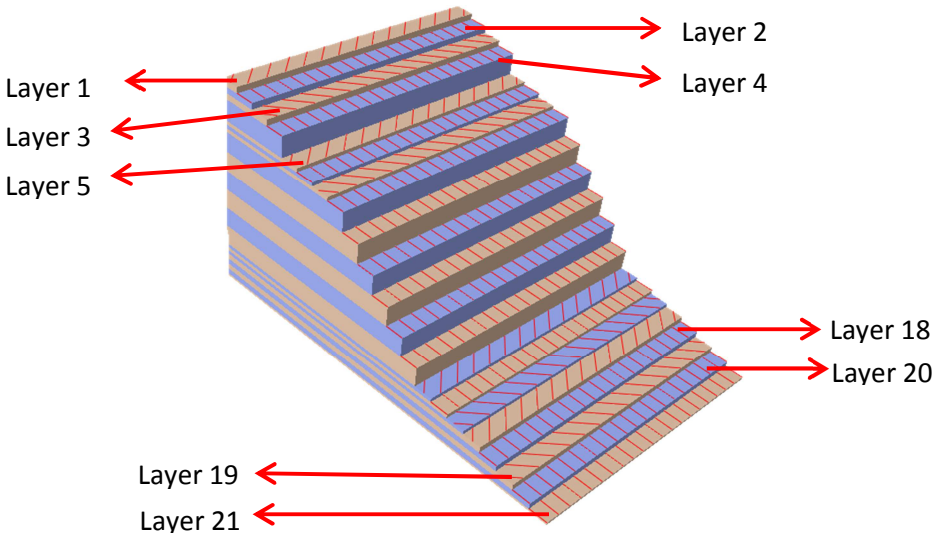

Figure 201 Plot of a typical composite lay-up of Section C in Table 4 used in the WTB.

Copyright © DashWin Consortium 2012

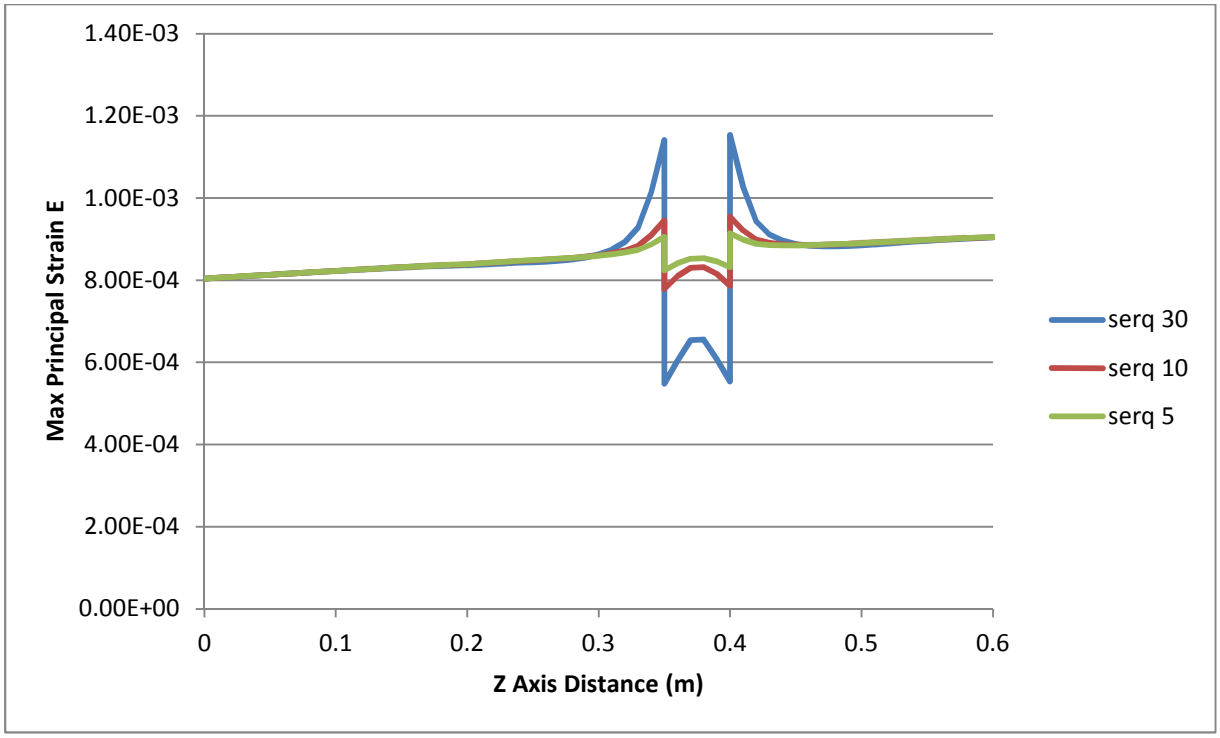

Figure 21 Comparison of maximum principal strain E along a surface path of bottom defects with 30%, 10% and 5% loss of thickness.

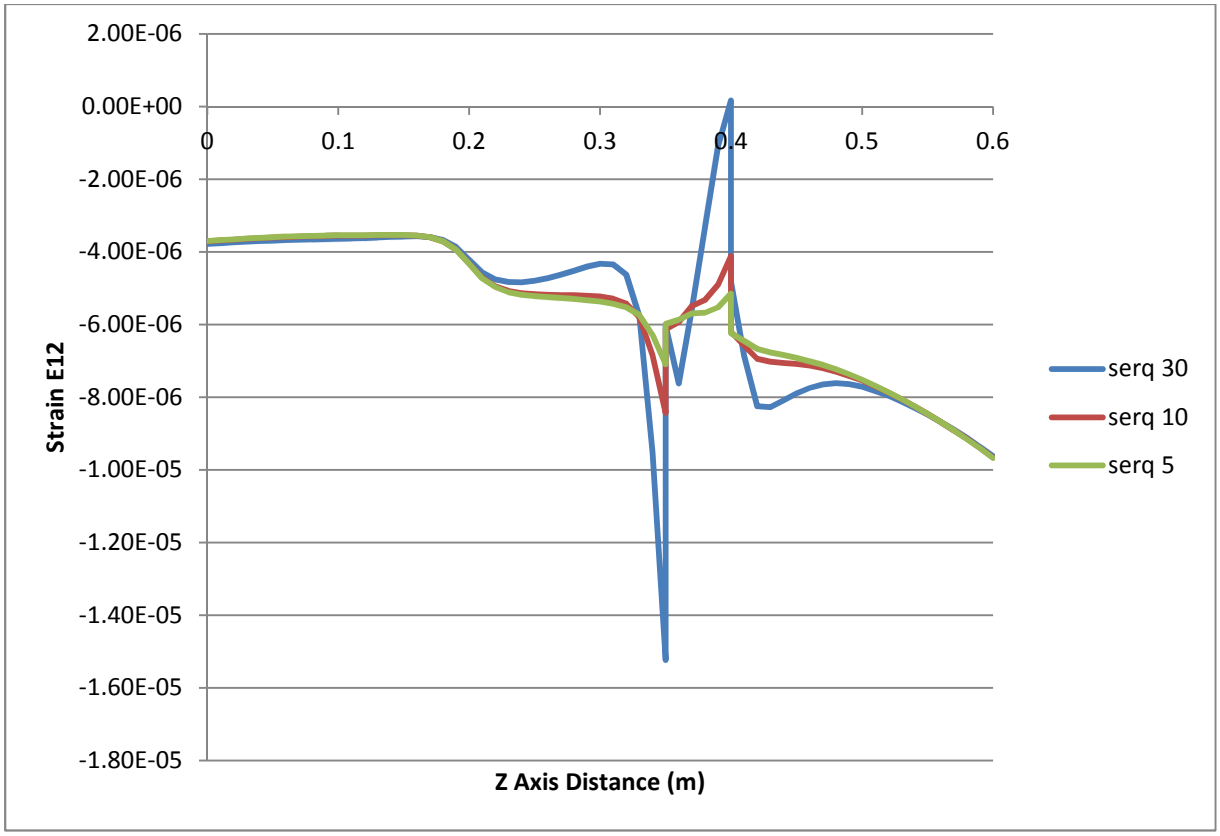

Figure 222 Comparison of shear strain E12 along a surface path of bottom defects with 30%, 10% and 5% loss of thickness.

Copyright © DashWin Consortium 2012

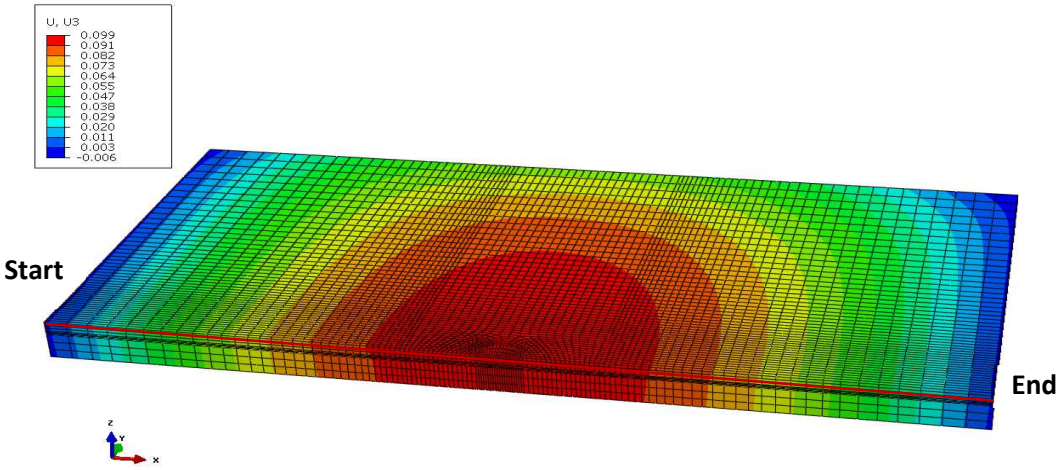

Figure 23 Displacement field output U_3 of FEM-2 at 5s. Red line indicates the path selected for data output.

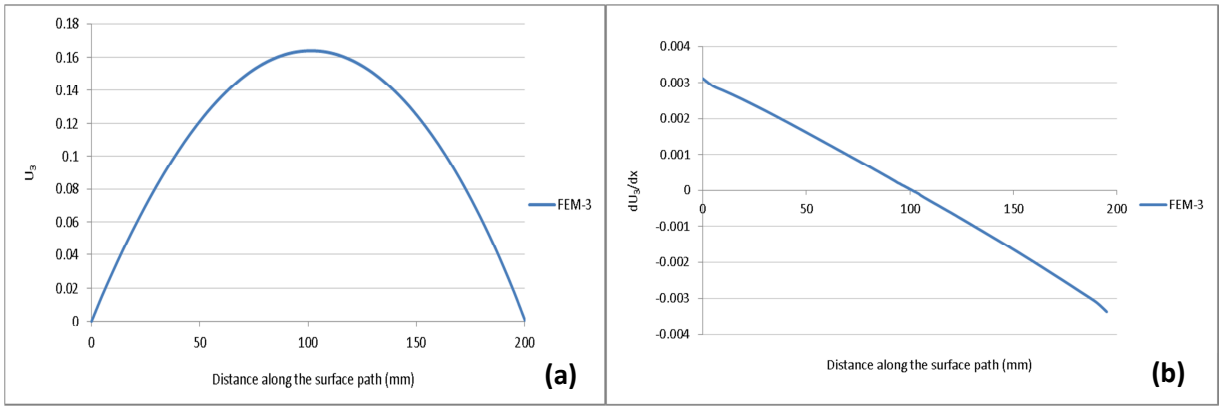

Figure 24 Data plot along the red coloured path showed in 23**Error! Reference source not found.**.
(a) Out-of-plane displacement U_3.
(b) Longitudinal gradient of out-of-plane displacement dU_3/dx.

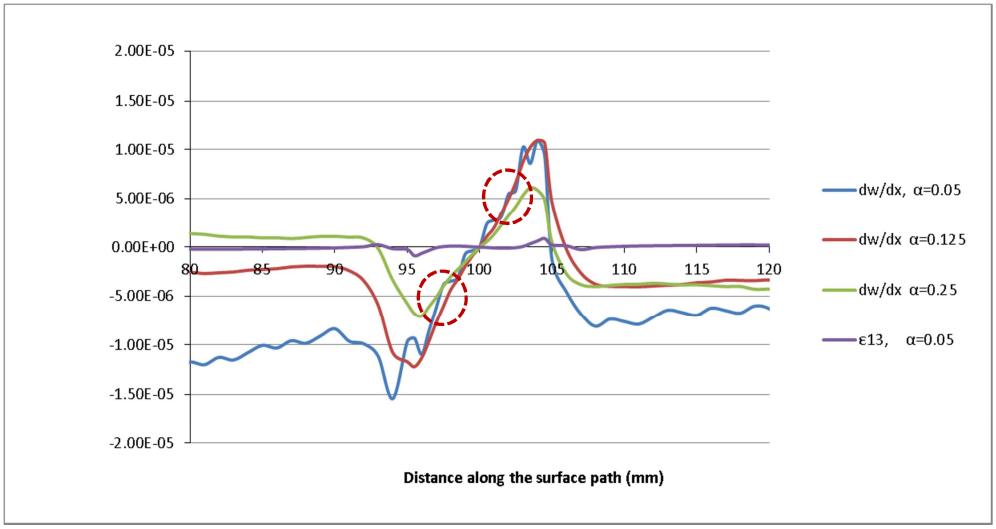

Figure 25 Filtered strain components $\frac{\partial w}{\partial x}$ plot along the selected surface path for FEM-3, FEM-10, and FEM-16. (β =0.05).

Copyright © DashWin Consortium 2012

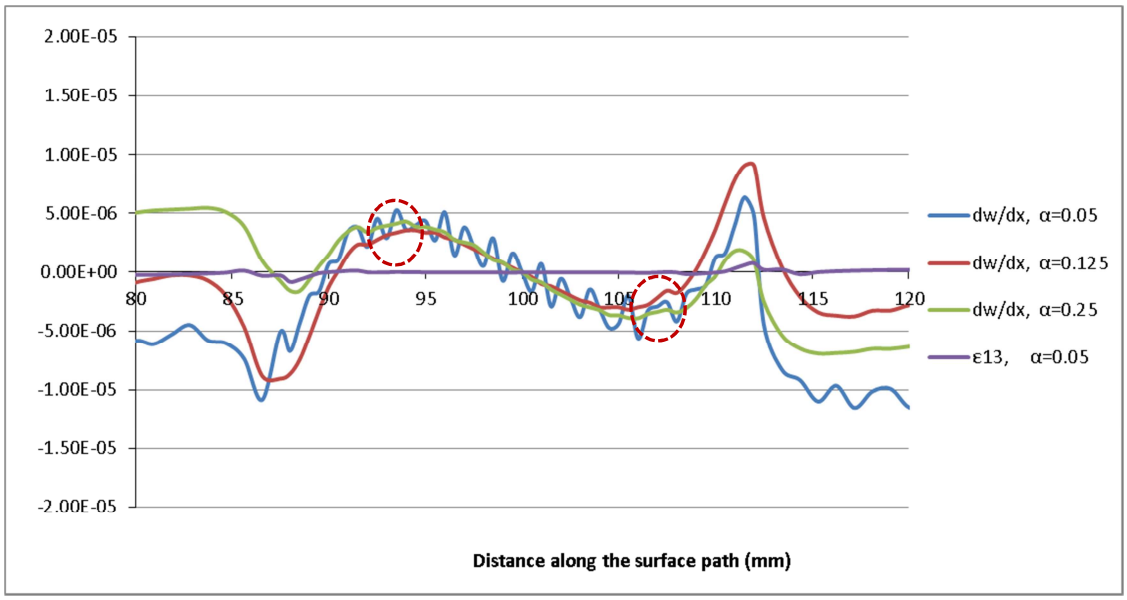

Figure 26 Filtered strain components $\frac{\partial w}{\partial x}$ plot along the selected surface path for FEM-6, FEM-12, and FEM-18. (β =0.125).

Copyright © DashWin Consortium 2012

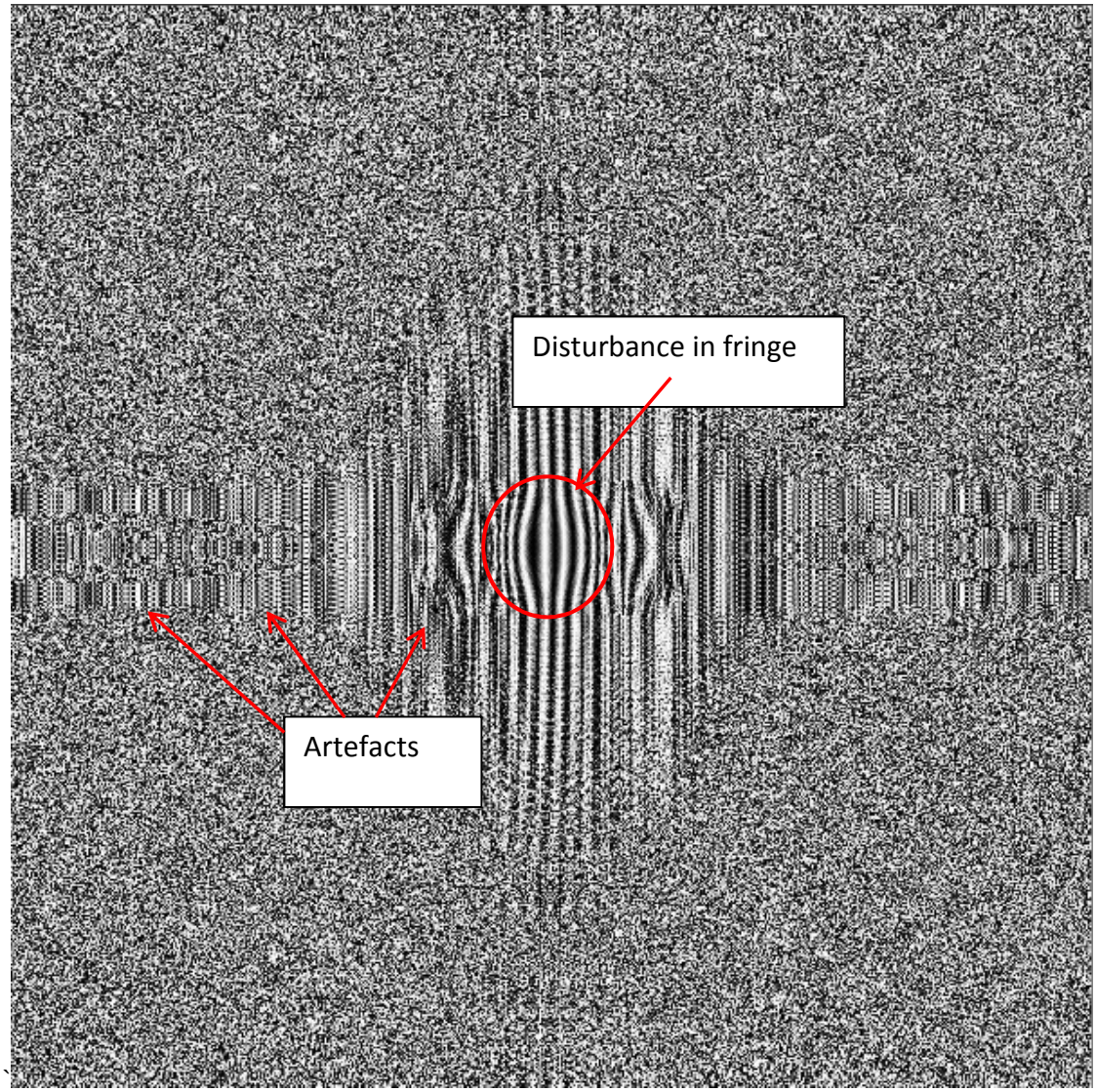

Figure 27 Simulated shearography fringe pattern on the whole surface of a 200mm x 200mm plate for FEM simulation FEM-2. Shearing distance: 1mm.

Copyright © DashWin Consortium 2012

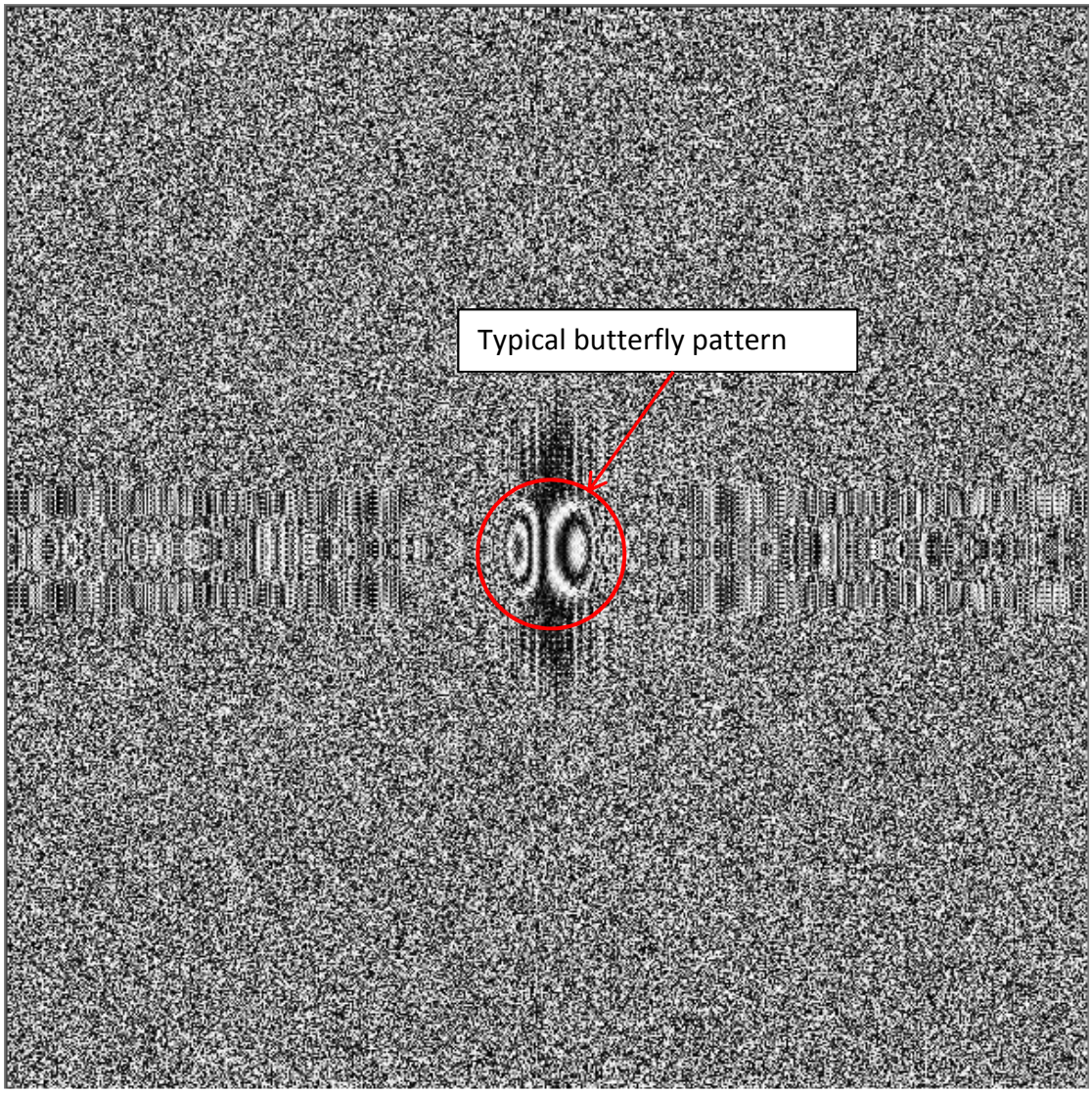

Figure 28 Simulated shearography fringe pattern on the whole surface of a 200mm x 200mm plate for FEM simulation FEM-2. The carrier fringes of Figure 27 are excluded to highlight the typical butterfly pattern caused by a subsurface defect. Shearing distance: 1mm.

Copyright © DashWin Consortium 2012

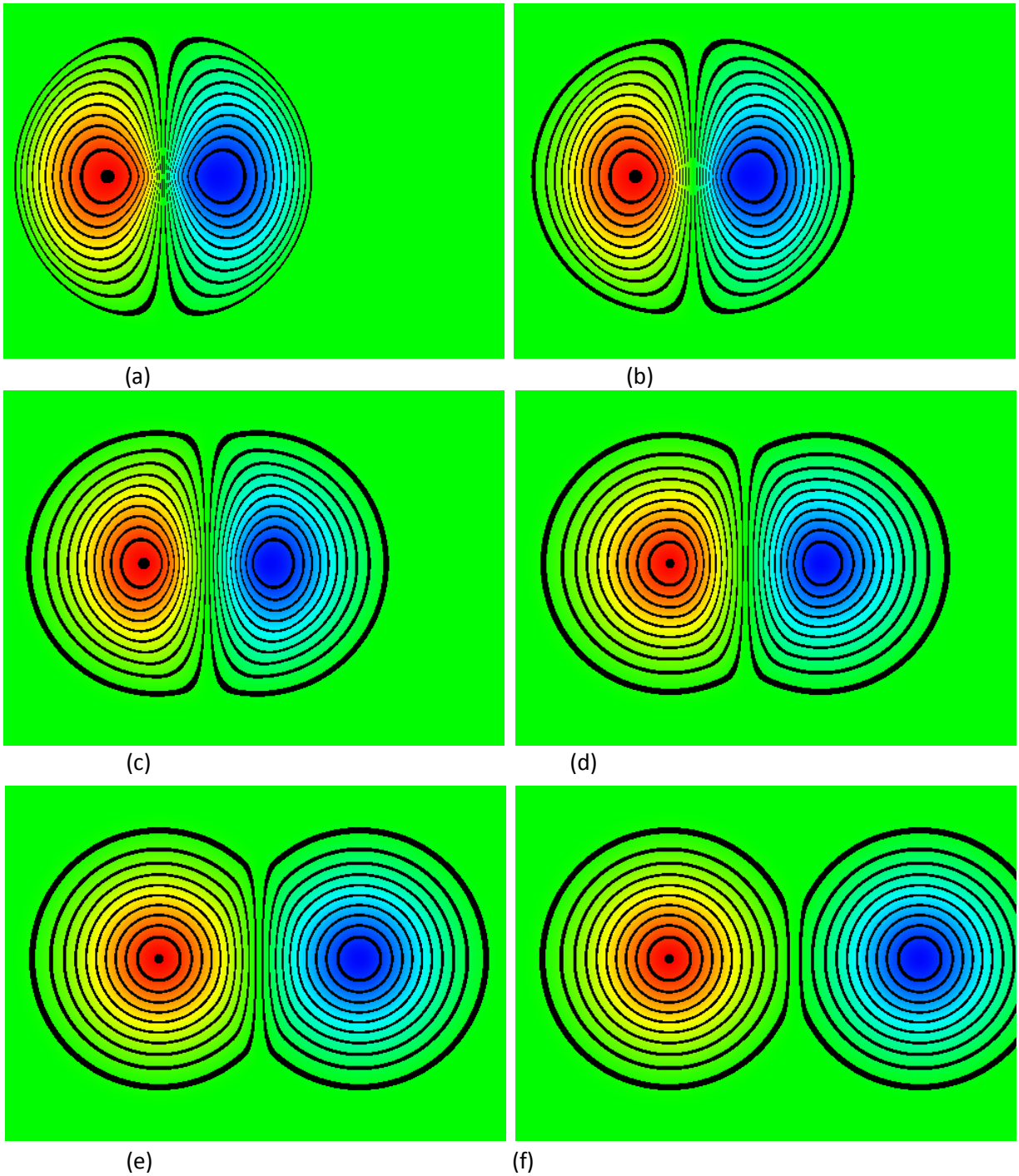

Figure 29 Shearography fringe patterns of a void defect with 30mm in diameter. The shearing magnitude is: (a) 1mm; (b) 5mm; (c) 10mm; (d) 15mm; (e) 20mm; and (f) 25mm.

Copyright © DashWin Consortium 2012

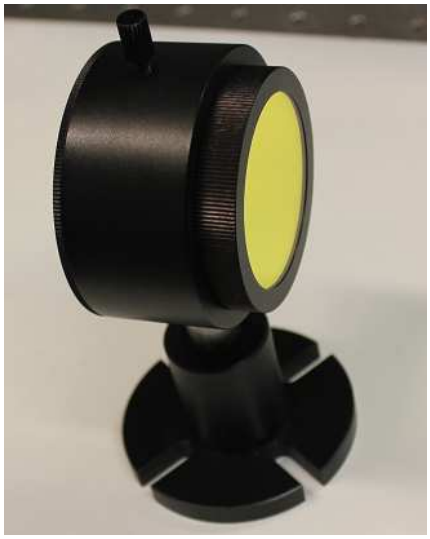

Figure 30 Image shearing device. It consists of a Wollaston prism, a polariser and a band-pass filter.

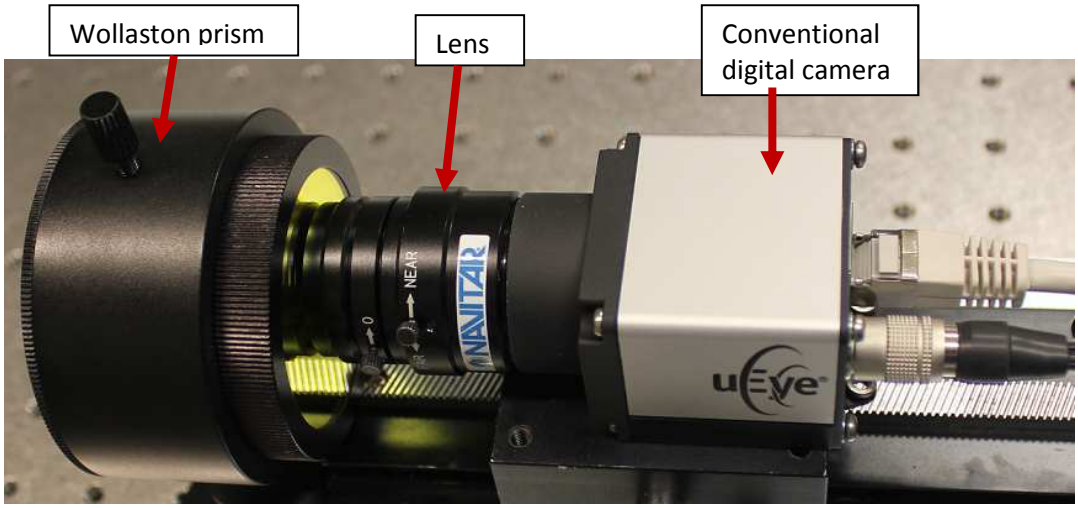

(a)

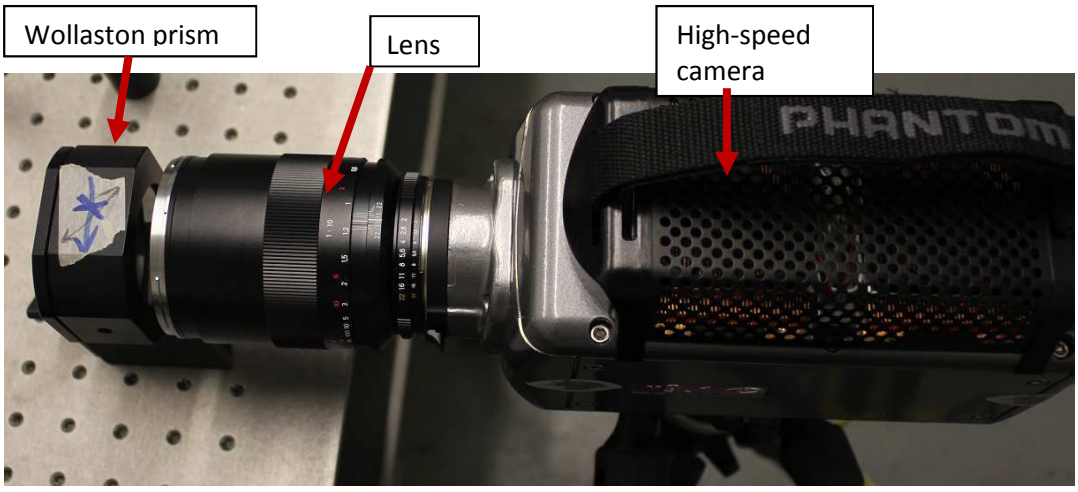

(b)

Figure 31 Two shearography set-ups with a Wollaston prism. (a) With a conventional digital camera. (b) With a high speed camera. Note: the laser beam is not included.

Copyright © DashWin Consortium 2012

(a)

(b)

Figure 32 Two types of heating lamps were used. (a) Two 400W halogen heating lamps. (b) A 1000W infrared heating lamp**.**

Copyright © DashWin Consortium 2012

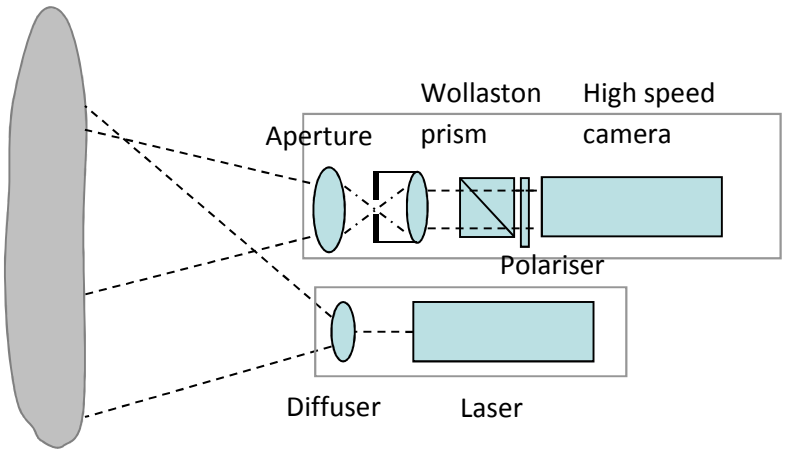

(a)

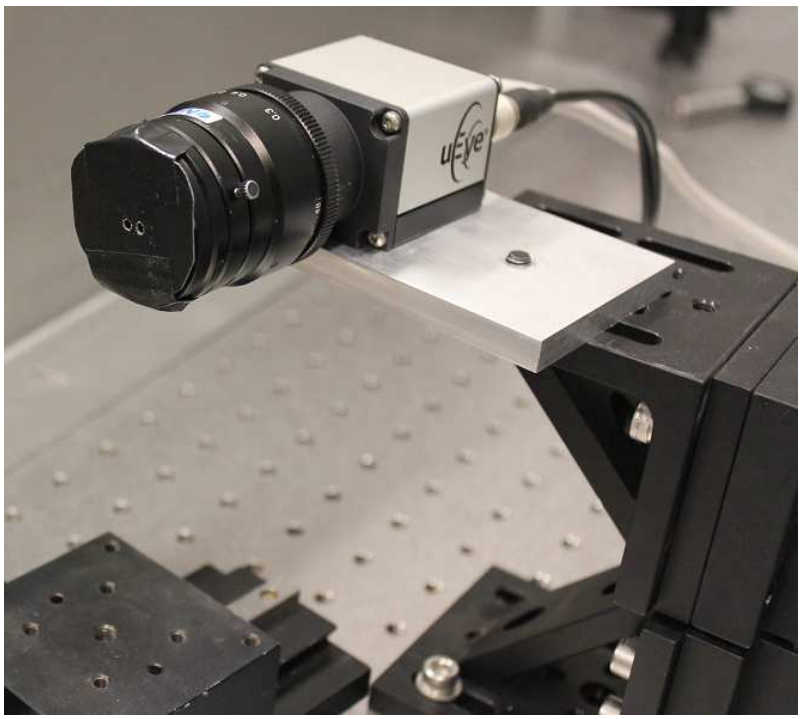

(b)

Figure 33 A spatially phase shifted shearography system with a double-hole aperture. (a) Diagram of optical set-up. (b) Camera with a double-hole aperture placed on the front focal plane of the lens.

Copyright © DashWin Consortium 2012

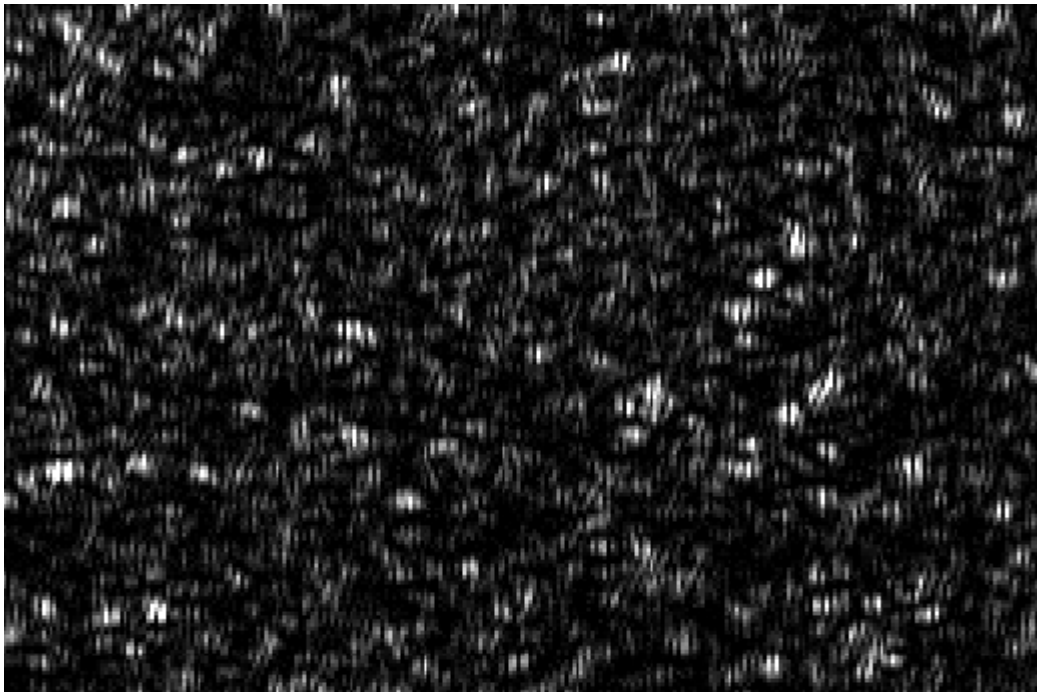

Figure 34 Specklegram showing the carrier fringes modulating the speckles.

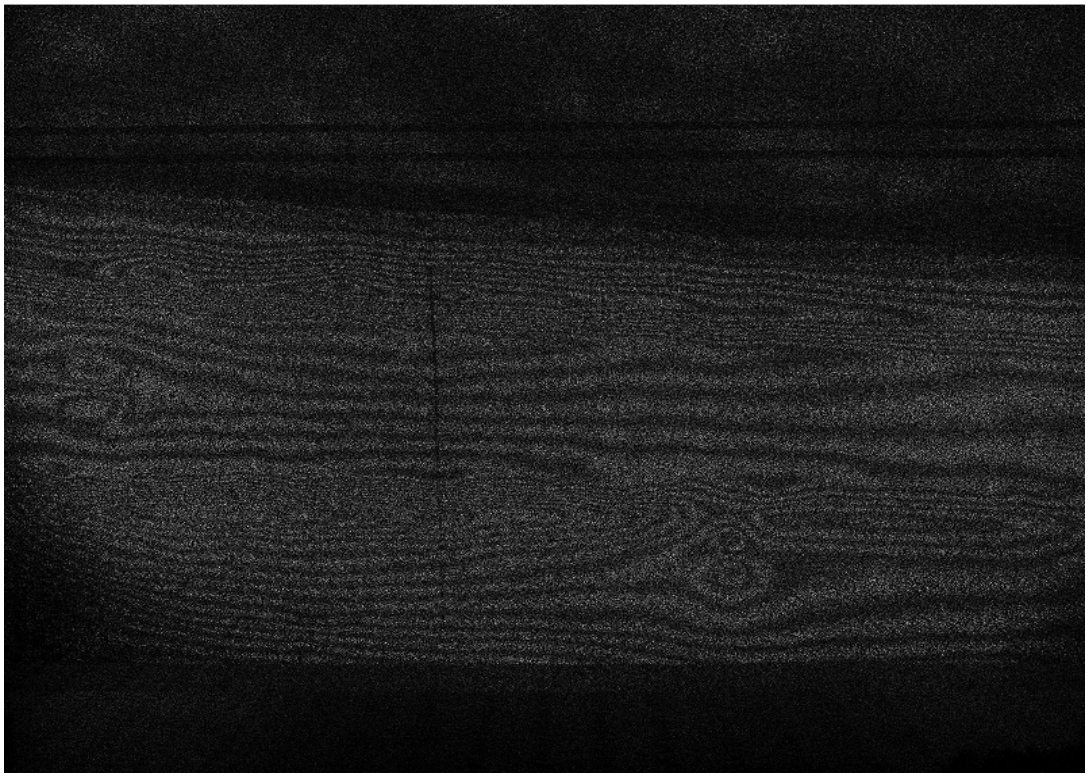

Figure 35 Shearography fringe pattern with heightened density due to further deformation

Copyright © DashWin Consortium 2012

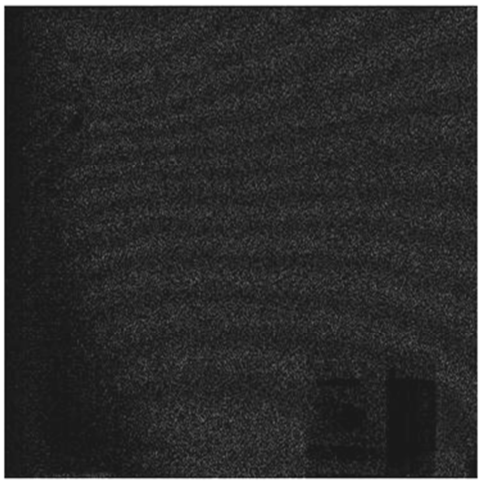

(a)

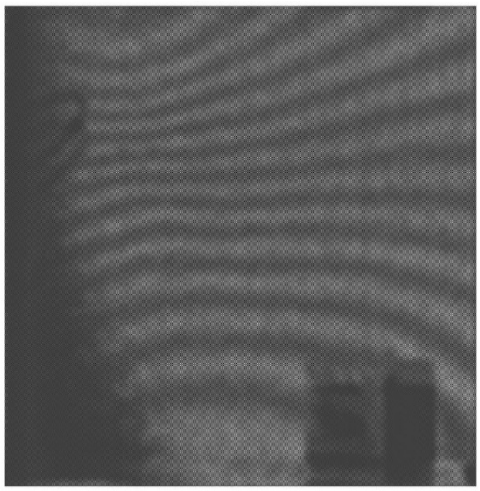

(b)

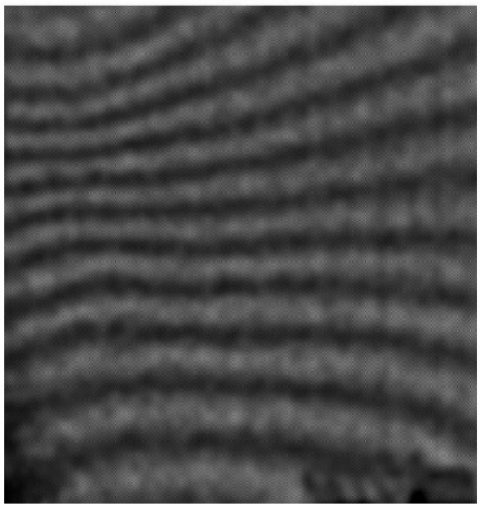

(c)

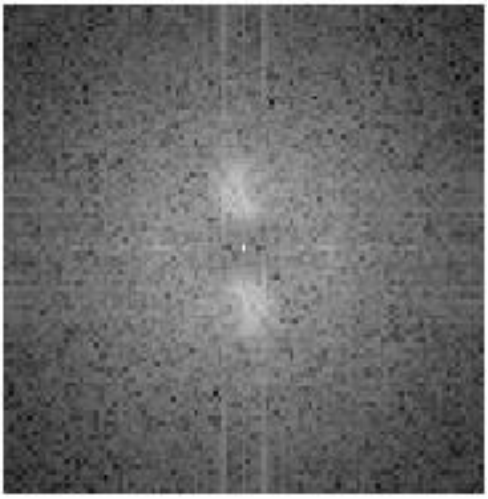

(d)

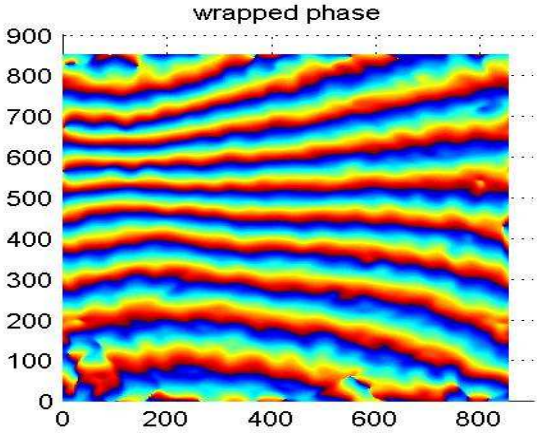

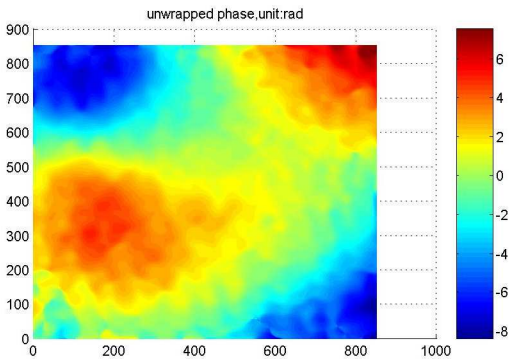

(e) (f)

Copyright © DashWin Consortium 2012

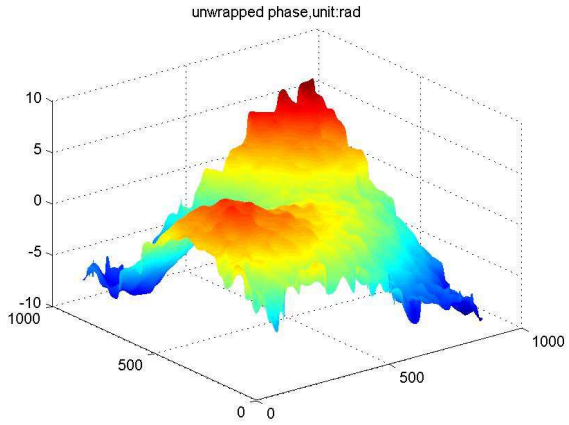

(g)

Figure 36 Analysis of shearography fringe by FTM method: (a) One of the original shearography fringe patterns. (b) Fringe pattern after low-pass filtering. (c) Central part of the fringe pattern. (d) Spectrum of (c). (e) Wrapped phase of (c) and (f & g) the unwrapped phase of (e).

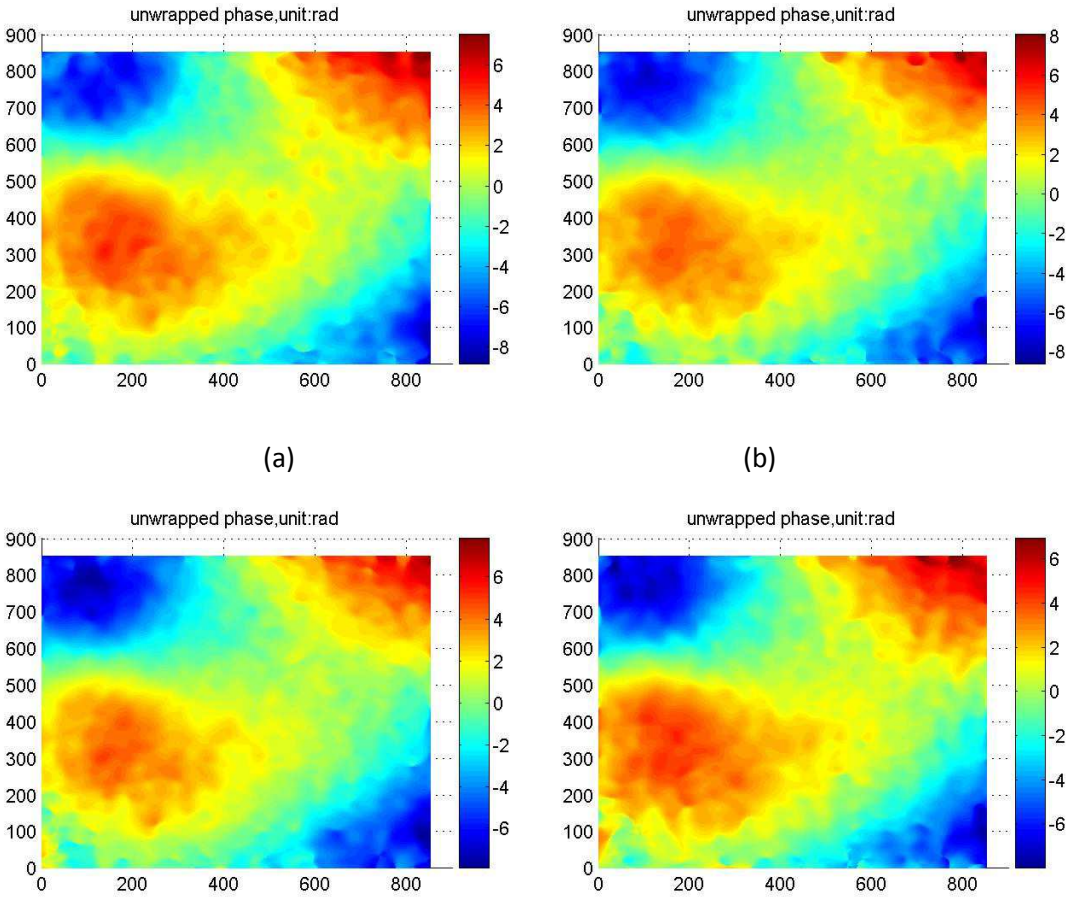

(a) (b)

(c) (d)

Copyright © DashWin Consortium 2012

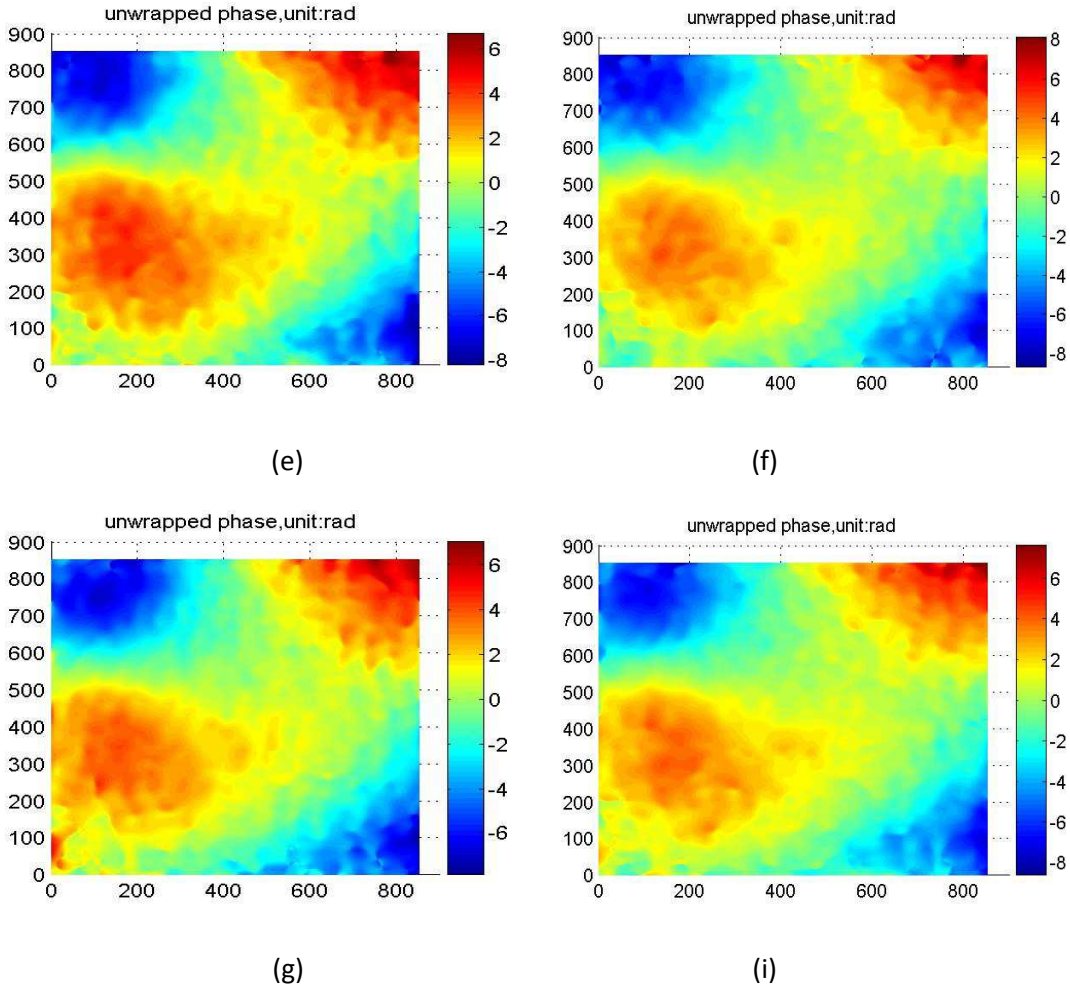

Figure 37 Extracted phase maps of eight speckle fringe patterns acquired in succession (the background phase has been removed).

Copyright © DashWin Consortium 2012

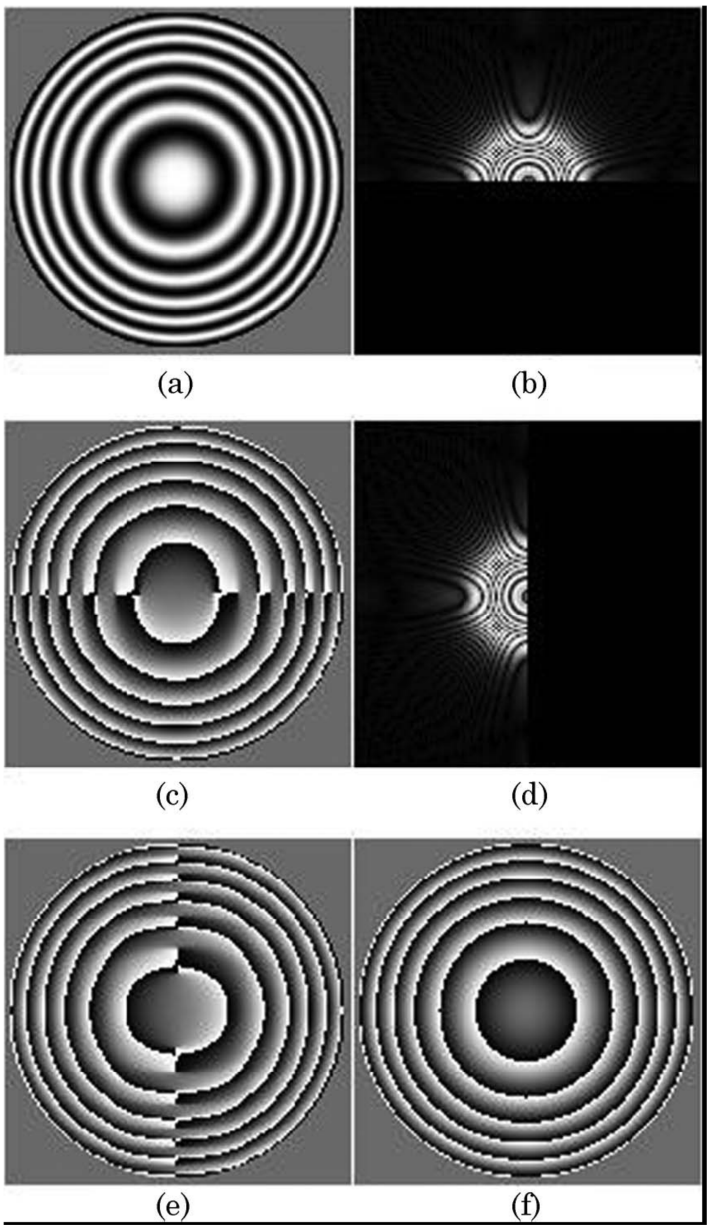

Figure 38 Results of applying the Fourier method to process a circular fringe pattern: (a) A fringe pattern with closed fringes. (b) Filtered Fourier spectrum. (c) The resulting wrapped phase (x direction). (d) Filtered Fourier spectrum, (e) The resulting wrapped phase (y direction), and (f) The actual wrapped phase.

Copyright © DashWin Consortium 2012

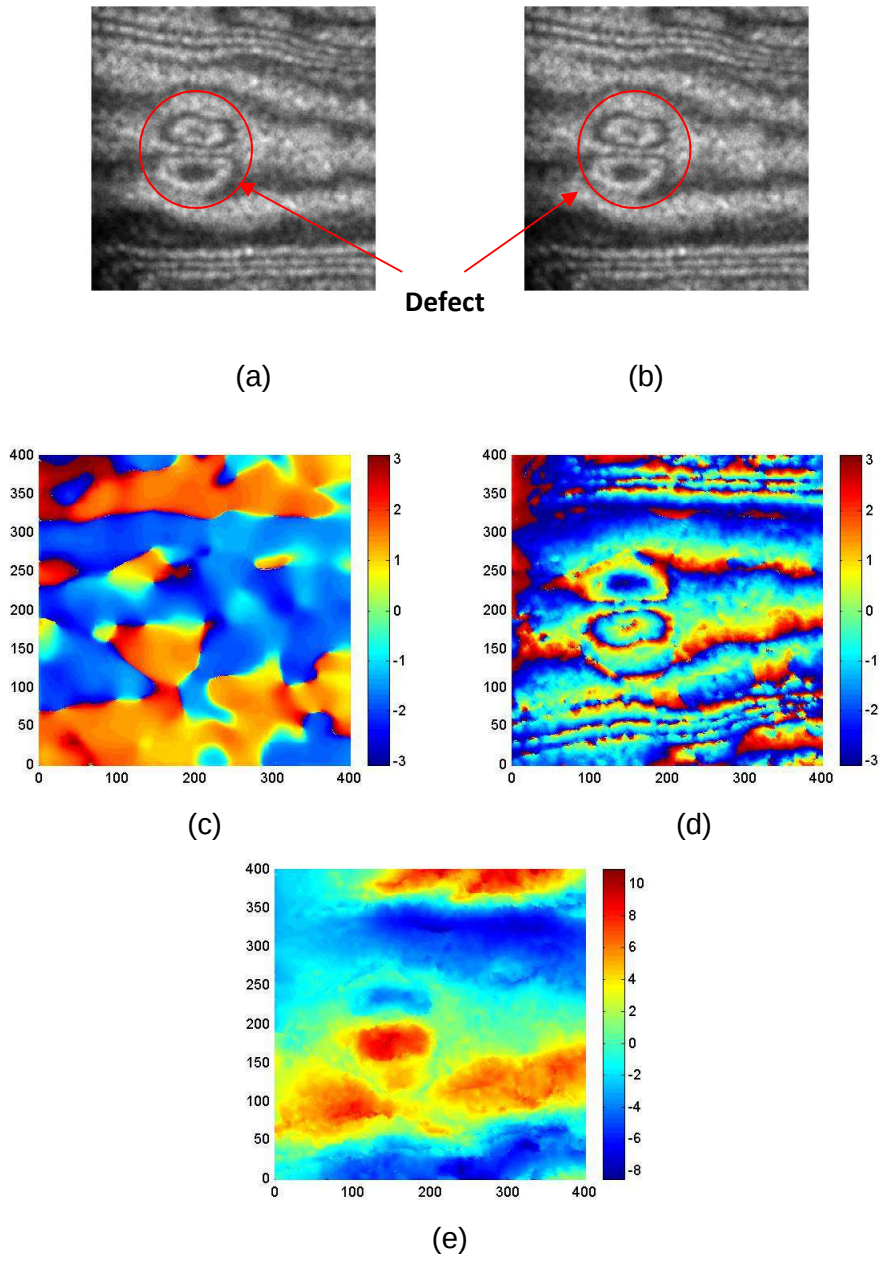

Figure 39 Experimental results of phase extraction from shearography fringes by the two-step approach: (a&b) are two shearography fringes captured in succession, (c) is the direction map of (a), and (d&e) are the extracted wrapped and unwrapped phases of (a).

Copyright © DashWin Consortium 2012

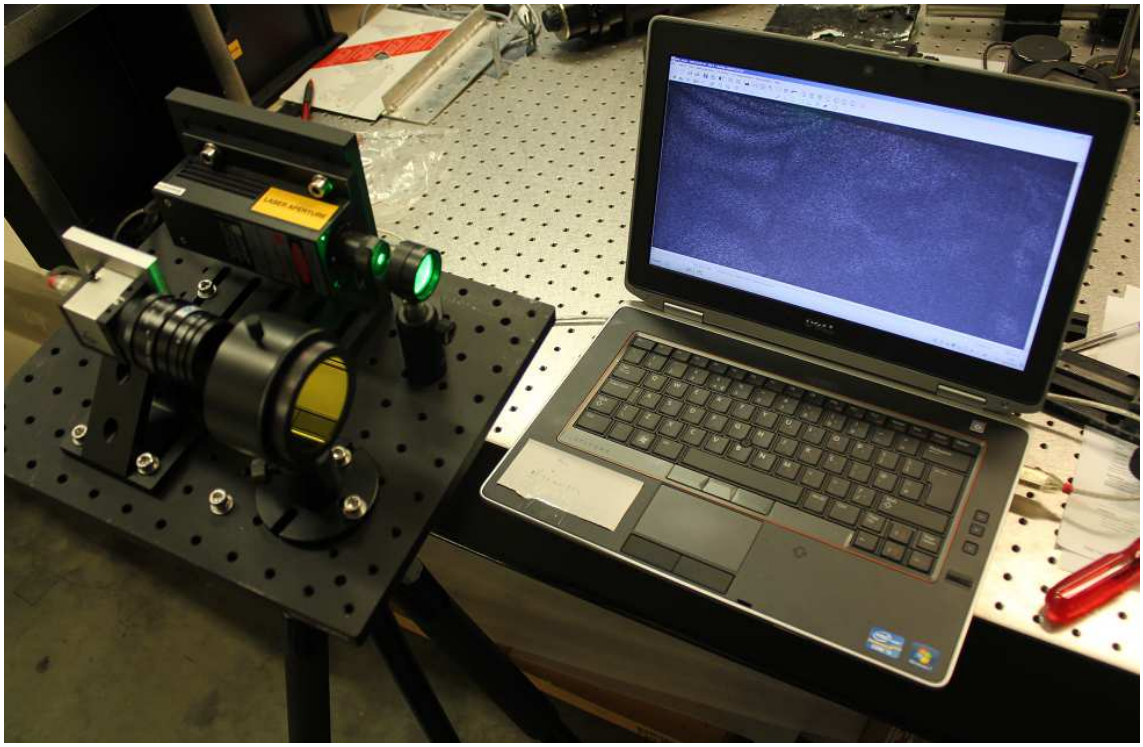

(a)

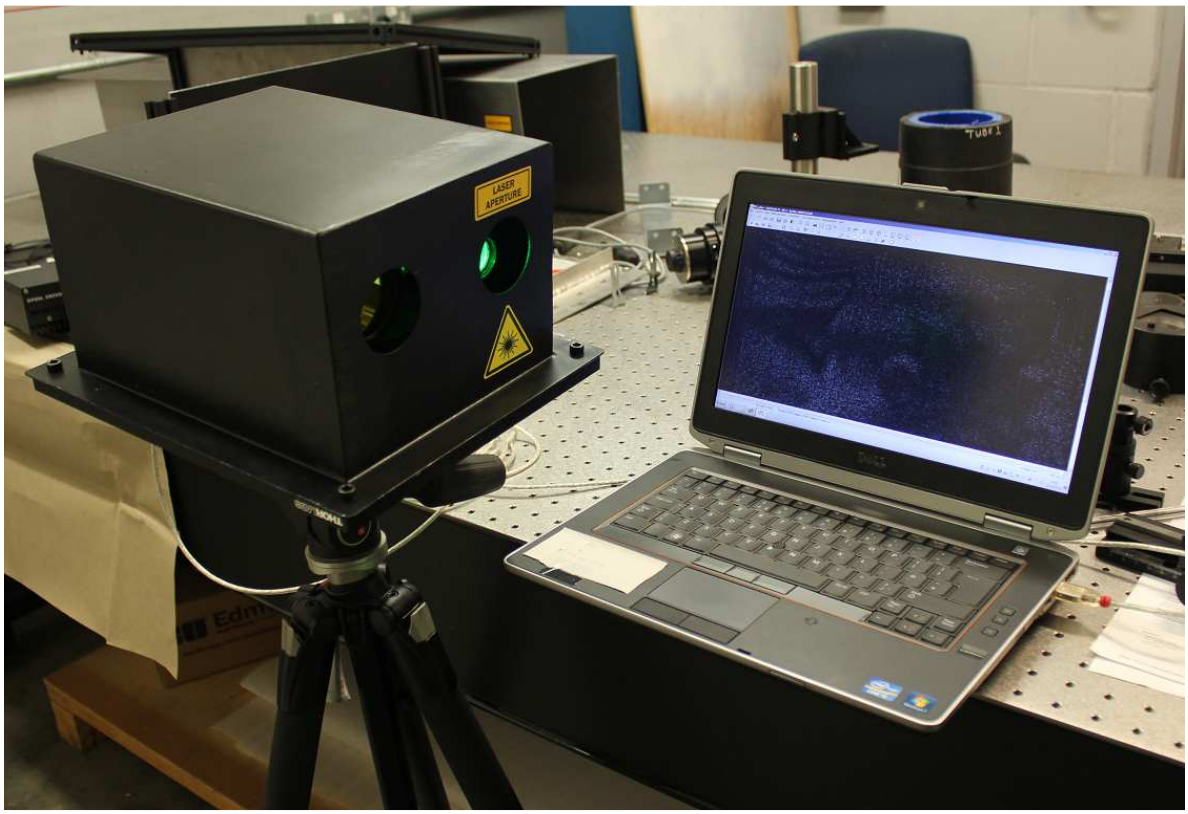

(b)

Figure 40 A compact shearography system. (a) The protective case is open

Copyright © DashWin Consortium 2012

Figure 41 A trial of the compact DashWin shearography system at Scottish & Southern Energy (Glasgow, Scotland).

Copyright © DashWin Consortium 2012

Figure 42 Experimental setup for rigid body motion measurement of a WTB suspended from a test frame.

Copyright © DashWin Consortium 2012

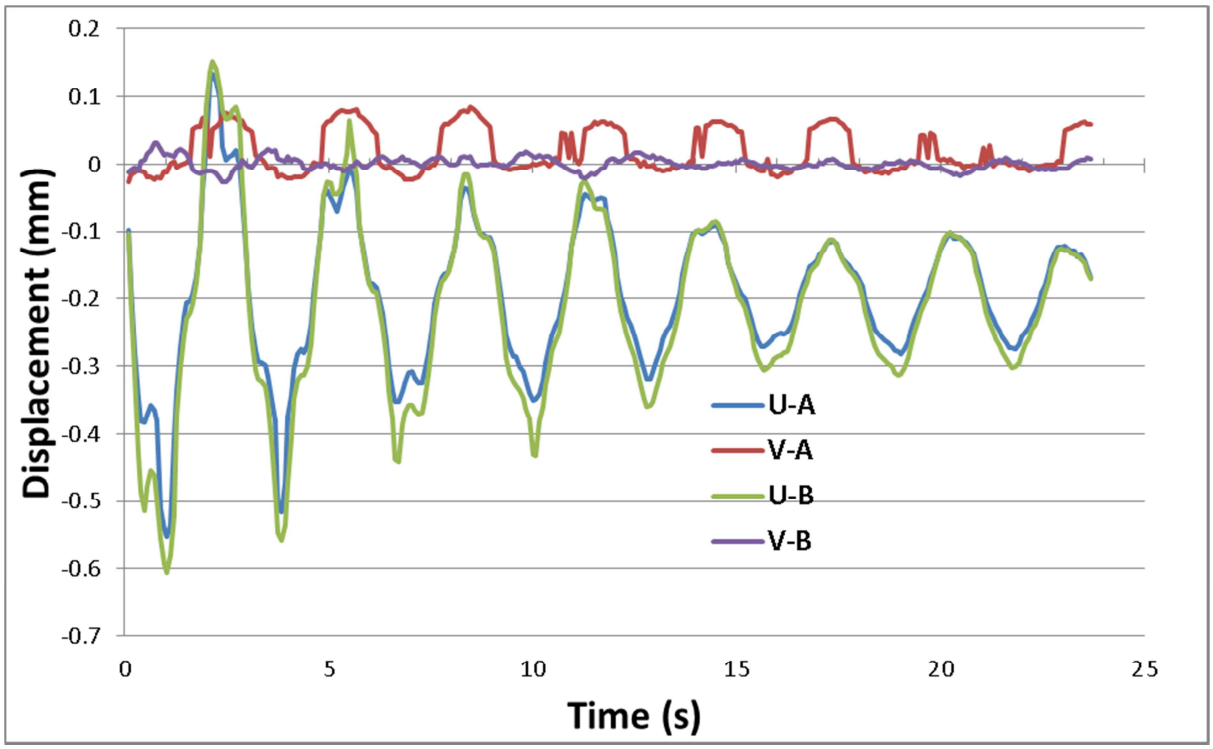

Figure 43 Typical in-plane motion history of the WTB section. Point A is located near the middle of the blade; Point B is located near the edge of the blade.

Figure 44 Flag pole used in rigid body motion measurement trials.

Copyright © DashWin Consortium 2012

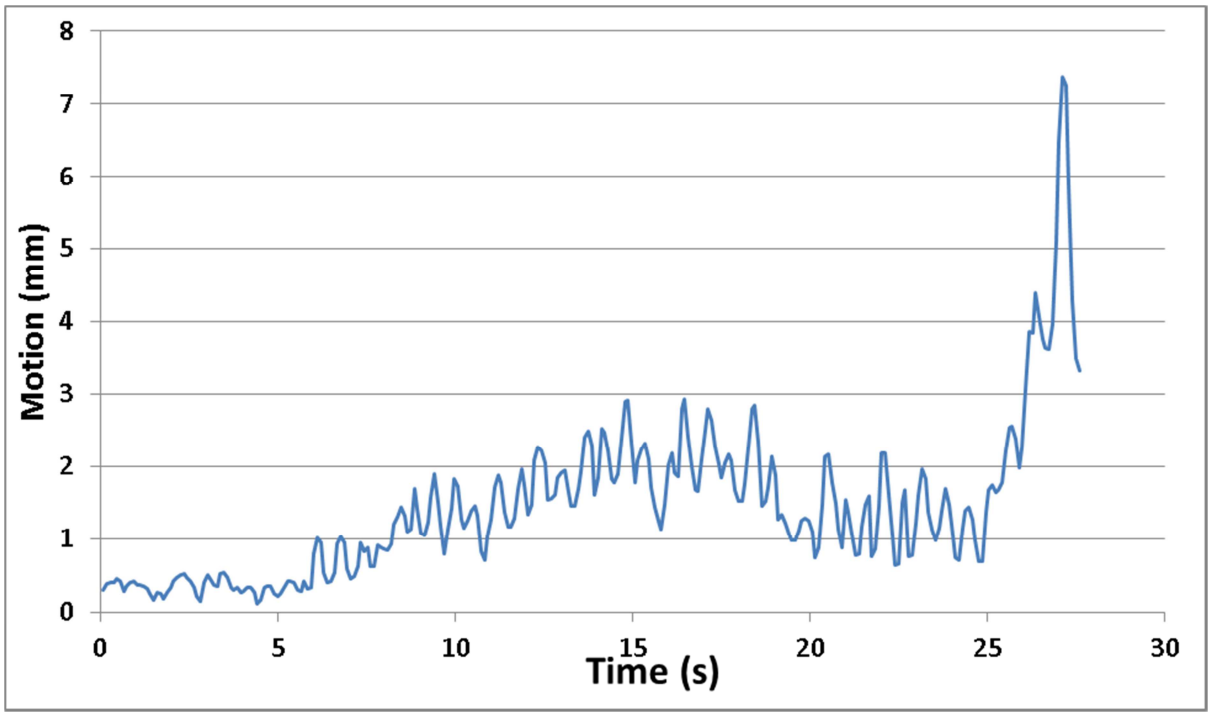

Figure 45 In-plane rigid body motion of the top of the flag pole over a 28 second period.

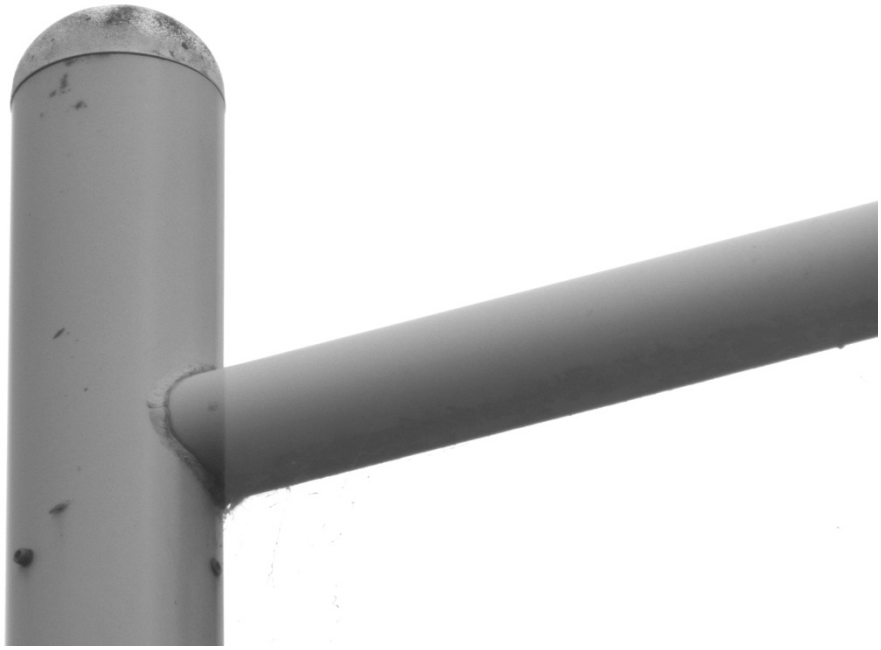

Figure 46 Lamp post used in rigid body motion measurement trials.

Copyright © DashWin Consortium 2012

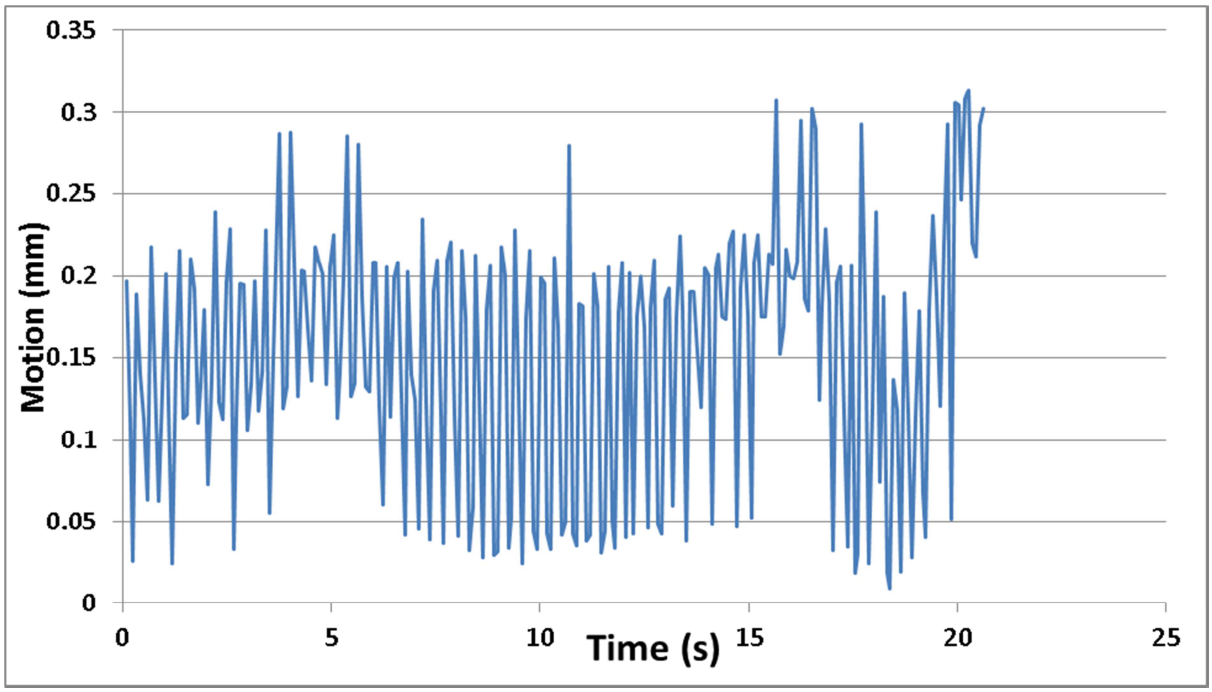

Figure 47 In-plane rigid body motion of the lamp post.

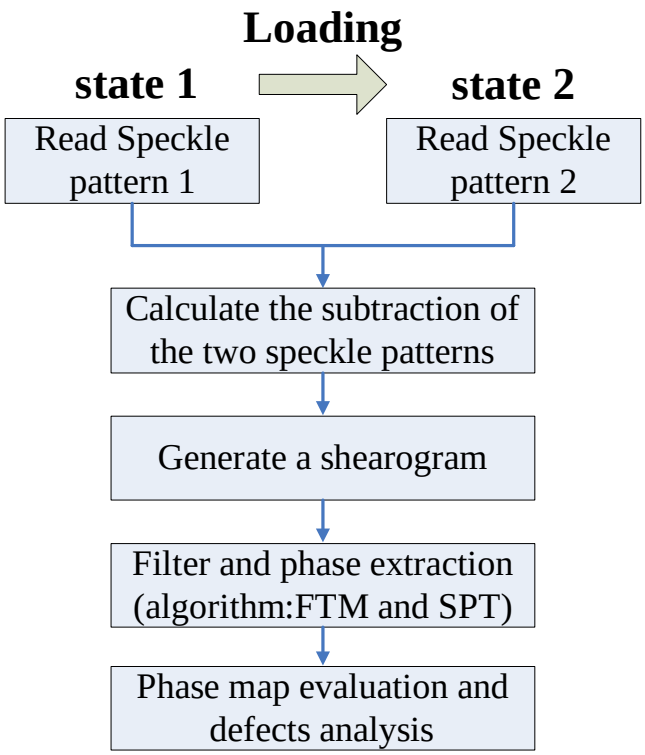

Figure 48 Flow chart of the Phase-of-Differences method.

Copyright © DashWin Consortium 2012

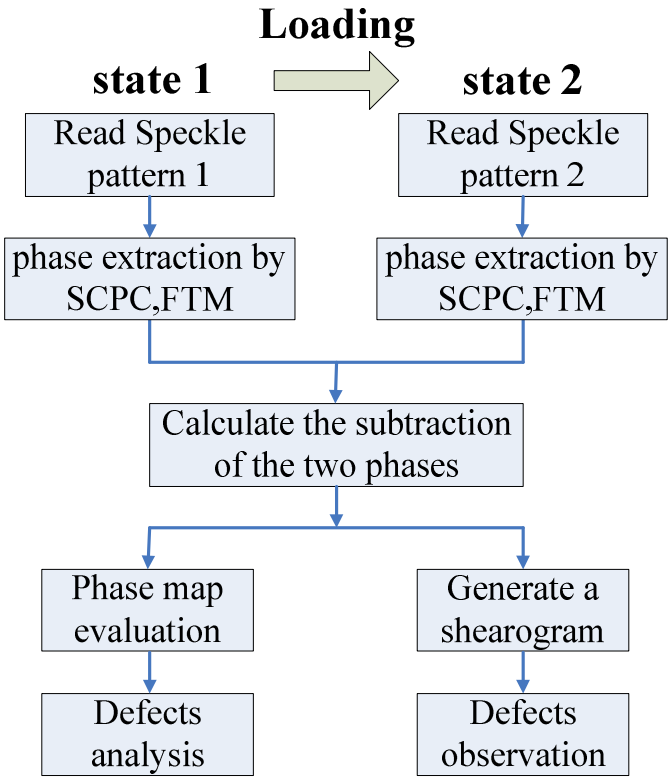

Figure 49 Flow chart of the difference-of-phases method.

Copyright © DashWin Consortium 2012

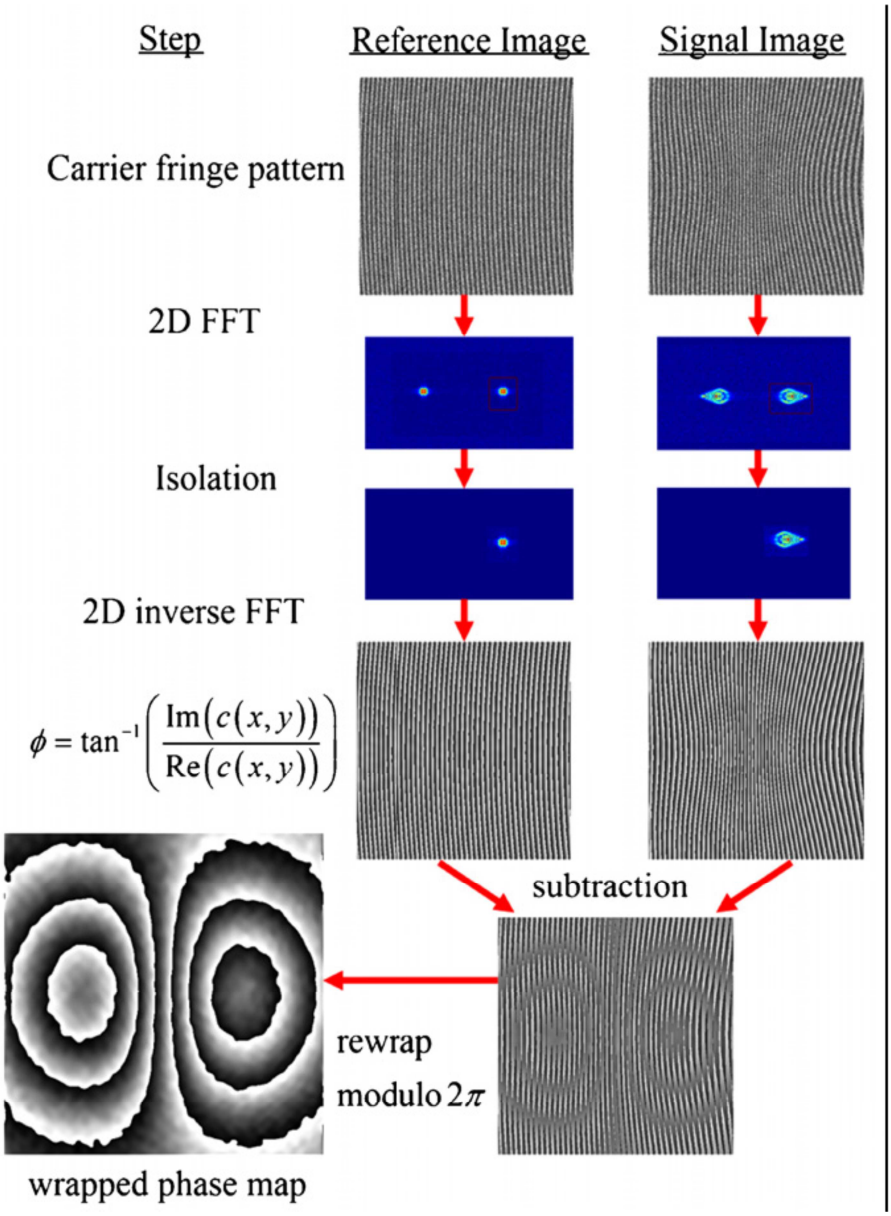

Figure 50 Sequence of processing steps used in Difference-of-Phases method with FTM.

Copyright © DashWin Consortium 2012

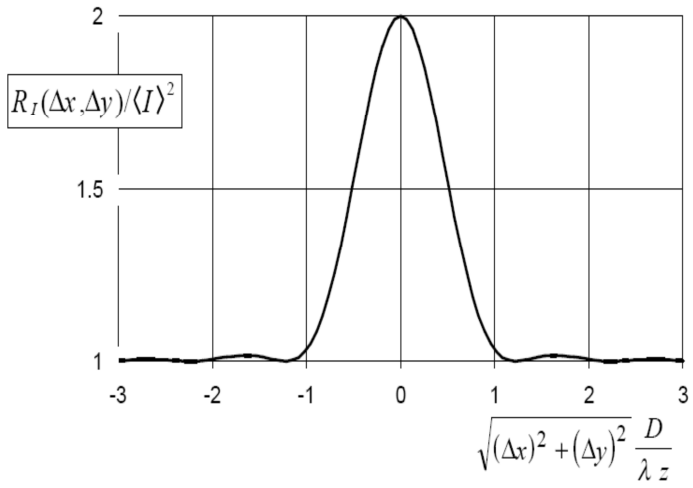

(a)

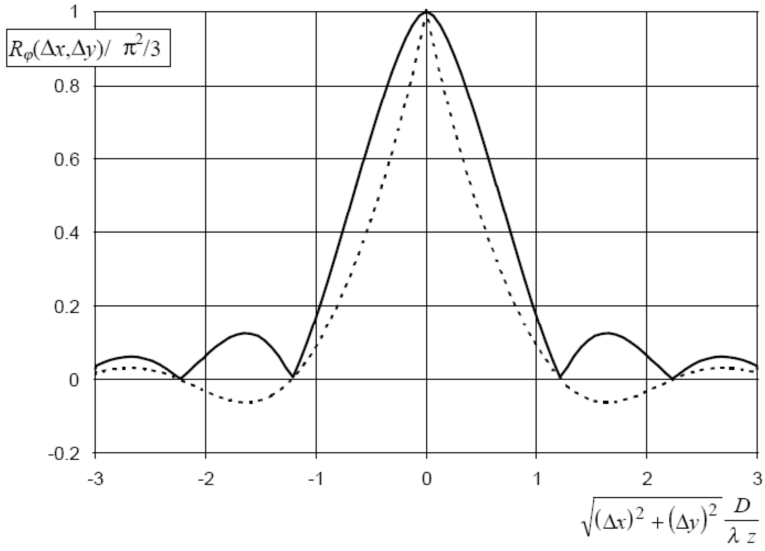

(b)

Figure 51 Characteristics of speckle autocorrelation. (a) The speckle intensity autocorrelation function and (b) the speckle phase autocorrelation function. The solid line corresponds to the phase autocorrelation functions for continuous phase, while the broken line is for discontinuous phases.

Copyright © DashWin Consortium 2012

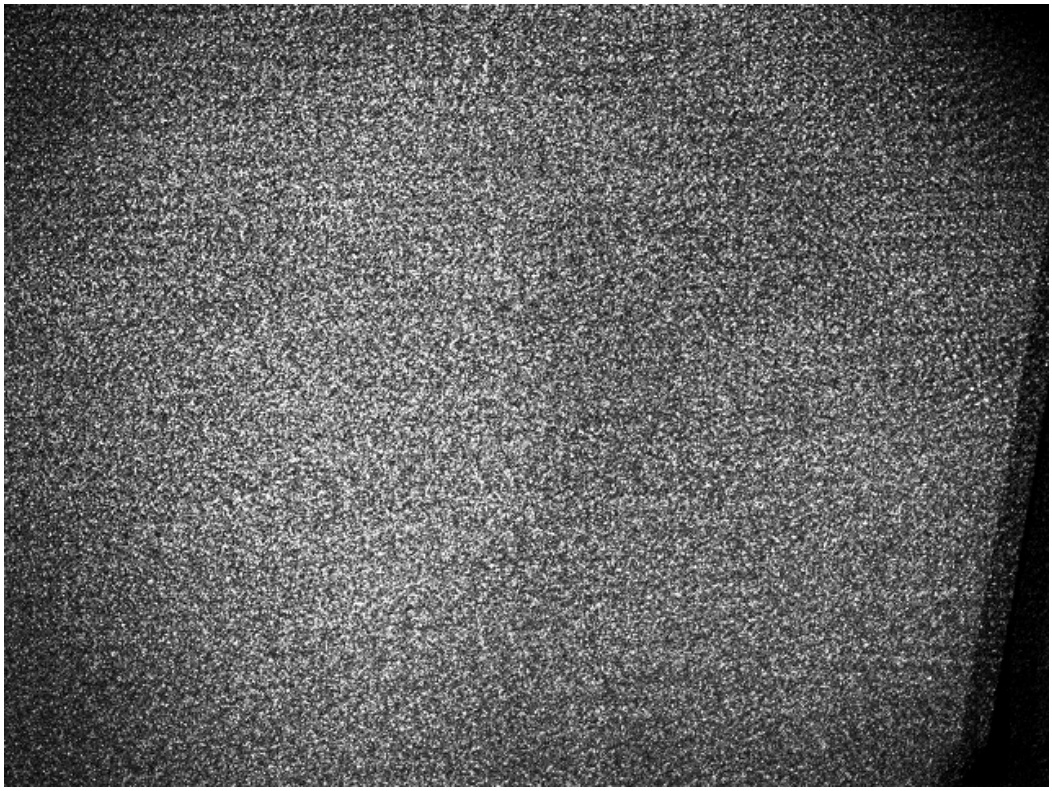

(a)

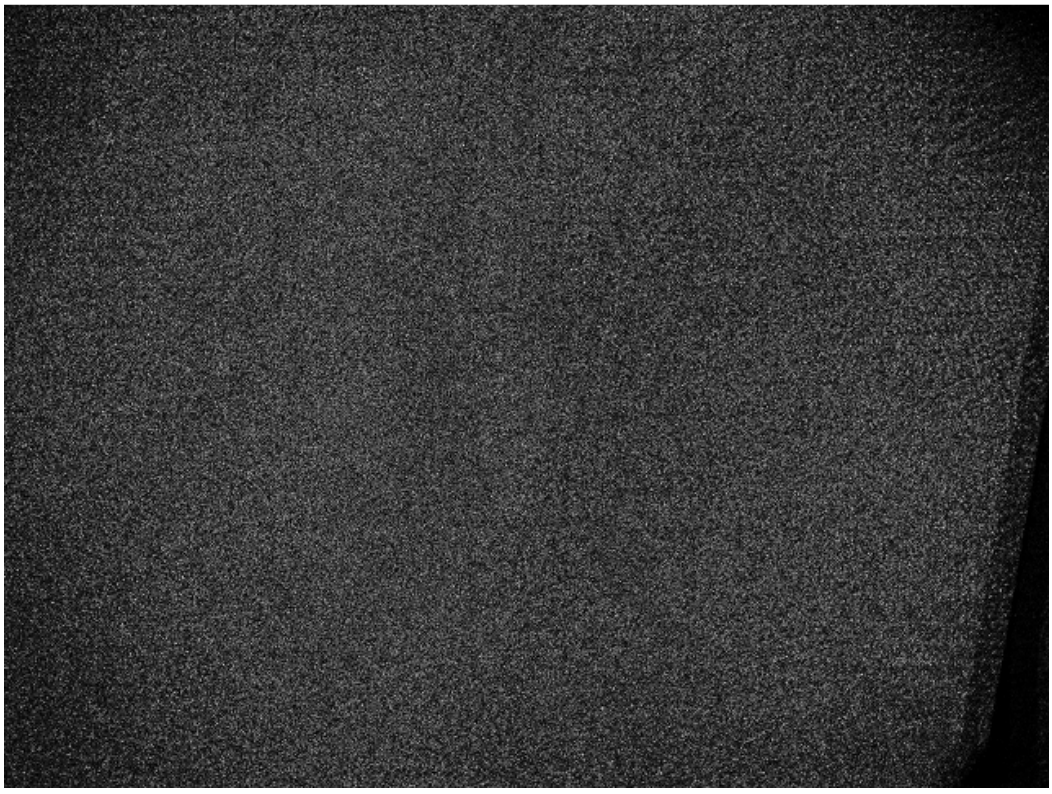

(b)

Copyright © DashWin Consortium 2012

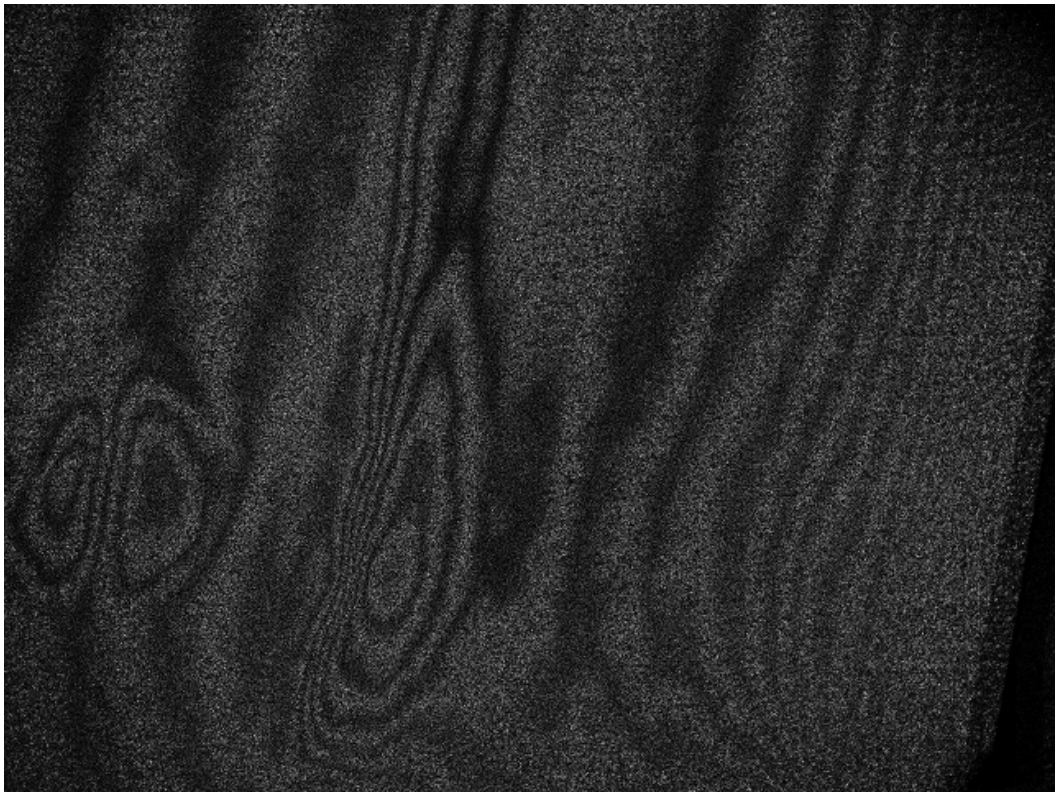

(c)

Figure 52 Laboratory test on a suspended WTB sample to validate the new procedure. (a) A typical speckle image of the sample at an instant. (b) Shearography fringe pattern from to uncorrelated speckle images produced by image subtraction. (c) Clear shearography fringe image from two correlated speckle images showing a defect on the left hand side.

Copyright © DashWin Consortium 2012

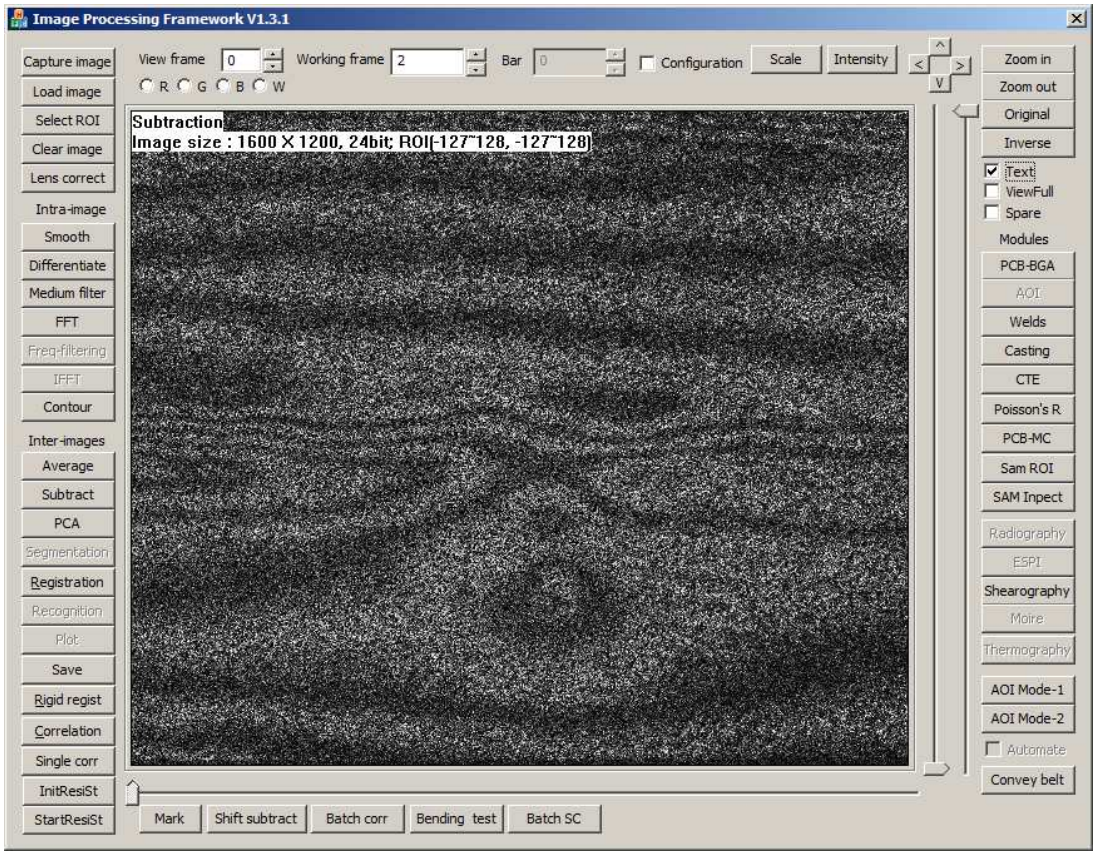

Figure 53 The main interface of the DashWin IPS (image processing system) software which incorporates shearography, DIC and other image based techniques.

Copyright © DashWin Consortium 2012

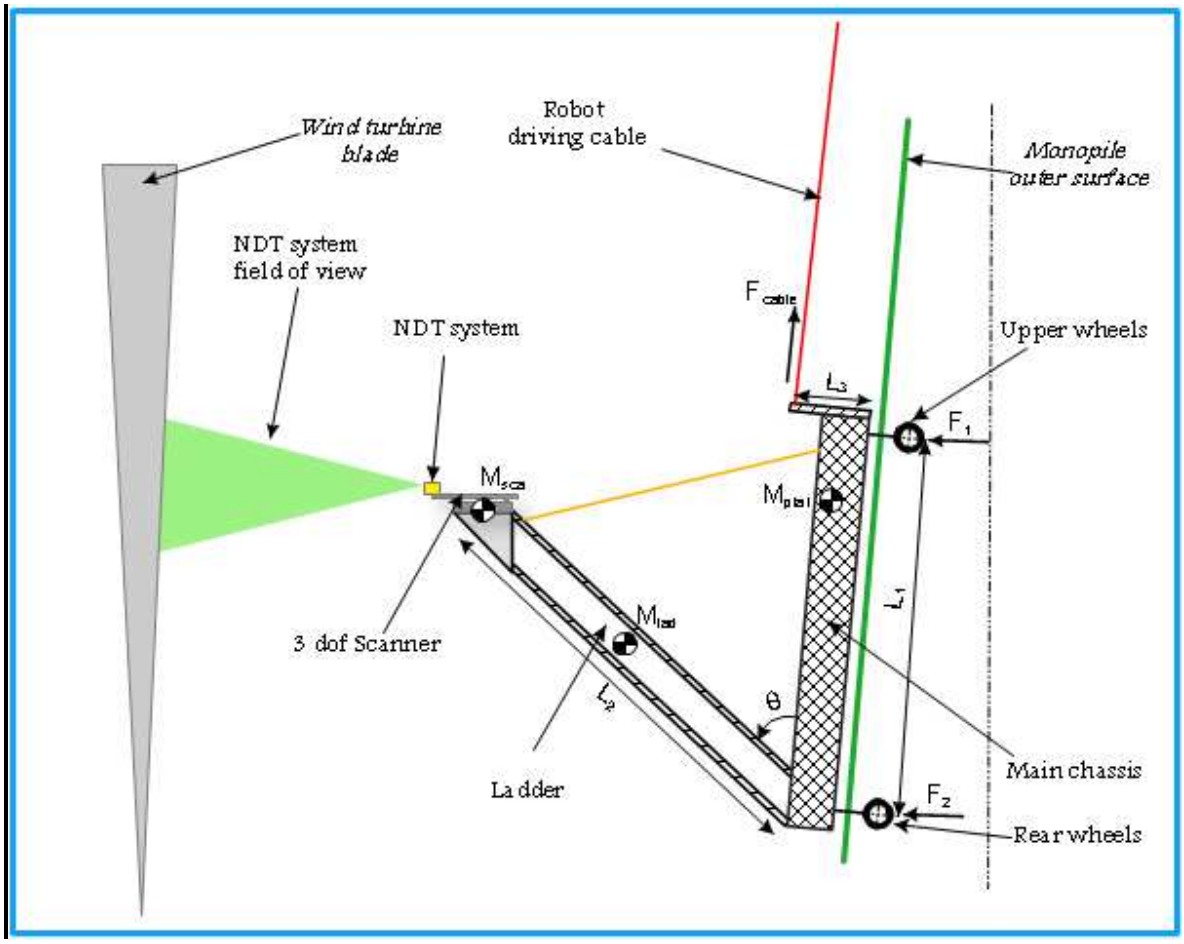

Figure 54 Concept of the robotic platform: a system overview.

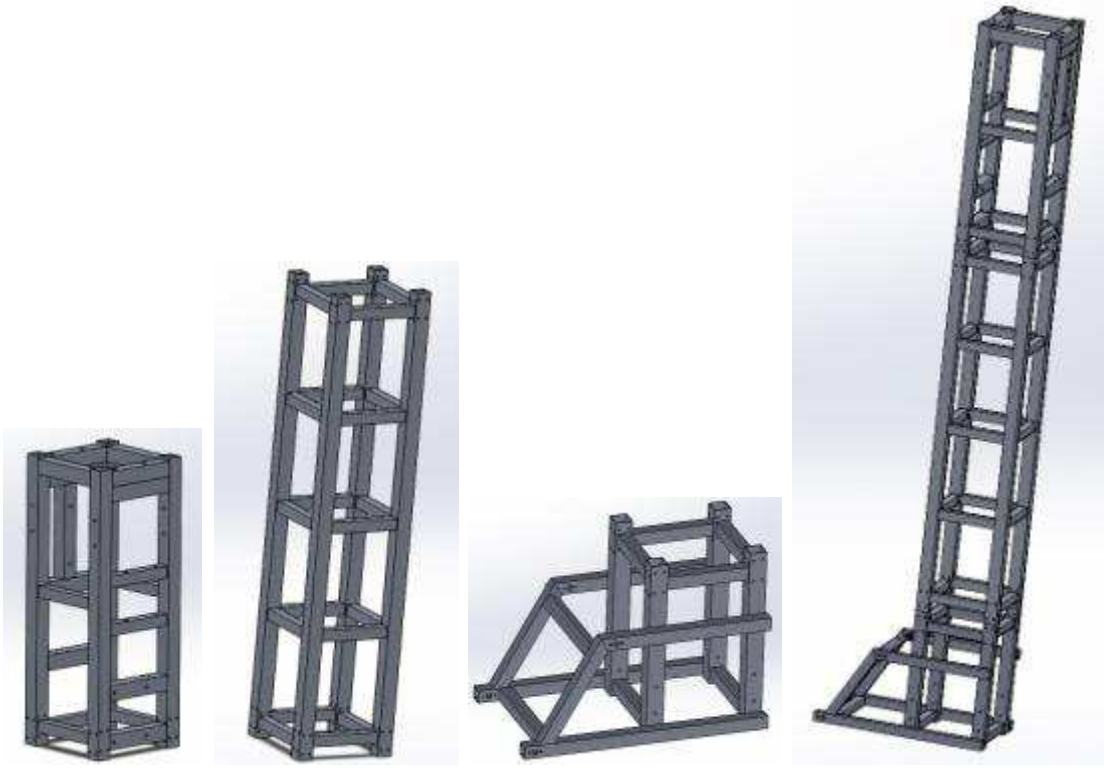

Copyright © DashWin Consortium 2012

Figure 55: Main chassis of the vehicle (upper/middle/bottom and assembled).

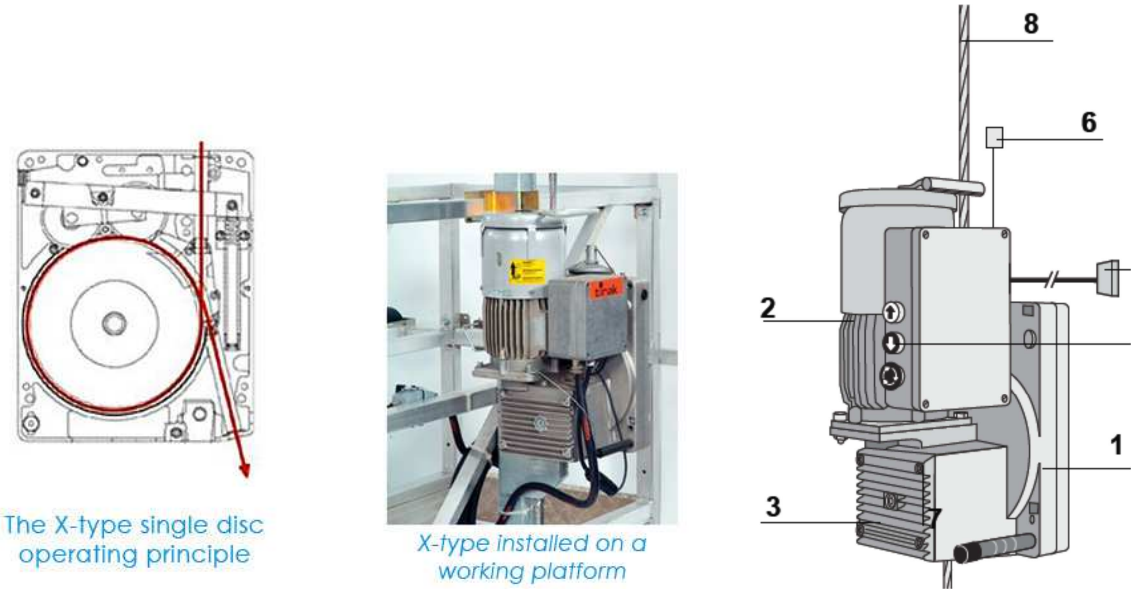

Figure 56 Winches principle of operation .

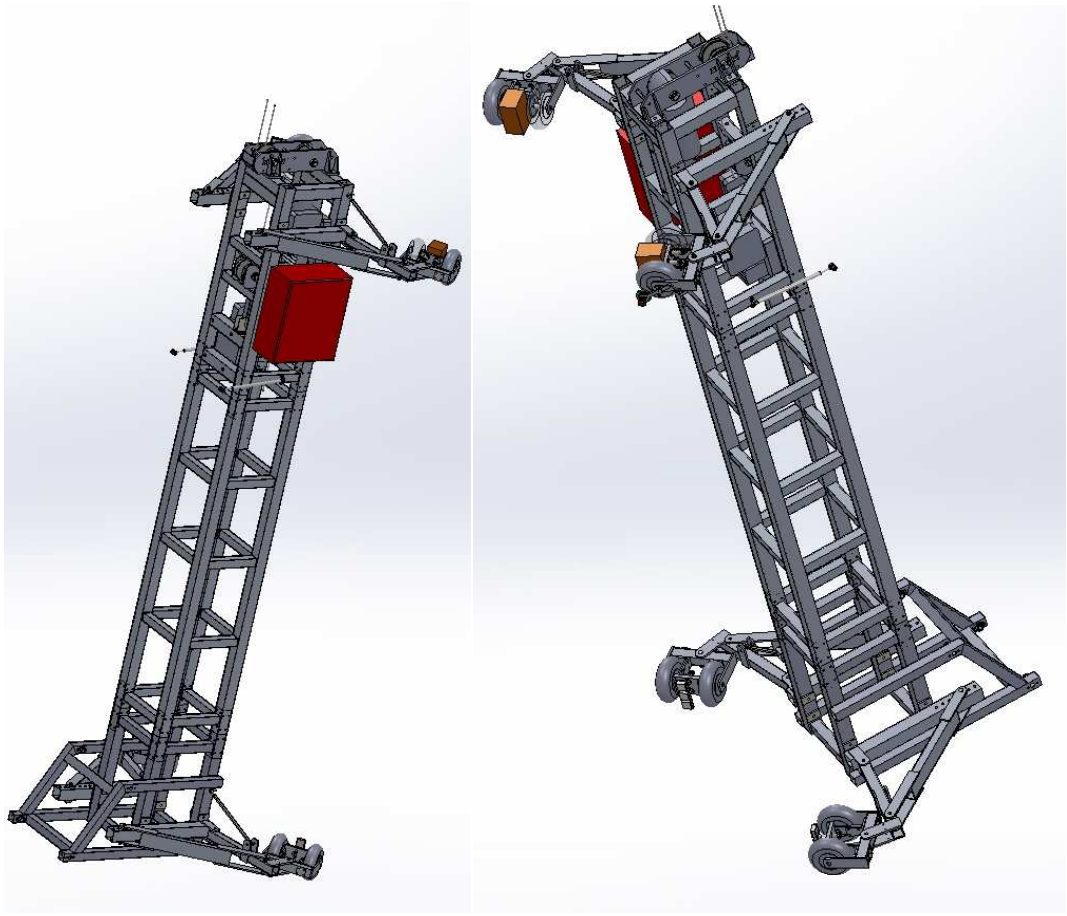

Figure 57 CAD snapshots of the assembled “vehicle”.

Copyright © DashWin Consortium 2012

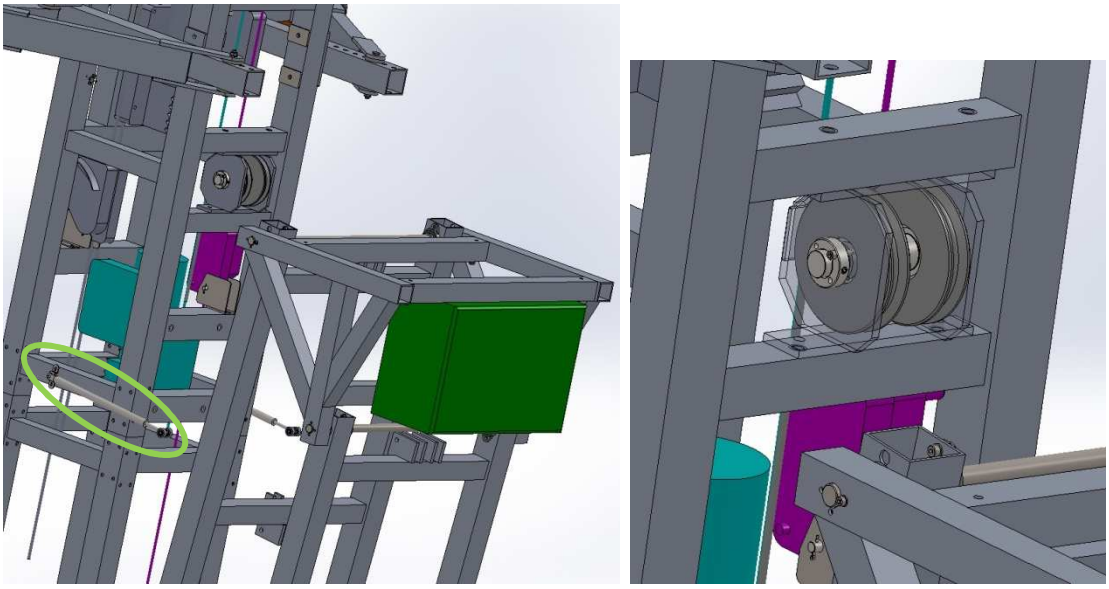

Figure 58 CAD snapshots of the “ladder” pulley mechanism, winch and safety mechanism.

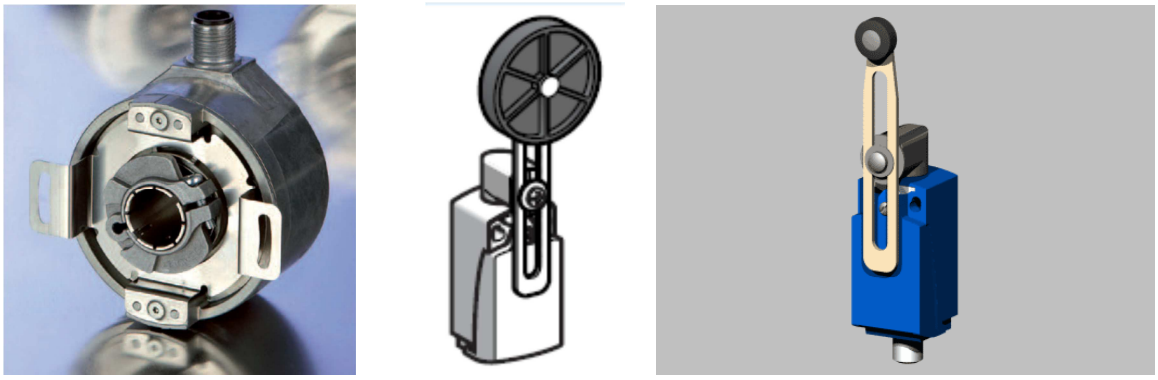

Figure 59 Absolute encoder of the ladder mechanism and limit contact sensor.

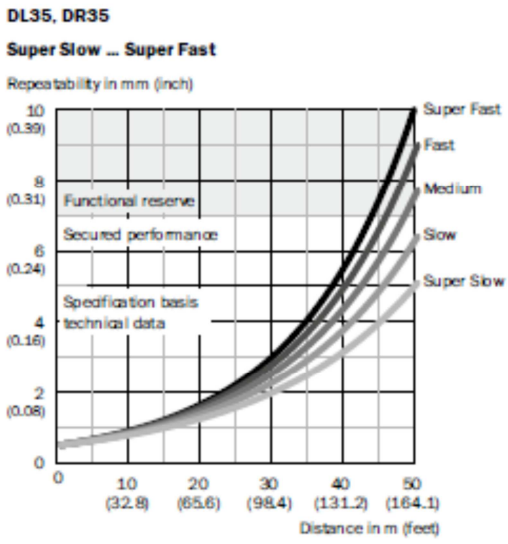

Figures 60 Long range laser sensor by manufactured by Sick Sensors**.**

Copyright © DashWin Consortium 2012

Figure 61 Short range precision laser sensor by Keyence.

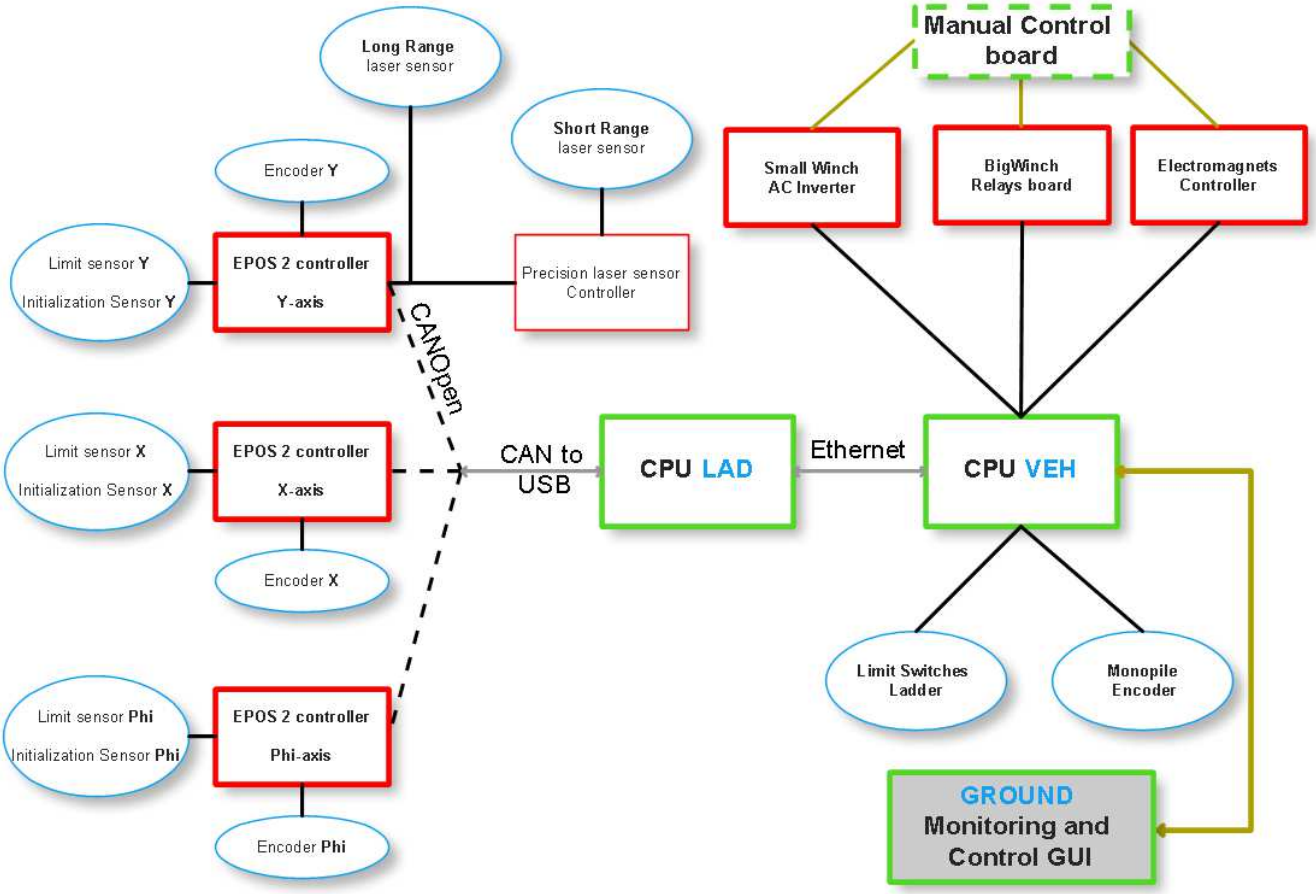

Figure 62 Schematic of the control system architecture.

Copyright © DashWin Consortium 2012

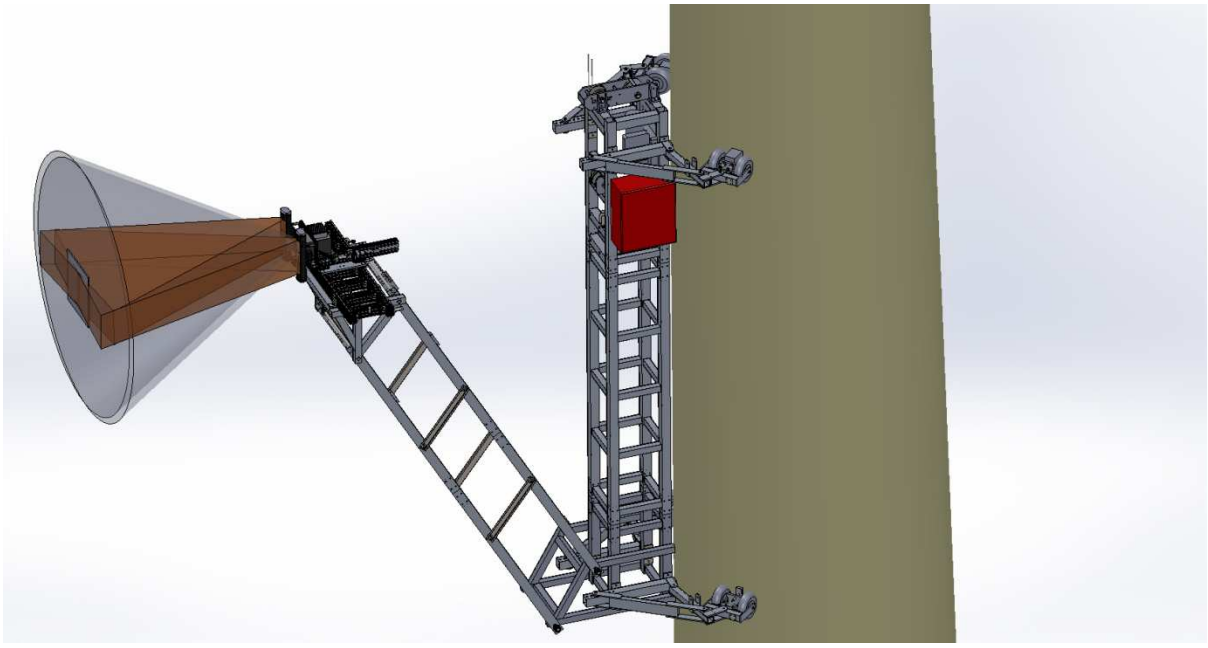

(a)

(b)

Copyright © DashWin Consortium 2012

(c)

Figure 63 3D CAD snapshots of the full system on the WT monopole.

Copyright © DashWin Consortium 2012

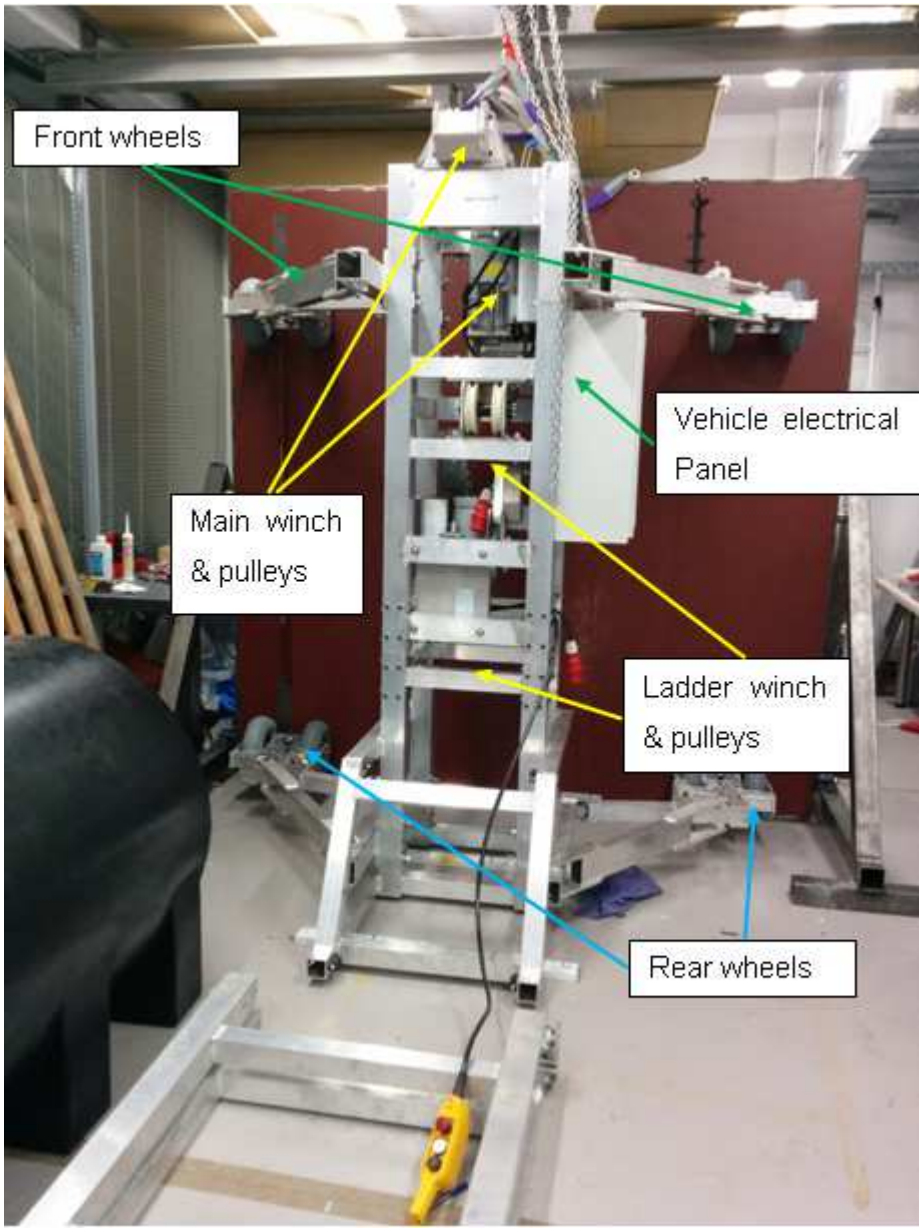

Figure 64 The short version of the robotic platform at an initial assembly stage.

Copyright © DashWin Consortium 2012

Figure 65 Extension of the robotic platform chassis.

Copyright © DashWin Consortium 2012

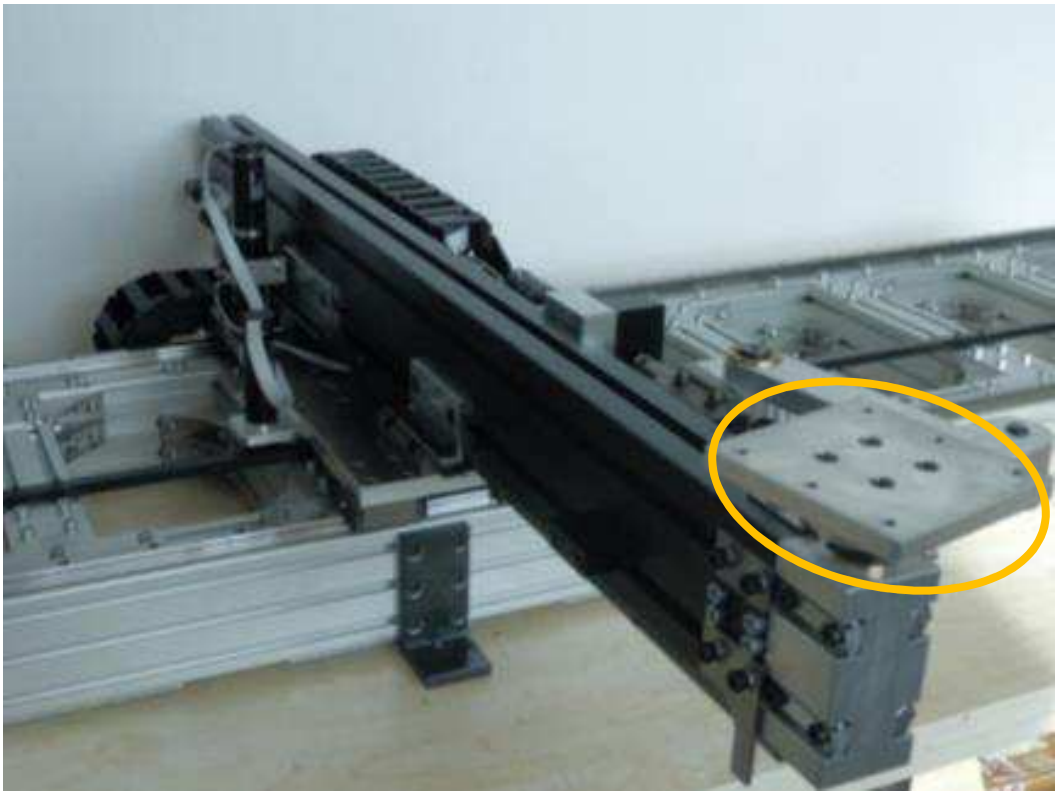

Figure 66 Interfacing flange for mounting the DS system on the robot platform.

Copyright © DashWin Consortium 2012

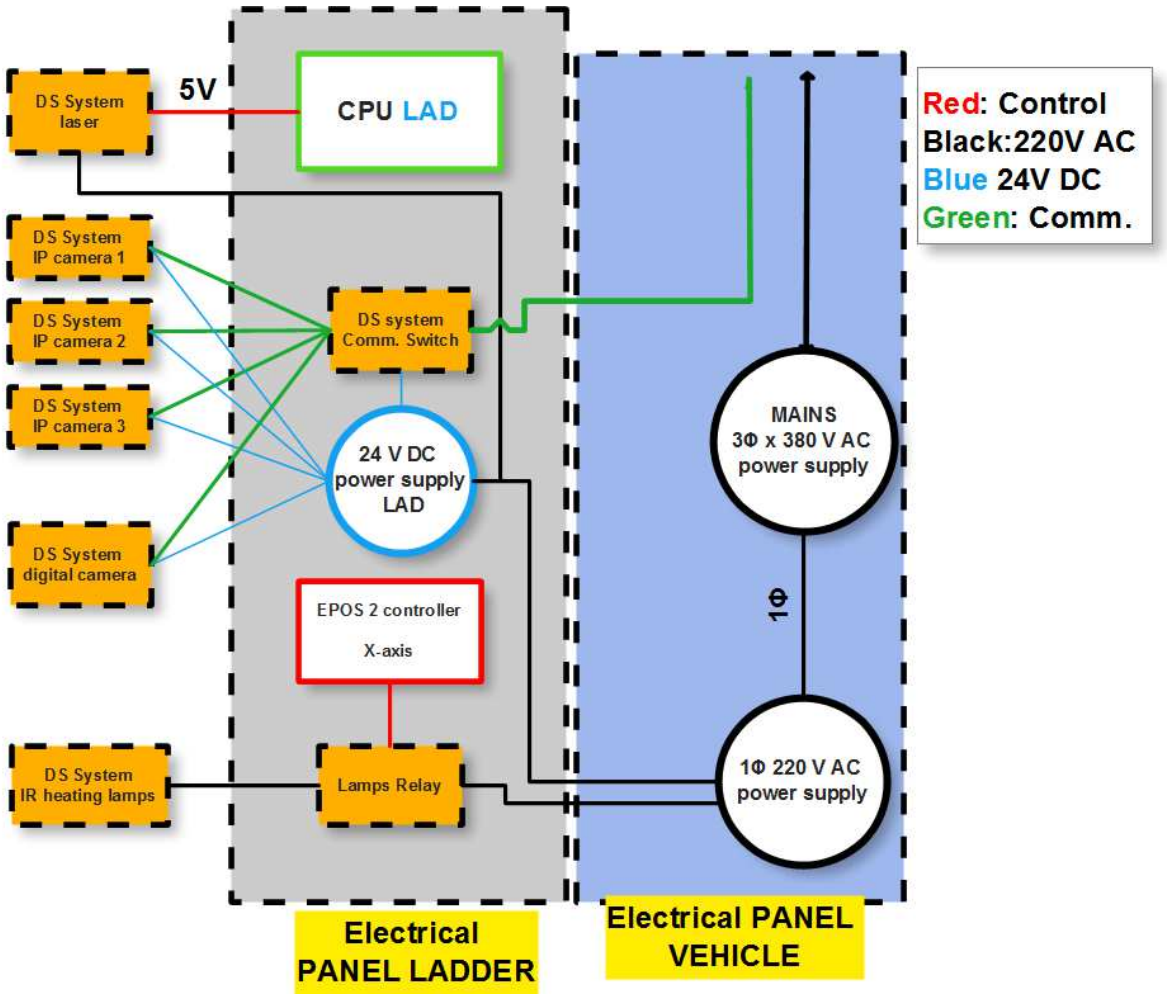

Figure 67 Electrical integration of the DS system with the robot's infrastructure.

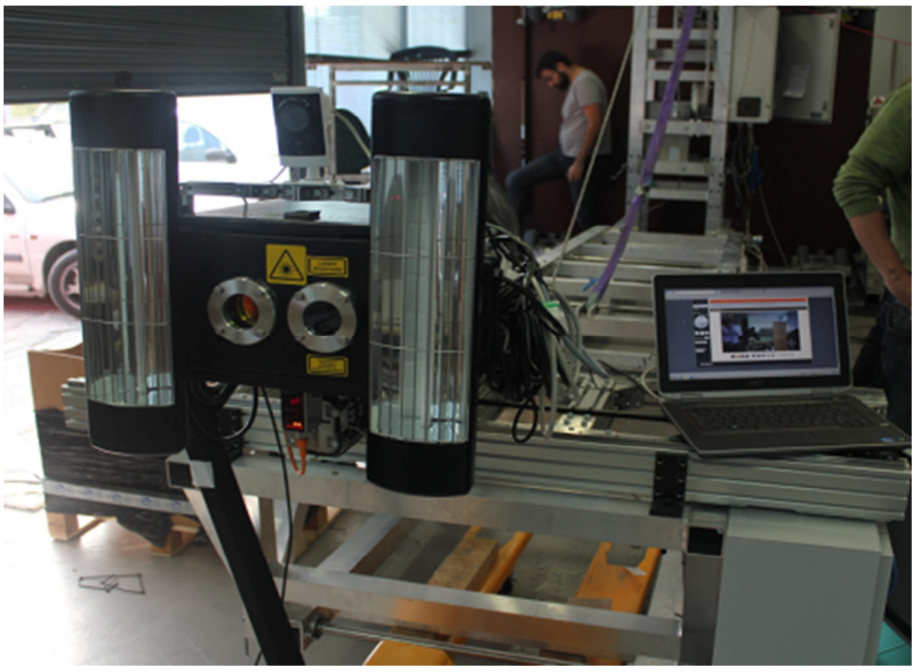

Figure 68 The integrated DashWin system in laboratory.

Copyright © DashWin Consortium 2012

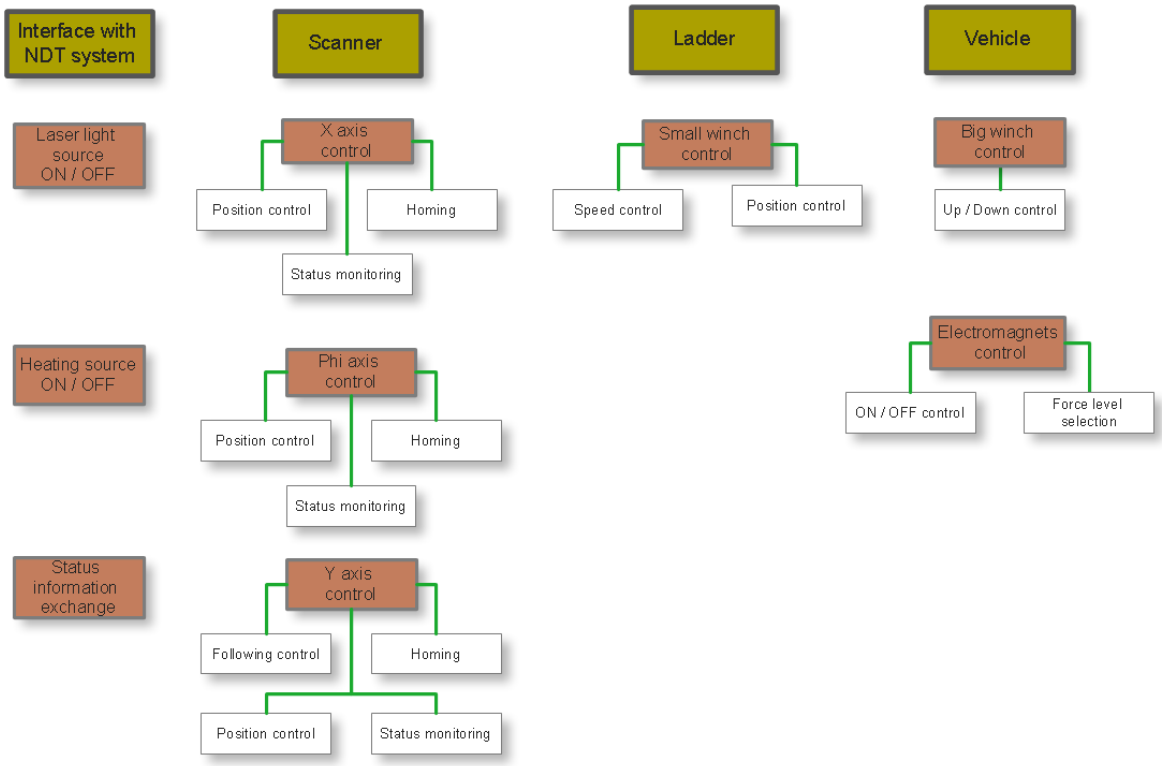

Figure 69 The control operations for the robotic platform.

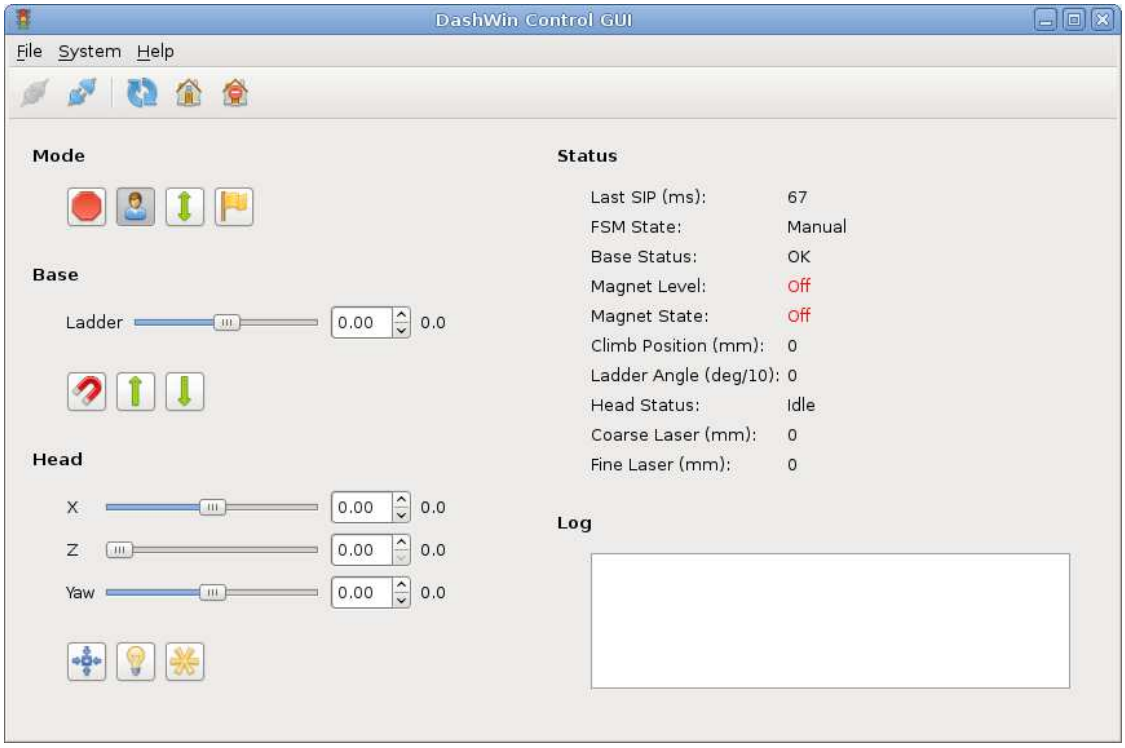

Figure 70 Control graphical user interface (GUI).

Copyright © DashWin Consortium 2012

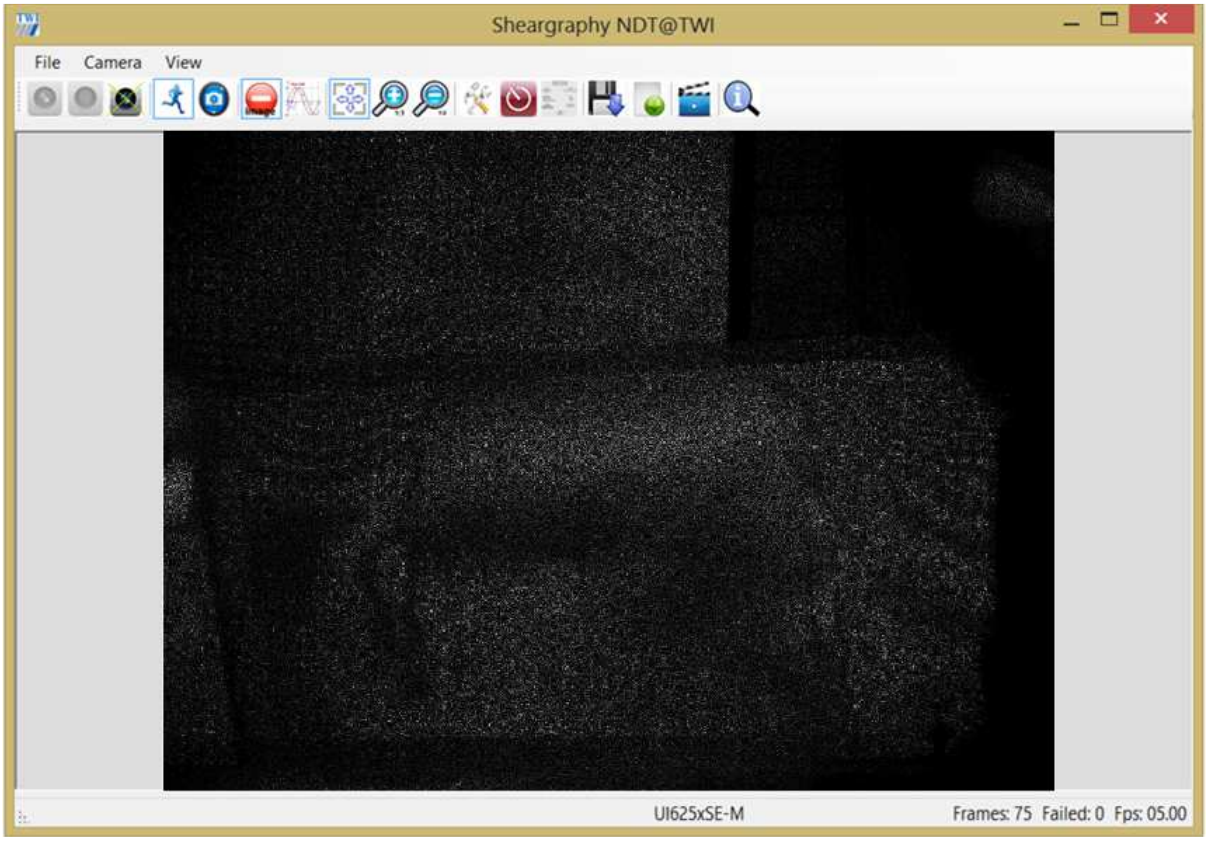

Figure 71 DashWin shearography software.

Figure 72 The second version shearography system in a protective enclosure

Copyright © DashWin Consortium 2012

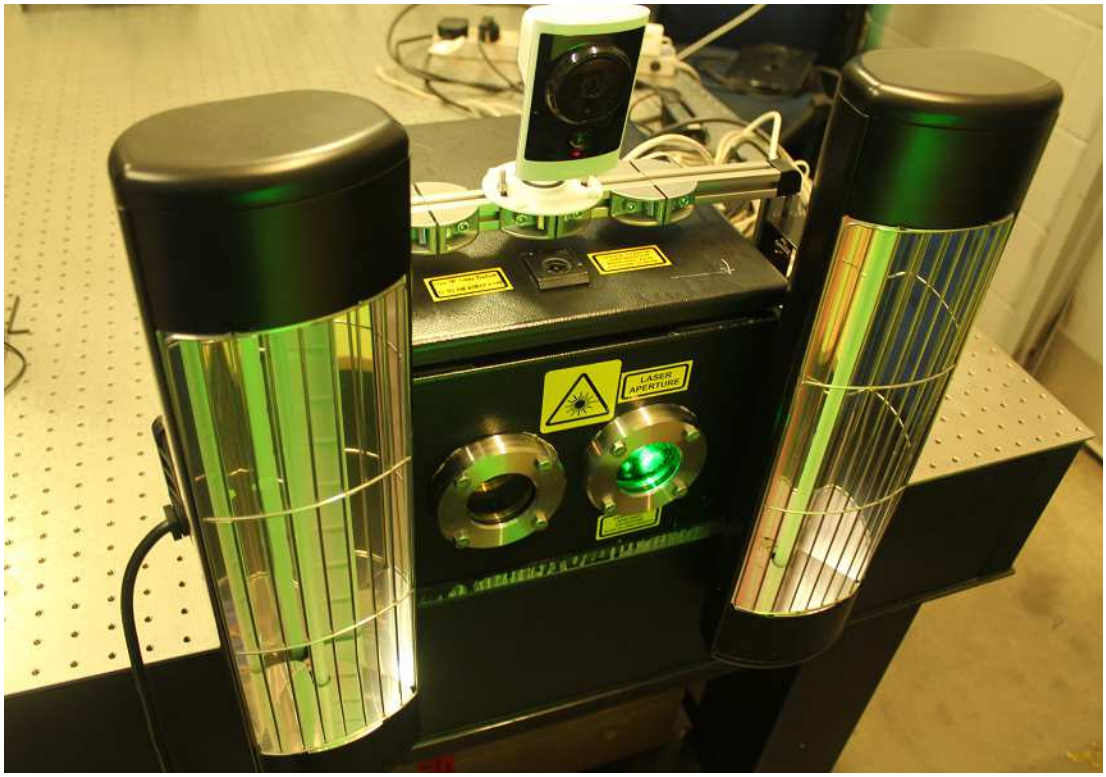

Figure 73 The second version integrated DashWin shearography system equipped with two heating lamps on the left and right hand sides, and a surveillance camera on the top.

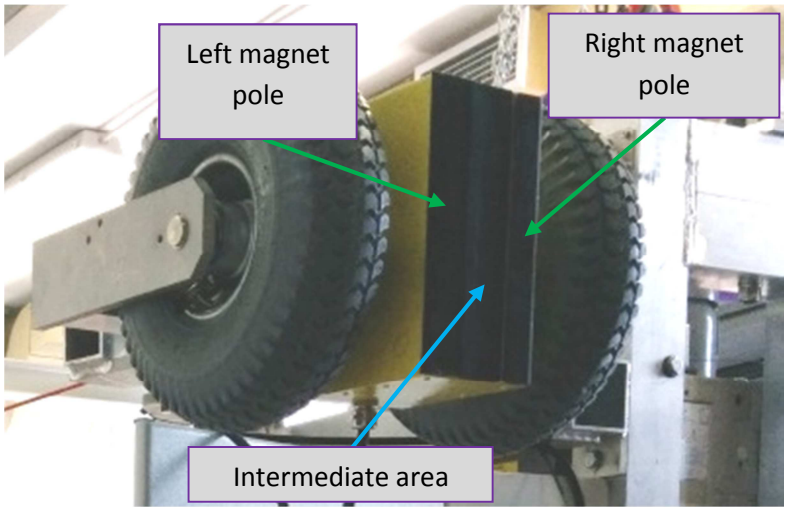

Figure 74 The electromagnets close up

Copyright © DashWin Consortium 2012

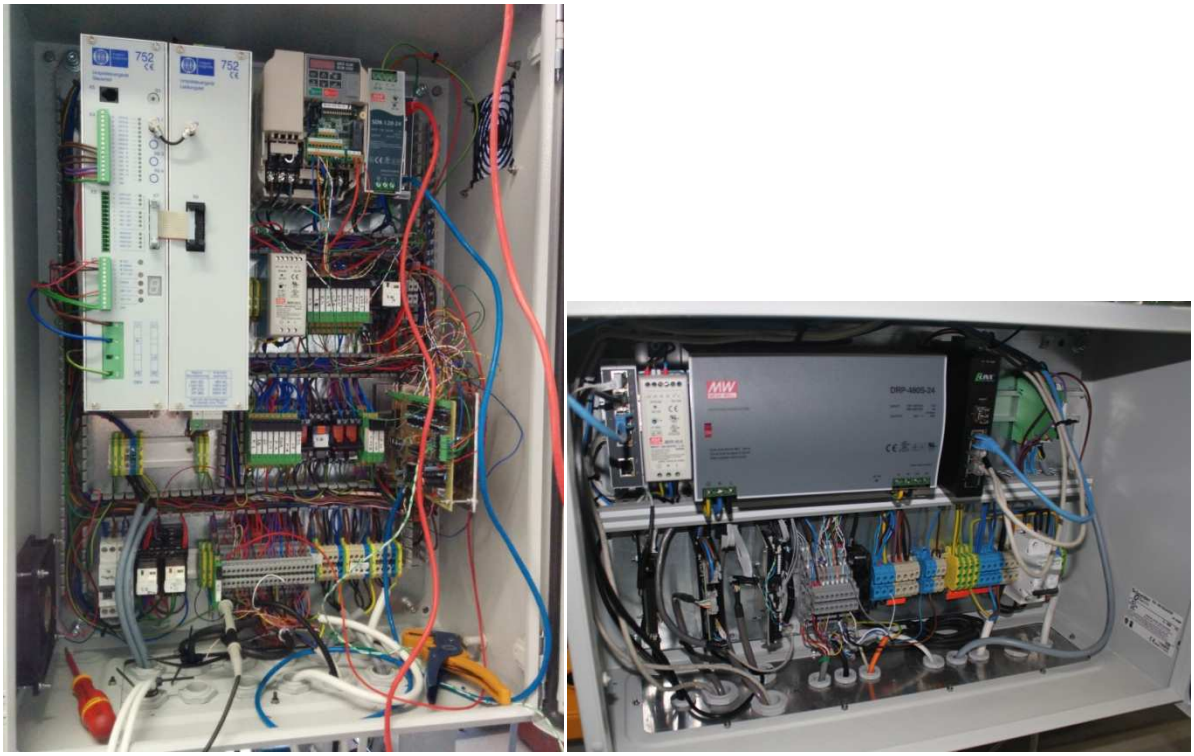

Figure 75 The two electrical panels of the system

(a)

Copyright © DashWin Consortium 2012

(b)

Copyright © DashWin Consortium 2012

(c)

Figure 76 The Dashwin system at a WTB height

Copyright © DashWin Consortium 2012

Figure 77 A standing 4m long WTB, an infrared heating lamp and the shearography system in an outdoor test.

Copyright © DashWin Consortium 2012

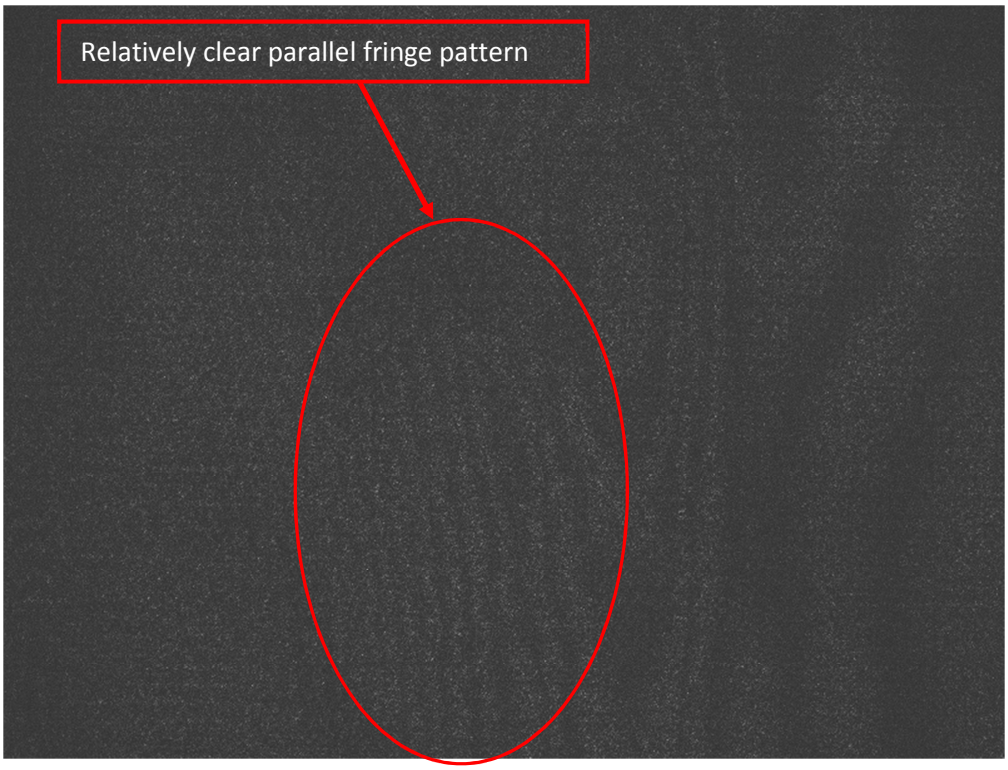

Figure 78 A typical shearography fringe pattern which has low contrast due to strong background illuminations from natural light.

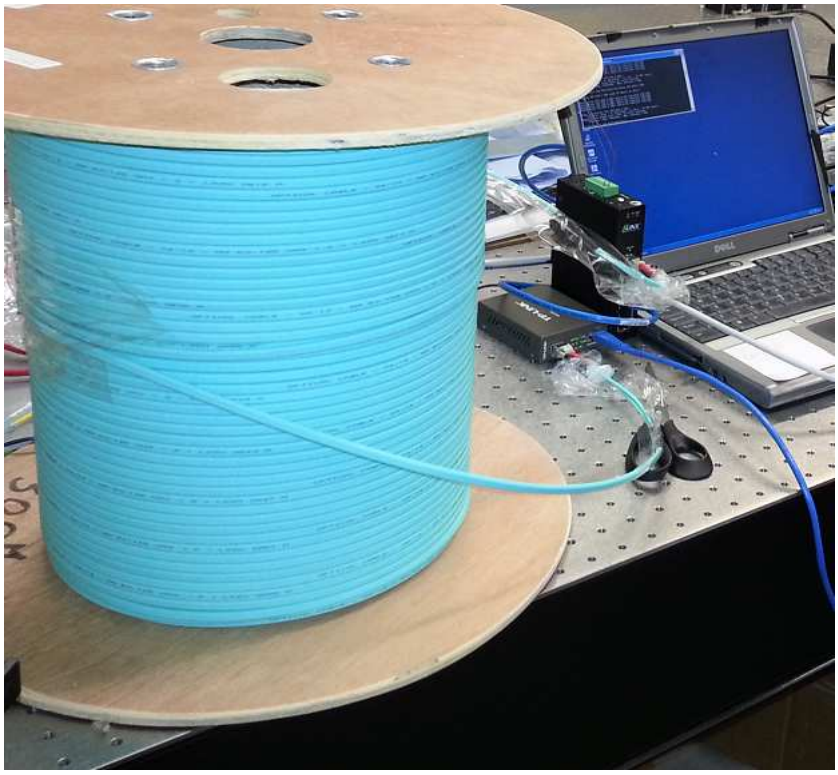

Figure 79 A 300m long optical cable was used to connect the camera and a laptop computer.

Copyright © DashWin Consortium 2012

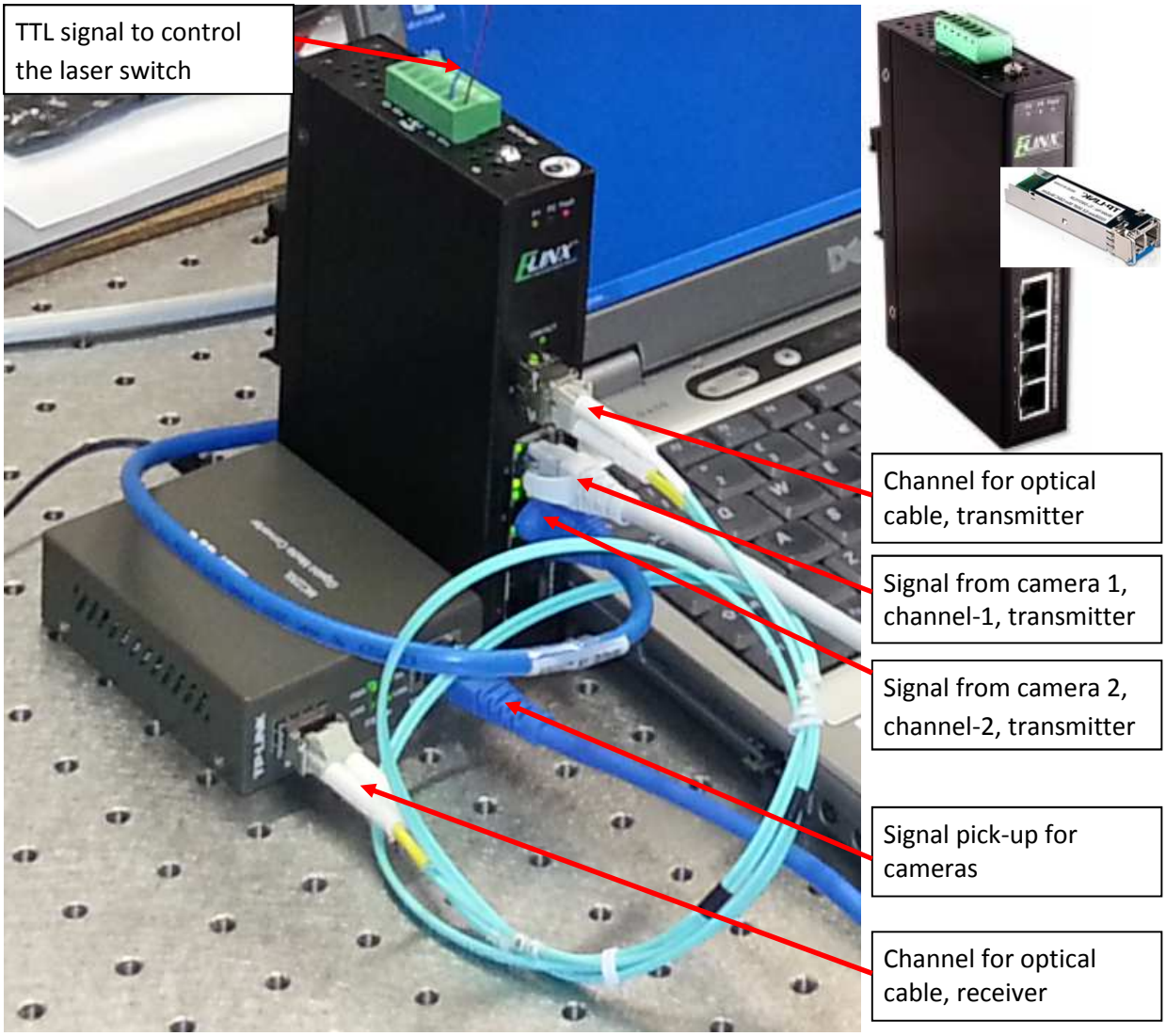

Figure 80 Optical cable connections. The connector has four data channels, allowing four data cables to be connected at the same time.

Copyright © DashWin Consortium 2012

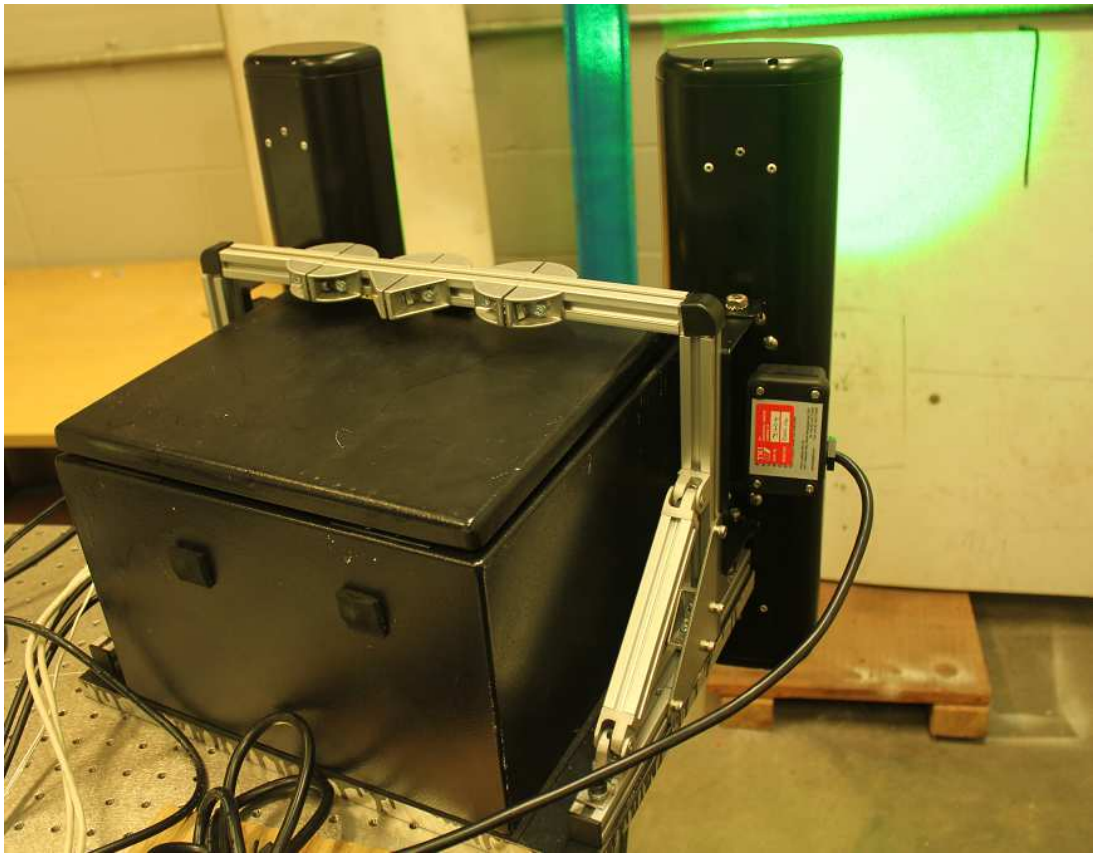

Figure 81 Test of the new shearography system.

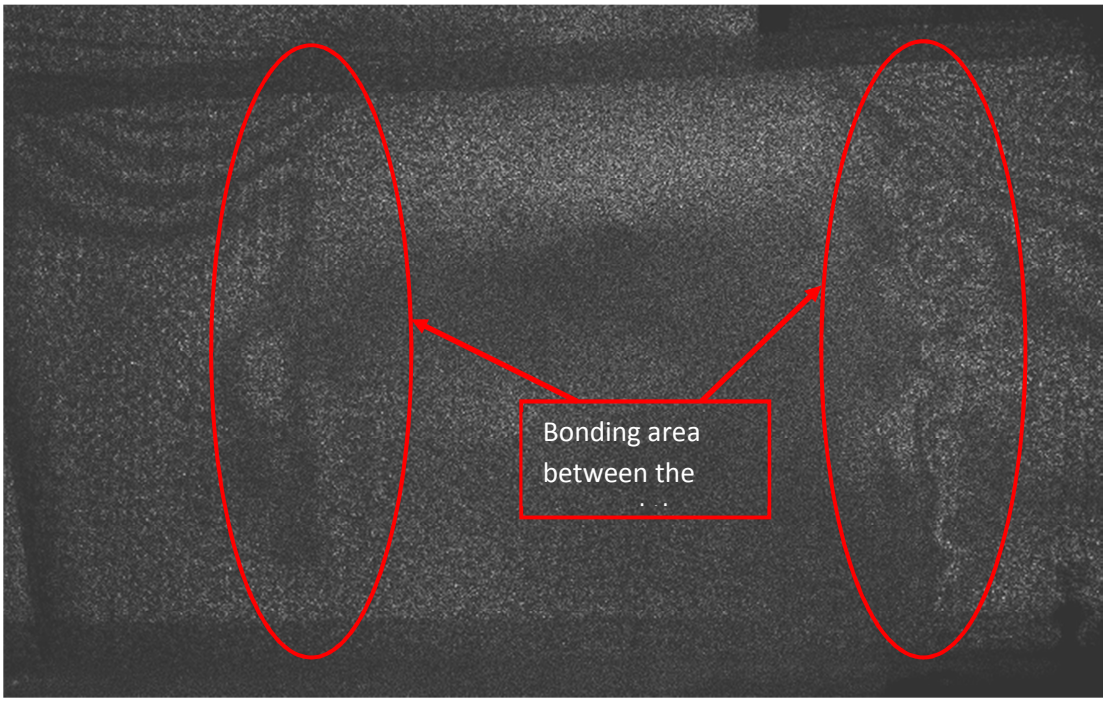

Figure 82 A shearography fringe pattern produced by the new shearography system.

Copyright © DashWin Consortium 2012

Figure 83 Mechanically assembling the shearography system onto the robotic platform.

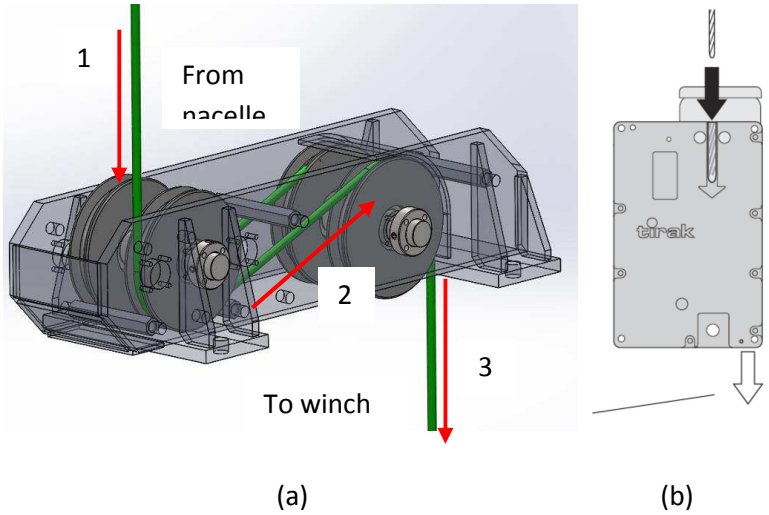

Figure 84 Steel cable connections. (a) Main cable route through the main winch's pulleys system, (b) Cable installation inside the winch (instructions & picture by the manufacturer)

Copyright © DashWin Consortium 2012

Figure 85 Attachment of the lifting cable on the main winch mounted on the platform.

Figure 86 System lifting to a perpendicular position

Copyright © DashWin Consortium 2012

Figure 87 Attachment of the platform on the WTB monopile

Copyright © DashWin Consortium 2012

Figure 88 Remote control of the platform to climb up the WTB monopile

Figure 89 Robot arm opened to enable the shearography system to achieve the correct distance from the WTB. [Note that the green spot ahead of the heating lamps is the laser illuminated area where the inspection will be carried out.]

Copyright © DashWin Consortium 2012

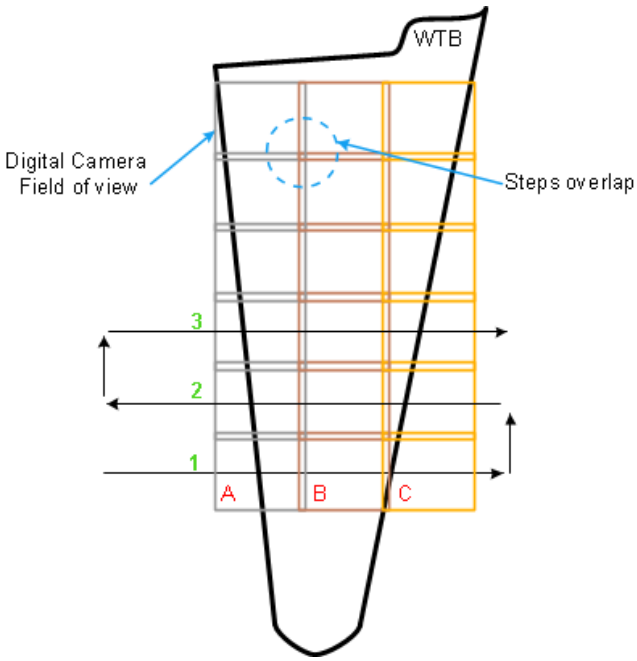

Figure 90 Scanning pattern with overlaps

Figure 91 Laser illuminated area on the WTB which was captured by the surveillance camera on top of the shearography box.

Copyright © DashWin Consortium 2012

Figure 92 A typical still image extracted from a video clip recorded by the surveillance camera.

Figure 93 A full image of the Vesta V47 wind turbine in which the WTBs have a length of 23m.

Copyright © DashWin Consortium 2012

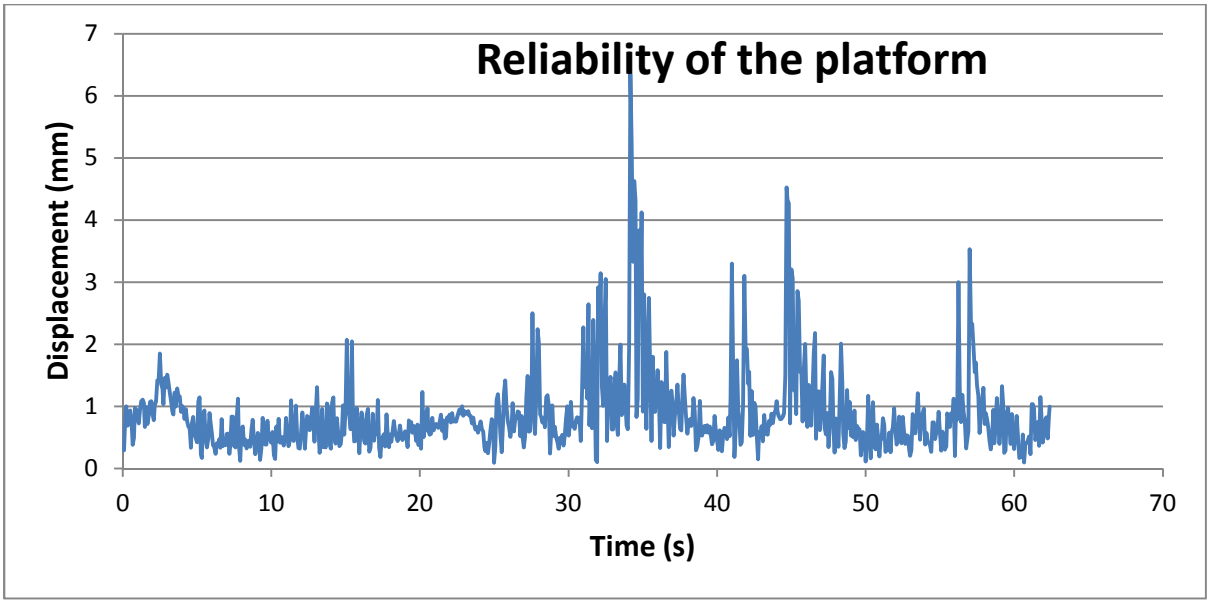

Figure 94 Displacement of the surveilance camera relative to an infinite scenery feature in the imge. It is a measure of the reliability of the robotic platform.

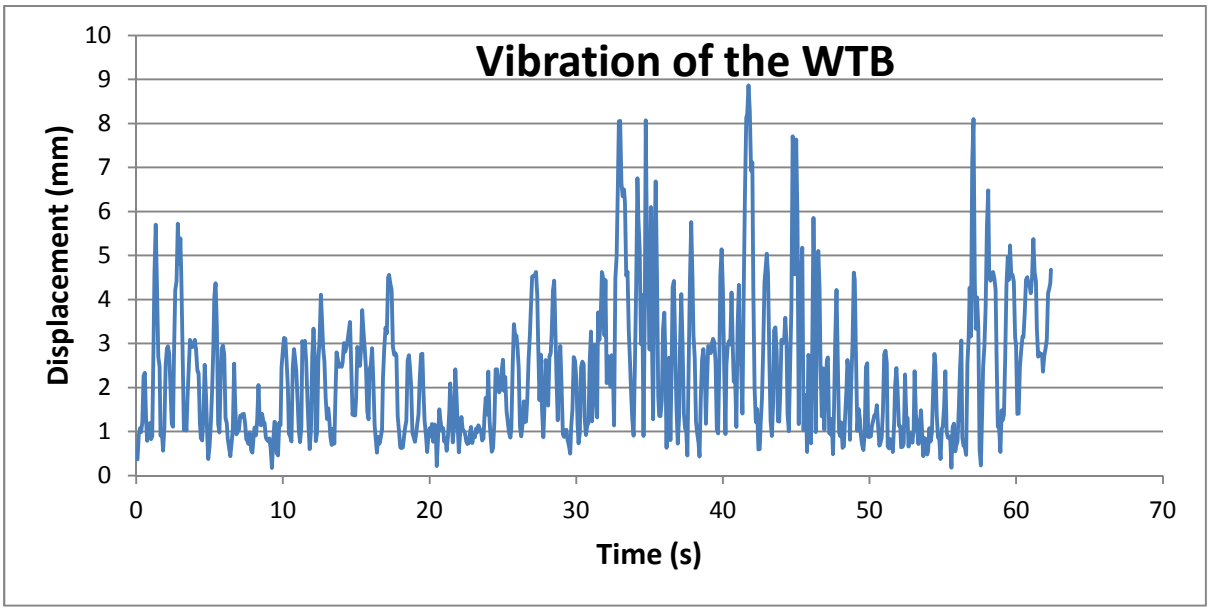

Figure 95 Vibration of the WTB.

Copyright © DashWin Consortium 2012

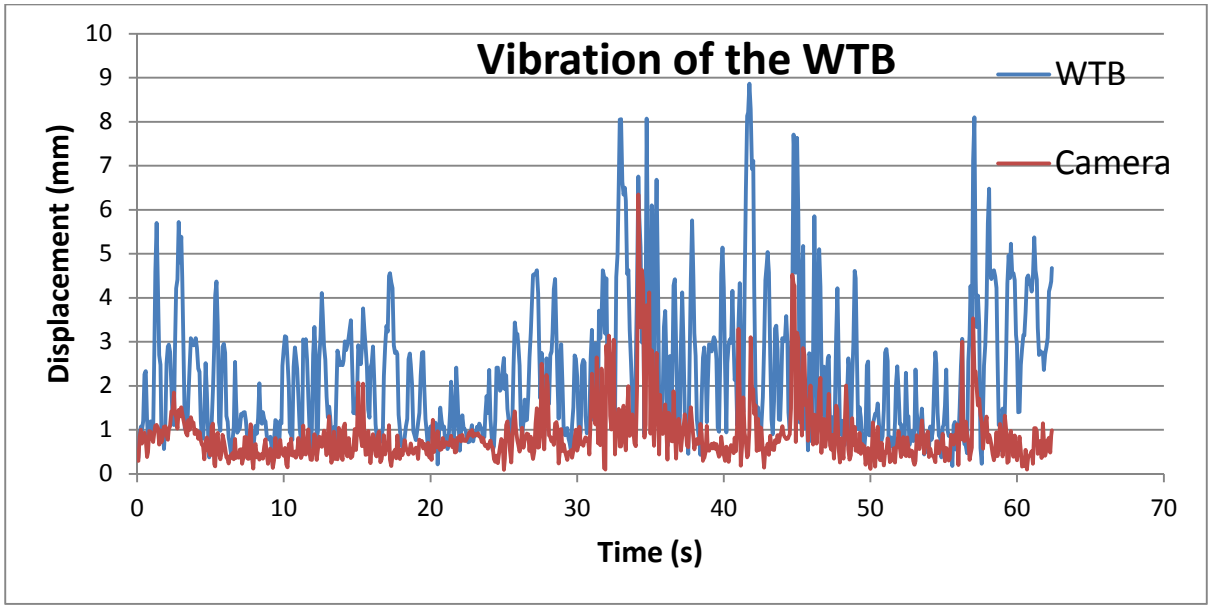

Figure 96 Vibration of the platform (camera) and the WTB.

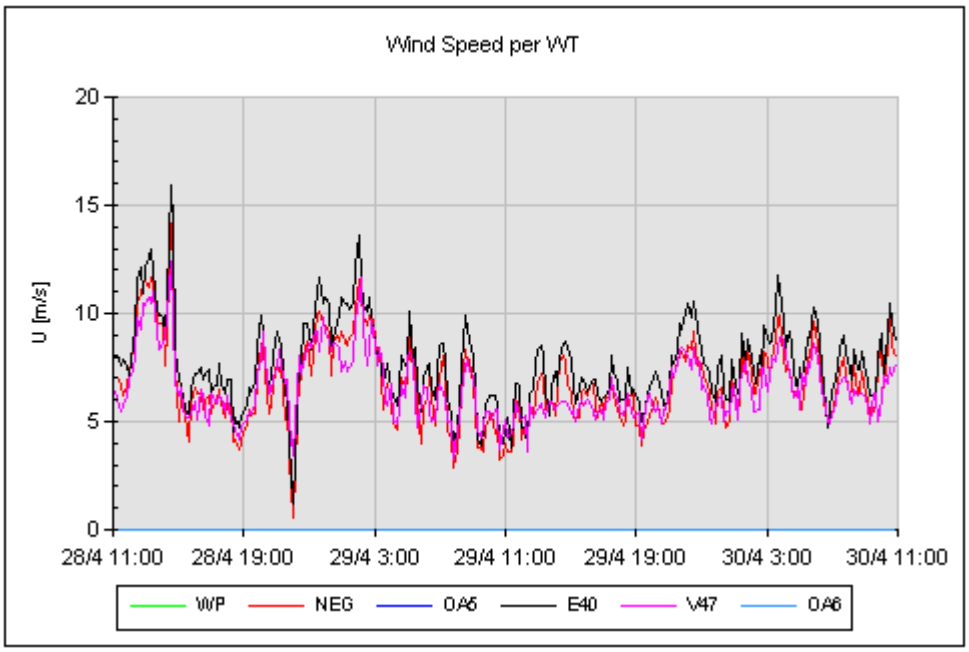

Figure 97 Wind Speed during the trial days on the Wind turbine.

Copyright © DashWin Consortium 2012

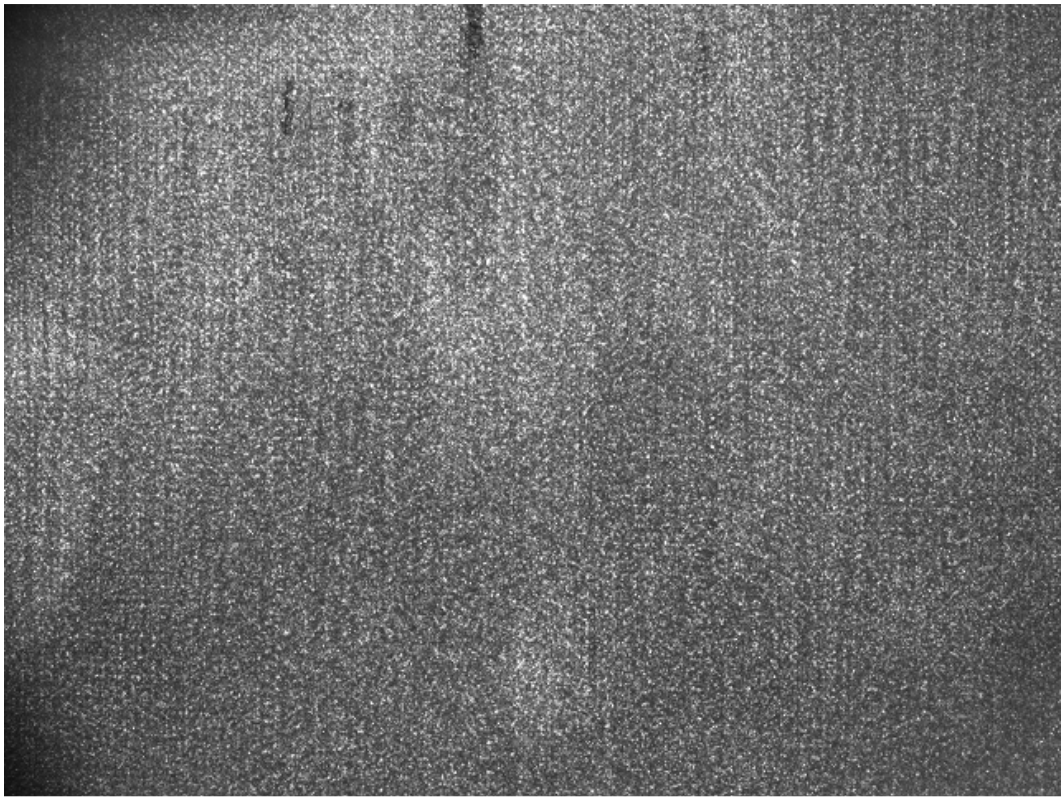

(a)

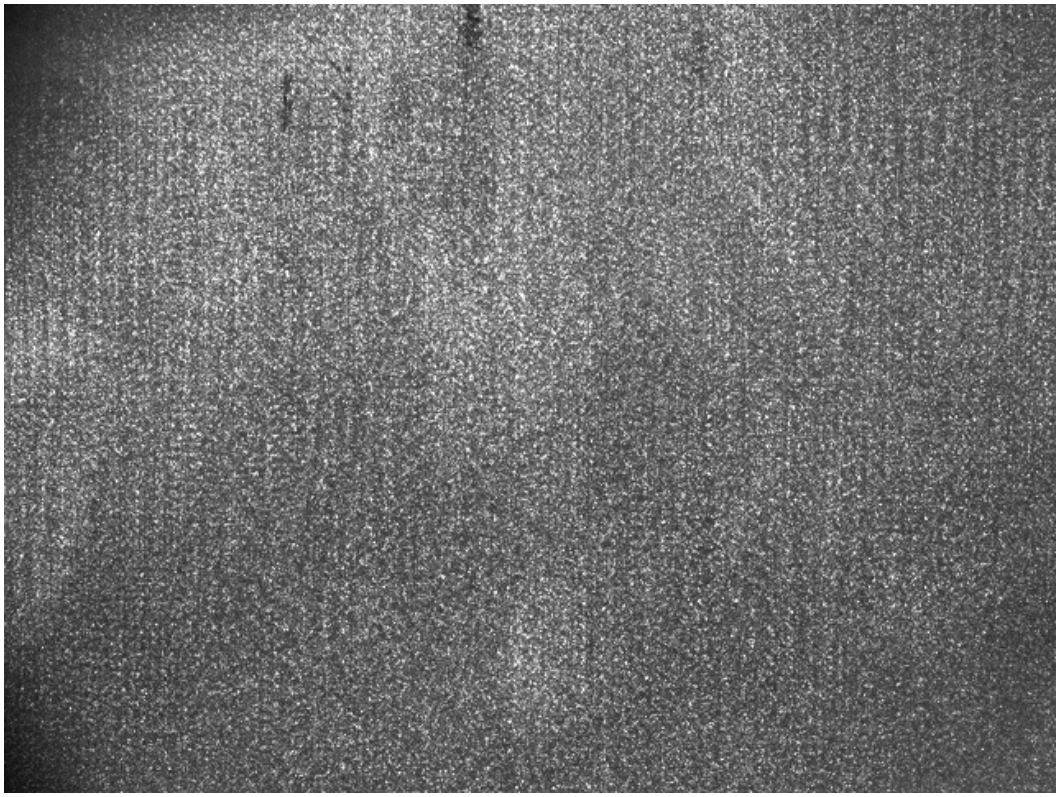

(b)

Copyright © DashWin Consortium 2012

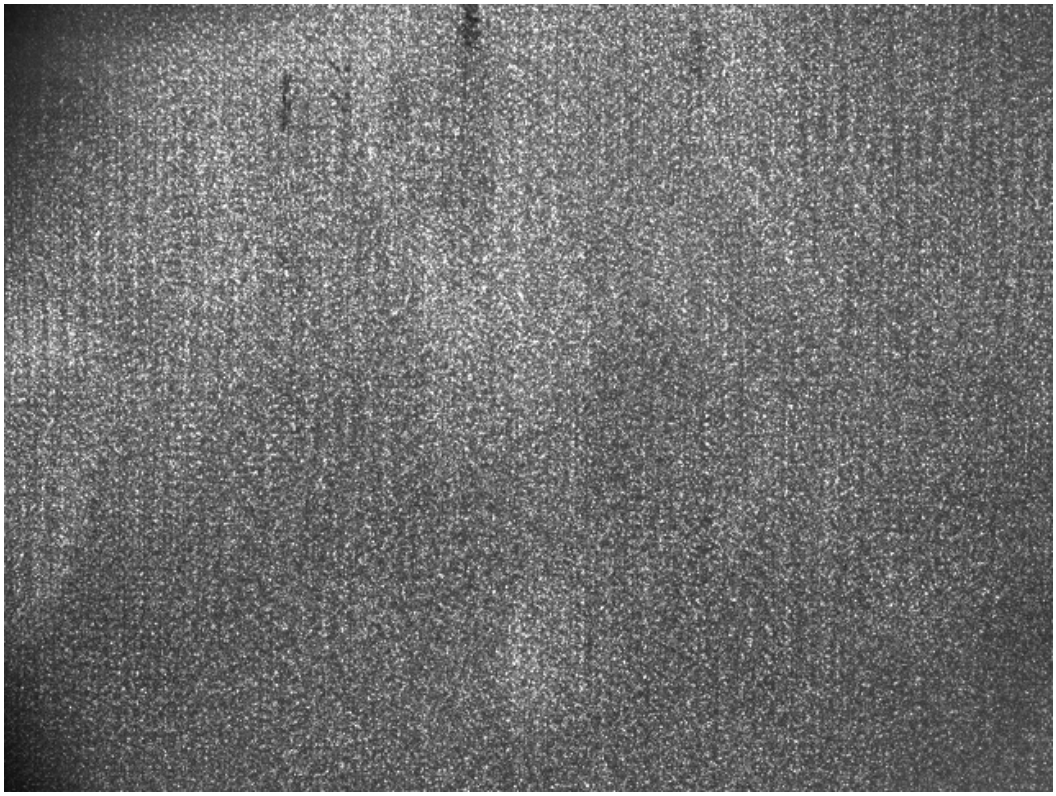

(c)

Figure 98 Three speckle images extracted from a video clip: (a) the 11th, (b) the 90th, and (c) the 508th still image.

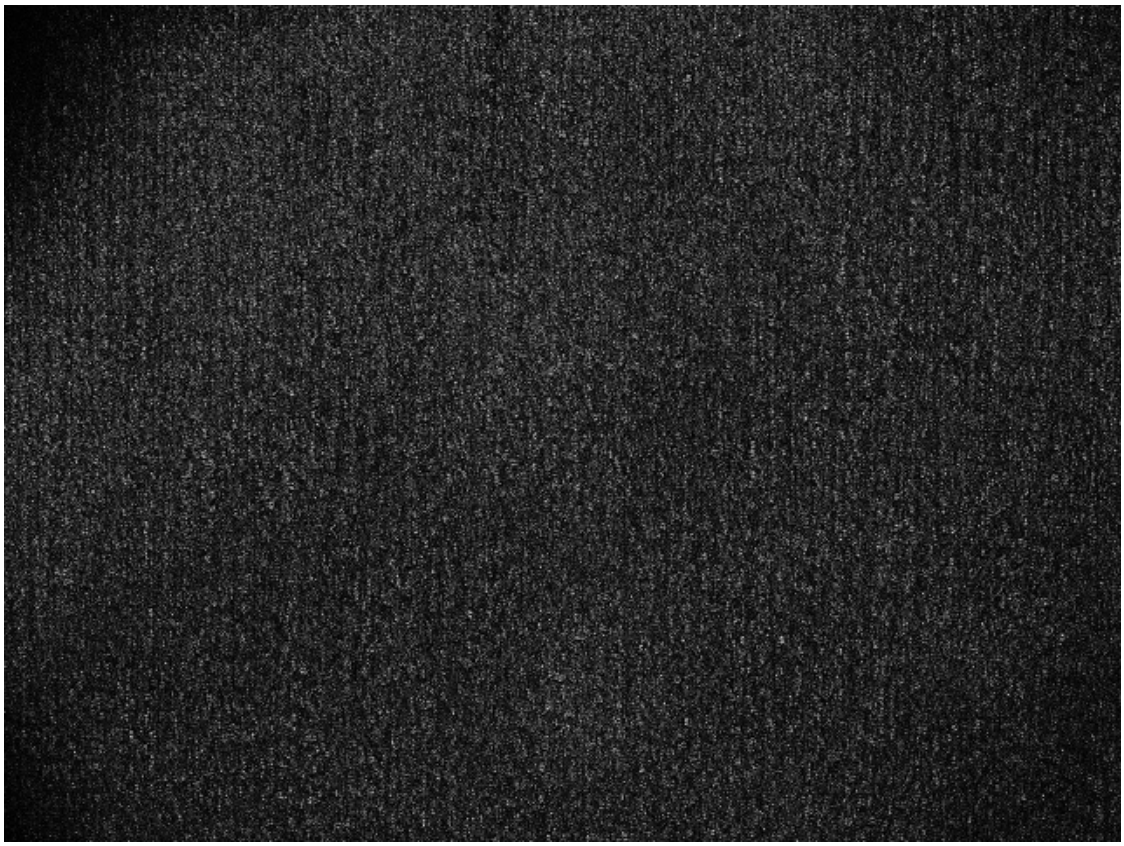

(a)

Copyright © DashWin Consortium 2012

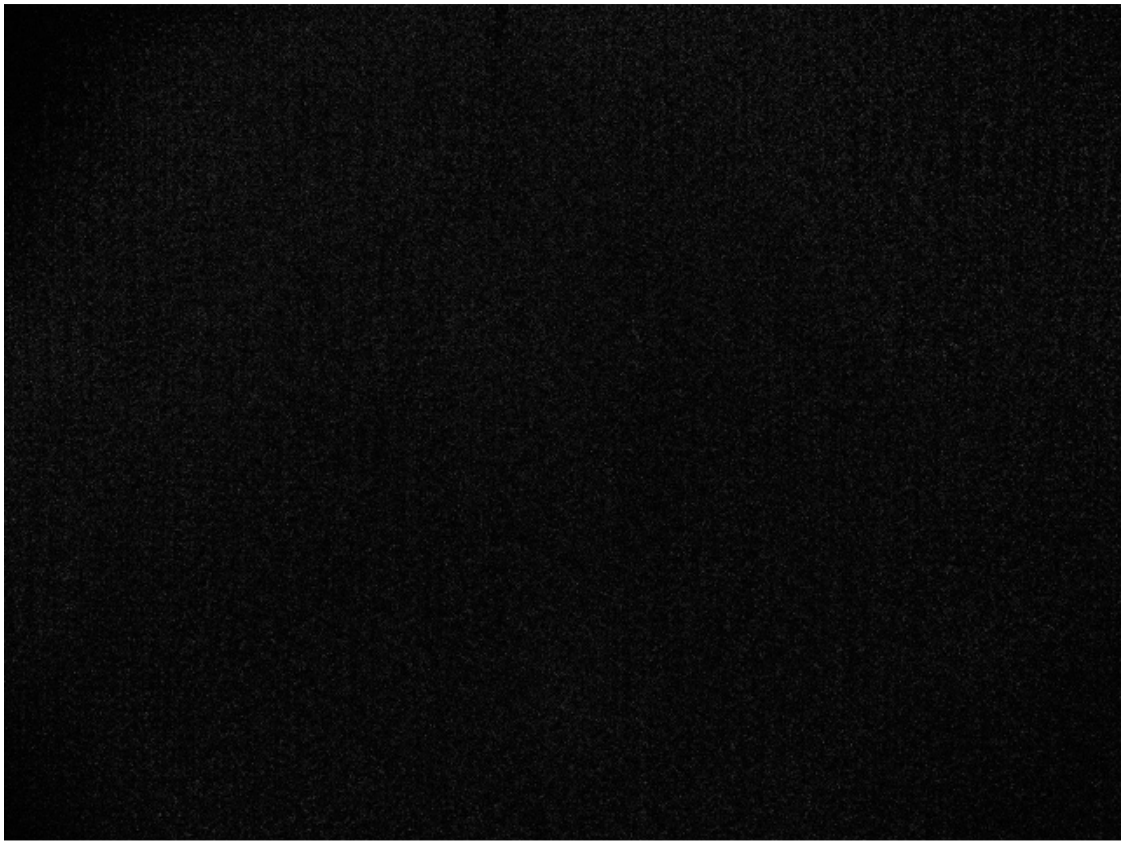

(b)

Figure 99 Two shearography images produced by image subtraction between (a) 11th and 90th, and (b) 11th and 508th speckle images from a video clip recorded in the field trial.

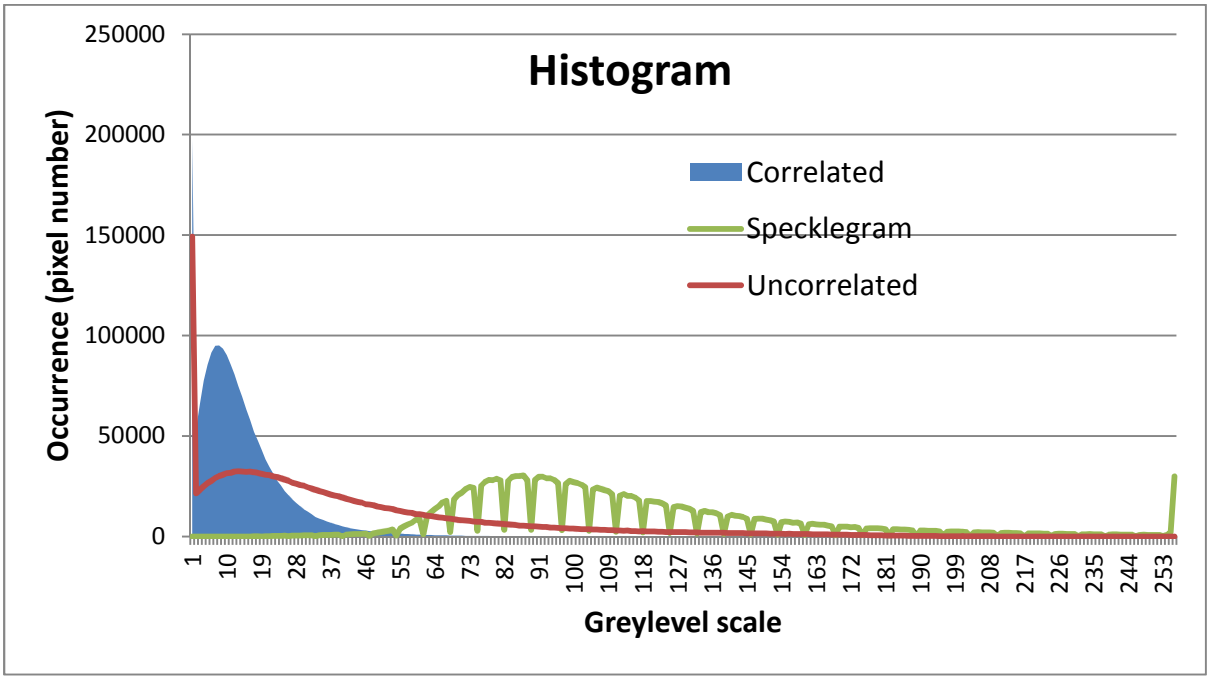

Figure 100 Histogram of a speckle pattern and two shearography patterns shown in Fig.99.

Copyright © DashWin Consortium 2012

Table 1 Types of defects found in composite materials

Bearing surface damage	Blistering	Contamination	Corner/Edge splitting
Corner crack	Corner radius delaminations	Cracks	Creep
Crushing	Cuts and scratches	Damaged filaments	Delaminations
Dents	Edge damage	Erosion	Excessive ply overlap
Fastener holes	Fiber distribution variance	Fiber faults	Fiber kinks
Fiber/matrix disbonds	Fiber misalignment	Fracture	Holes and penetration
Impact damage	Marcelled fibers	Matrix cracking	Matrix crazing
Miscollination	Mismatched parts	Missing plies	Moisture absorption
Overaged prepreg	Over or under-cured	Pills or fuzz balls	Ply underlap or gap
Porosity	Prepreg variability	Reworked areas	Surface damage
Surface oxidation	Surface swelling	Thermal stresses	Translaminar cracks
Unbond or disbond	Variation in density	Variation in fiber volume ratio	Variation in thickness
Voids	Warping	Wrong materials	

Table 2 DashWin defect detection capabilities for shearography.

Defect Type	**Diameter / Length (mm)**	**Maximum Depth (mm)**
Void/hole	5	4
	10	8
	20	16
	40	30
	80	60
Crack*	10	2
	20	4
	40	8
	80	16
	150	30
Disbond*, Delamination*	10	3
	20	5
	40	10
	80	16
	150	30
Impact damage	10	-

*Note: Detection capabilities for cracks, disbonds and delaminations are highly dependent on the local structure of the component.

Copyright © DashWin Consortium 2012

Table 3 Material properties used in FEM simulations.

Material	Steel	Aluminium	E-Glass	Balsa	Gel	Mat	C260	C520	Carbon	Faulty Layer
Conductivity (W/mK)	50	237	1.3	0.05	25	10	0.17	0.23	17	0.0243
Density (kg/m3)	7800	2700	1870	130	1235	1500	1760	1870	1490	1.293
Specific Heat (J/kgK)	450	897	940	2.9	200	500	940	1040	710	1.005
Young's modulus (GPa) E1	210	70	38	12.8	3.44	7.58	43	48.2	130	2.41
Young's modulus (GPa) E2	210	70	13	0.5	3.44	7.58	8.9	11.7	10.3	0.585
Poisson ratio	0.25	0.34	0.23	0.231	0.3	0.3	0.27	0.3	0.3	0.3
G12 (GPa)	80.8	26	15.4	0.162	1.32	6.48	4.5	6.48	7.17	0.324
G13 (GPa)	80.8	26	15.4	0.162	1.32	6.48	4.5	6.48	7.17	0.324
G23 (GPa)	80.8	26	15.4	0.162	1.32	6.48	4.5	6.48	7.17	0.324

Table 4 Composite section lay-up arrangement.

Layers	A	B	C	D	E	F	G	H	I	J
1	Gel	Gel	Gel	Gel	Gel	Gel	Gel	Gel	Gel	Gel
2	Mat	Mat	Mat	Mat	Mat	Mat	Mat	Mat	Mat	Mat
3	C520	C520	C520	C520	C520	C520	C520	C520	C520	C520
4	Mat	Mat	Mat	Mat	Mat	Mat	Mat	Mat	Mat	Mat
5	C520	C520	C520	C520	C520	C520	C520	C520	C520	C520
6	C260	C260	C260	C260	Balsa	C260	C260	C260	C260	C260
7	Mat	Mat	Mat	Mat	C260	Mat	Mat	Mat	Mat	Mat
8	C260	C260	C260	C260	Mat	C260	C260	C260	C260	C260
9	C520	C260	C520	C520	C260	Balsa	C520	C520	C520	
10	C520	Mat	C520	C520		C260	C520	C520	C520	
11	C520	C260	C520	C520		Mat	C520	C520	C520	
12	C520	C520	C520	C520		C260	C520	C520	C260	
13	C520	Mat	C520	C520		C520	C520	C520	Mat	
14	C520	C520	C520	C520		Mat	C520	C520	C260	
15	C520		C520	C520		C520	C260	C260	C520	
16	C520		C260	C260			Mat	Mat	Mat	
17	C520		Mat	Mat			C260	C260	C520	
18	C520		C260	C260			C520	C520		
19	C260		C520	C520			Mat	Mat		

Copyright © DashWin Consortium 2012

Table 4 Composite section lay-up arrangement (continue).

Layers	A	B	C	D	E	F	G	H	I	J
20	Mat		Mat	Mat			C520	C520		
21	C260		C520	C520				C520		
22	C520			C520				Mat		
23	Mat			Mat				C520		
24	C520			C520				C520		
25				C520				Mat		
26				Mat				C520		
27				C520				C520		
28				C520				Mat		
29				Mat				C520		
30				C520				C520		
31				C520				Mat		
32				Mat				C520		
33				C520						

Table 5 Defective composite section lay-up arrangement.

Layers	Ga	Ge
1	Gel	Gel
2	Mat	Mat
3	C520	C520
4	Mat	Mat
5	C520	C520
6	C260	C260
7	Mat	Mat
8	C260	C260
9	C520	C520
10	C520	C520
11	C520	C520
12	FAULT	C520
13	C520	C520
14	C520	C520
15	C520	C260
16	C260	Mat
17	Mat	C260
18	C260	FAULT
19	C520	C520
20	Mat	Mat
21	C520	C520

Copyright © DashWin Consortium 2012

Table 6 Shearography system specifications relevant to the design of the robotic platform

Description	Value / comment
System's offset distance with regard to the WTB	**~1-2m**. Can be modified if camera lenses are suitably adjusted / replaced
Tolerance of offset distance	**+/- 1mm,** along the whole inspection process
Camera direction with regard to the WTB	**Roughly perpendicular** to the WTB surface
Tolerance of camera direction with regard to the WTB	**Acceptable tolerance of +/- 30º with regard to the surface normal**
Camera field of view	**Around 1m^2** at an offset distance of 1m. Will change if other lenses are used
System weight	Max. ~30Kg
System outer dimensions	400mm x 500mm x 450mm (H)
Power	Up to 48V DC for the camera and laser source (max. ~300W) 230V AC (~3-6KW) for the heating source
Communication	Fibre optic data link directed to the ground station Interconnection with the manipulator controller (Lights ON/OFF)
CPU	Laptop at ground level
Control GUI	Custom made, running on Microsoft Windows

Table 7 Environmental specifications for the robotic platform.

Description	Value / comment
Permissible weather conditions	These conditions, **for the moment** have been aligned with those for human operators. That is, operation in good weather conditions (no rain) with wind speeds below 12m/s.

Table 8 Workspace specifications for the robotic platform

Description	Value / comment
Monopile diameters	Depends on the WT size (output power) (e.g. for a 1MW WT, the base diameter is typically around 5m and upper diameter approximately 4m).
Monopile height	Depends on the WT size. (e.g. for a 1MW WT it is approximately 100m).
Monopile outer surface	Made of tubular parts welded together. Weld reinforcements protruding ~5-10mm. Coated white.

Copyright © DashWin Consortium 2012

Blade geometry	Depends on the WT size (e.g. for a 1MW WT the WTB length is ~40m and its maximum width is ~3m).
Blade positioning on hub	At an inclination of ~5º.
Blade-monopile clearance	Depends on the WT size (e.g. for a 1MW WT the maximum clearance is ~8m).
Blade vibration specifications	Only qualitative specifications were provided.
Hanging points on nacelle	At least one, between the WTBs and the monopile.

Principle of a two-step interferometry phase extraction approach

This approach is based on Spiral Phase Transformation and optical flow. The optical flow method calculates the motion field at every pixel position between two image frames that are taken at times t and t +Δt. An arbitrary pixel at time t given by (x; y; t) and with intensity *I*(x;y;t) will move between two consecutive frames to the position(x+Δx; y +Δy; t +Δt) with intensity *I*(x+Δx; y +Δy; t +Δt). Assuming the movement is small, the intensity map at t+Δt can be expanded as:

$$I(x+\Delta x, y+\Delta y, t+\Delta t) = I(x,y,t) + I_x \Delta x + I_y \Delta y + I_t \Delta t \quad (1)$$

where I_x , I_y and I_t represent the derivatives of *I* with respect to x, y, and t. It is reasonable to assume that the brightness of an object does not change over time. Therefore, we have $I(x+\Delta x, y+\Delta y, t+\Delta t) = I(x,y,t)$, hence Equation (1) can be rewritten as:

$$I_x u + I_y v + I_t = 0 \quad (2)$$

where $u = x_t$ and $v = y_t$ corresponds to the velocity components. Equation (2) can be used to determine the components of the movement in the direction of the intensity gradient, but it is not possible to obtain the components along the direction of the iso-intensity contours. As a consequence, the flow velocity (u; v) cannot be computed locally without introducing additional constraints. One way of addressing this issue is to impose smoothness in the u and v fields. A regularized optical flow method has been developed, and is described as follows:

Firstly, an energy map is defined as:

$$E^2 = (I_x u + I_y v + I_t)^2 + \lambda(u_x^2 + u_y^2 + v_x^2 + v_y^2) \quad (3)$$

where E is the energy to be minimized and λ is the regularizing parameter that weighs the smoothness of *u* and *v*. From Equation (3), it is possible to obtain an iterative solution using the Gauss–Seidel method:

$$u^{k+1} = \bar{u}^k - I_x[I_x \bar{u}^k + I_y \bar{v}^k + I_t] \Big/ (\lambda^2 + I_x^2 + I_y^2)$$
$$v^{k+1} = \bar{v}^k - I_y[I_x \bar{u}^k + I_y \bar{v}^k + I_t] \Big/ (\lambda^2 + I_x^2 + I_y^2) \quad (4)$$

Copyright © DashWin Consortium 2012

where u^{k+1} and v^{k+1} are the velocity components obtained in the iteration k+1 and $\bar{u}$ and $\bar{v}$ correspond to the mean value of u and v in a defined neighbourhood (typically of size of 5 × 5 pixels). Once the u and v maps at every pixel are obtained, we can calculate the direction map as:

$$\eta = \arctan(\frac{v}{u}) \tag{5}$$

In a two-step PSI, we have two patterns of the form:

$$I_t = a + b\cos(\varphi + \omega t) \qquad t = 0,1 \tag{6}$$

where a is the background illumination, b is the modulation term, Φ is the modulating phase, and ω the instantaneous temporal frequency. If we suppress the DC component of I_t in Equation (6) by using a high-pass filter and apply the SPT operator, we obtain:

$$\mathrm{SPT}\{\overline{I_t}\} = i\exp(i\eta)b\sin(\varphi + \omega t) \qquad t = 0,1 \tag{7}$$

where $\overline{I_t} = b\cos(\varphi + \omega t)$ and SPT corresponds to:

$$\mathrm{SPT}\{\bullet\} = \mathrm{FT}^{-1}\{(\frac{\omega_x + i\omega_y}{\sqrt{\omega_x^2 + \omega_y^2}})FT\{\bullet\}\} \tag{8}$$

where η is the direction map, FT means 2D Fourier transformation, and ωx and ωy are the coordinates in the Fourier space. Note that, if there are only one or two fringes in the interferograms, we can always subtract the DC component to normalise the interferograms. In our case, we propose to calculate the direction map from two interferograms using the regularised optical flow method described above. From Equation (7), if we know the direction map, we have:

$$b\sin(\varphi + \omega t) = -i\exp(-i\eta)\mathrm{SPT}\{\overline{I_t}\} \qquad t = 0,1 \tag{9}$$

from which we can obtain the modulating wrapped phase as:

$$\varphi = \arctan(\frac{-i\exp(-i\eta)\mathrm{SPT}\{\overline{I_t}\}}{\overline{I_t}}) \qquad t = 0,1 \tag{10}$$

Copyright © DashWin Consortium 2012